Microstructures and phases analysis of the 60Al-40V master alloy produced by the aluminothermic process.

By

Tresor Okabo Mapoli

Supervisors:

Prof Charles W. Siyasiya

Dr Kofi A. Annan

Dr Kalenda Mutombo

Submitted in partial fulfilment of the requirements for the degree.

Master of Applied Science (Metallurgy)

In the

Department of Materials Science and Metallurgical Engineering

Faculty of Engineering, Built Environment & Information Technology

UNIVERSITY OF PRETORIA

Republic of South Africa

May 2021

1. DECLARATION

I declare that this dissertation is my work. It is being submitted for the degree of Master of Applied Science in the Faculty of Engineering, Built Environment and Information Technology, University of Pretoria, South Africa. It has not been submitted before for any degree or examination at any other university.

2. SUMMARY

The Al-V binary system is one of the most important sub-systems of the α-β Ti-based alloys designed and used in diverse applications. The Al-V master alloy is used as a semi-finished product in the production of Ti-6Al-4V alloy. The alloy is receiving much attention in the automobile and aerospace industries due to its lightweight and excellent mechanical properties, i.e., the combination of high strength and fatigue resistance at elevated temperatures. In this work, an aluminothermic reaction process was proposed for the production and development of the Al-V master alloy. Al metal and vanadium pentoxide (V_2O_5) were mixed in a proportion that produced an exothermic reaction capable of generating the master alloy and Al_2O_3 rich slag. The target was to produce a 60 wt. % Al and 40 wt. % V master alloy through the aluminothermic process. The thermodynamic calculations, as well as the characterisation of the 60Al-40V master alloy, were carried out in order to understand and improve the production process of the master alloy.

The study was aimed at determining the thermodynamic parameters using thermodynamic computer software and analytical characterisation techniques to assist in the development and production of the Al-V master alloy.

The CALPHAD package within Thermo-Calc™ software was used to predict the equilibrium phase diagram, thermodynamic properties such as the Gibbs free energy, enthalpy and /or entropy of formation and activities of constitutive elements in the Al-V system. The aluminothermy produced master alloy was experimentally characterised using techniques such as light optical microscopy (LOM), scanning electron microscopy (SEM), energy-dispersive X-ray spectroscopy (EDX), and X-Ray diffraction (XRD) analyses. These techniques were employed to assess the viability of the aluminothermic process in terms of microstructure, chemical composition, crystallographic structure, and phases present in the produced master alloy. The differential scanning calorimetry (DSC) and thermogravimetry (TG) thermal analysis techniques were used to determine the phase transformations and phase stability.

The Al-V equilibrium binary phase diagram that was predicted by the Thermo-Calc™ software agreed with some of the phases that were observed in this work, i.e., the following phases were observed as predicted by the Thermo-Calc™: the Al (fcc), the V (bcc) and three intermetallic compounds namely the $Al_{23}V_4$, Al_3V and the Al_8V_5 phases. The maximum solubility of V in liquid

Al of 1.2 wt. % was found at a temperature of 664 °C. The liquidus line was fairly reproduced and the invariant temperatures of the melting temperature of the five intermetallic phases were determined. The value of the integral molar Gibbs energy of mixing was found to be negative, about -25 J/mol-atom for the most stable phase (Al_3V), indicating that the reaction was spontaneous and was favoured by the change in the entropy and enthalpy. The activities of both constitutive elements in the Al-V system showed a strong negative deviation from the ideal behaviour which indicates that a good mixing ability existed between components. The enthalpies of formation of all intermetallic phases were negative for the entire composition range. The predicted phase diagram and thermodynamic properties determined in this work were fairly in agreement with what is reported in the literature.

The microstructural analysis through both LOM and SEM indicated the dendritic structure, the same morphology was observed after the DSC-TG test. The quantitative determination of the elemental composition of each phase by EDX analysis revealed that the average elemental composition of the alloy was 63 ± 0.05 wt. % and 37± 0.05 wt. % for Al and V, respectively. With this composition, the master alloy produced was close to the theoretical 60Al-40V master alloy. The XRD technique revealed diffraction peaks principally of two intermetallic compounds, namely, the Al_3V and Al_8V_5 phases, and was confirmed by SEM/EDX analysis. Phase transitions of the intermetallic phases formed in the material were observed and their invariant temperatures were determined by the DSC-TG analysis. The DSC-TG trace curves showed peaks during both the heating and cooling process and the peritectic temperatures obtained correspond with the invariant reactions of the intermetallic $Al_{21}V_2$, Al_3V and Al_8V_5 phases as predicted by the Thermo-Calc™ software. The obtained results show that the most stable phase found at high temperature was identified to be the Al_3V phase. A good agreement between the calculated phase diagram, using the Thermo-Calc™ software, and experimental data was achieved.

3. PUBLICATIONS

Conference proceedings and presentation

T.O. Mapoli, K.A. Annan, C.W. Siyasiya, and K. Mutombo, “Preparation and microstructural characterization of the 60Al-40V master alloy” IOP Conf. Ser. Mater. Sci. Eng., vol. 655, no 1, PP 1-8, 2019

4. DEDICATION

I dedicate this research project to my late father, Professor Achukani Okabo Jean-Rene (1950-2010)

5. ACKNOWLEDGEMENTS

First, unto the Lord Almighty, to whom I give all the glory and praise for He has taken me up to this far, Ebenezer.

The following contributions are gratefully acknowledged: In a very special way, I would like to convey sincere gratitude and appreciation to Prof Charles Siyasiya, Dr Kofi A. Annan, and Dr Kalenda Mutombo respectively supervisor and co-supervisors for their guidance, support, and unmeasurable encouragement throughout this master's research program. The Materials Science and Metallurgical Engineering department of the University of Pretoria for providing equipment and guidance. To Mr Carel and Mr Lwazi of IMMRI, thank you for the training in the use of equipment. To Mrs Wiebke Grote, X-ray diffraction analyst at the XRD and XRF facility, thank you for the XRD work and to Prof Johan de Villiers, I greatly appreciate all the assistance received for the interpretation of the XRD data. To Eudri Venter and Chantelle Venter in the Physics department at the University of Pretoria for their assistance with the SEM/EDX analysis at the microscopy Centre.

I am grateful to Dr Kobus Wagener and Mr Benni Vilakazi at the Nuclear Energy Corporation of South Africa (NECSA) for their assistance with the DSC-TG thermal analysis experiments on the master alloy performed at their facilities.

I would also like to extend my appreciation to my colleagues in the Physical Metallurgy group in the department of Materials Science and Metallurgical Engineering at the University of Pretoria, namely Ms Kedibone Lekganyane, Mr Patrick Edwin Kambilinya and Mr Tulani Mukarati for openly sharing research ideas and contributions which have been beneficial to the realisation of this work.

To my family, my gratitude goes to my mother and my sister namely: Esther Tshela Tshibwabwa and Nathalie Tshela Tshibwabwa, for their emotional and financial support and for always believing in me. My gratitude goes also to my brother Gracia Achukani, my lovely niece Mercia Kasamiro and all my aunties, uncles, cousins, and their respective families for their great support during my study. Of final and most importantly, to my fiancée and wife to be Sara Lubaba Mukalay for her emotional support and patience during the writing of this project.

To everyone left out, please consider yourself as being of help and receive my appreciation.

6. TABLE OF CONTENTS

CHAPTER 1. INTRODUCTION 1

1.1 Background 1

1.2 Problem statement 3

1.3 Motivation 4

1.4 Aim of the study 4

1.5 Objectives 4

1.6 Thesis outline. 5

CHAPTER 2. LITERATURE REVIEW 6

2.1 The Al-V phase diagram. 6

2.2 Thermodynamic properties 11

2.2.1 Theory and relationships between thermodynamic properties 11

2.2.2 Thermodynamic data of the Al-V binary system 13

2.3 Microstructures and phases in the Al-V system 15

2.4 Thermodynamic calculations 21

2.4.1 The Thermo-Calc^{TM} software. 21

2.4.2 The Thermo-Calc^{TM} database and usage 23

2.5 Basic thermal analysis 24

2.5.1 Differential scanning calorimetry (DSC) 24

2.5.2 Simultaneous thermal analysis (STA) 27

2.6 Manufacture technologies of high-temperature materials. 27

2.6.1 Melting and casting technology 28

2.6.2 The possible manufacturing processes of the Al-V alloys in industry. 29

CHAPTER 3. RESEARCH METHODOLOGY 31

3.1 Thermodynamic calculations 31

3.2 Raw materials and master alloy preparation (using the aluminothermic process) 31

3.3 Characterisation of the produced 60Al-40V master alloy 32

3.3.1 Chemical analysis 32

3.3.2 Microstructural and phase analysis 33

3.3.3 Thermal analysis 33

3.3.4 Microhardness testing 34

CHAPTER 4. RESULTS 35

4.1 Phase transformation predictions using Thermo-Calc™ software. 35

4.1.1 Phase diagram 35

4.1.2 Thermodynamic properties 38

4.1.3 Expected intermetallic phases in the Al-V alloy as a function of composition. 43

4.2 Characterisation of the aluminothermy produced 60Al-40V master alloy. 43

4.2.1 Chemical composition 43

4.2.2 Microstructural and phases analysis of the as-received master alloy. 45

4.2.3 Microstructures and EDX results after DSC-TG thermal analysis. 51

4.2.4 Thermal Analysis 57

4.3 Microhardness 59

CHAPTER 5. DISCUSSION 61

5.1 Expected intermetallic phases based on the thermodynamic predictions. 61

5.2 Microstructures and phases in the produced Al-V master alloy 62

CHAPTER 6. CONCLUSIONS AND RECOMMENDATIONS 66

6.1 Conclusions 66

6.2 Recommendations 66

CHAPTER 7. REFERENCES 68

CHAPTER 8. APPENDIX A 84

8.1 SEM-EDX analysis (point count analysis) 84

8.2 SEM-EDX analysis 100

8.3 SEM-EDX analysis after DSC-TG tests 103

8.4 DSC-TG thermal analysis 107

7. LIST OF FIGURES

Figure 2-1: The Al-V phase diagram according to Murray [56] 6
Figure 2-2: The Al-V phase diagram according to Murray and adopted by Willey [62] 7
Figure 2-3: The Al-V phase diagram by Okamoto comparing Murray (solid lines) and Richter (dashed lines) [57], [61]. 8
Figure 2-4: The (Al) solid solution phase in the Al-V alloy etched with KOH at 250 magnification [88]. 16
Figure 2-5: The $Al_{21}V_2$ phase in the Al-V alloy etched with KOH at 250 magnification [88]..... 17
Figure 2-6: The typical morphology of the $Al_{45}V_7$ in Al-23. wt.% V alloy quenched at 710 °C, etched with Kroll reagent at 250 magnification [88]. 18
Figure 2-7: The Al_3V phase in the Al-V alloy etched with Kroll reagent at 250 magnification. [88] 19
Figure 2-8: The Al_8V_5 phase in the Al-V alloy etched with Kroll reagent, at 250 magnification [88]. 20
Figure 2-9: The (V) phase observed in the V-rich Al-V alloy quenched at 900 °C at high and low magnification respectively [88]. 21
Figure 2-10: Frame-work of the Thermo-Calc™ software program based on the Calphad method [93]. 22
Figure 2-11: Schematic diagram of heat flux differential scanning calorimetry (DSC)..... 25
Figure 2-12: DSC plot for polyethylene terephthalate (PET) showing both the exothermic and endothermic reactions occurring during a temperature scan from 50 -300 °C [104]. 26
Figure 4-1: The Thermo-Calc™ predicted Al-V phase diagram. 36
Figure 4-2: The volume fraction of all phases in the Al-V binary system as a function of temperature. 38
Figure 4-3: The variation of the calculated Gibbs free energy (phase stability) of the phases as a function of the mole fraction of V. 39
Figure 4-4: The change in the calculated enthalpy of formation of the Al-V binary system as a function of the mole fraction of V. 40
Figure 4-5: The activity of (a), (c) the V element and (b), (d) of the Al element, in the Al-V binary system as a function of mole fraction of V and Al, respectively. 42

Figure 4-6: Micrograph of the as-cast 60Al-40V master alloy produced by the aluminothermic process..... 46
Figure 4-7: SEM micrographs of the 60Al-40V master alloy at low and high magnifications, (a) and (b) respectively..... 47
Figure 4-8: (a) Micrograph and (b) the EDX spectrum taken from region 1. 47
Figure 4-9: SEM-EDX electron image (Scan 1), (a) elemental distribution, (b) Al K series, (c) V K series of the master alloy, (d) the average elemental composition of the scanned area (scan 1). 49
Figure 4-10: The optical micrographs a) before the DSC-TG test, and b) after the DSC -TG test at a temperature of 1300 °C 51
Figure 4-11: SEM micrographs of the 60Al-40V master alloy, (a) before DSC-TG test; (b) after DSC-TG test at 1100, (c) at 1300, and (d) at 1400 °C, respectively. 52
Figure 4-12: (a) SEM image, and EDX- spectra of (b) the grey (A), (c) light grey (B) (d) dark grey phase (C) after the DSC-TG test at the temperature of 1300 °C 53
Figure 4-13:An illustration of the volume fraction of the Al_3V phase through thresholding procedure using the Image J ® software (a) before, and after DSC-TG test, (b) at 1100, (c) 1300, (d) 1400 °C, respectively. 55
Figure 4-14: The Volume fraction of the Al_3V phase as a function of temperature..... 56
Figure 4-15: XRD spectrum of the as-cast 60Al-40V master alloy obtained by X' Pert High Score Plus software..... 57
Figure 4-16: The change in the heat flow of the 60Al-40V master alloy as a function of temperature showing the phase stability, (a) for the 1^{st} heating-cooling cycle, (b) for the 2^{nd} heating-cooling cycle up to the temperature of 1300 °C. 58
Figure 8-1: SEM-EDX electron image (region 1) 84
Figure 8-2: Spectrum 1- chemical composition analysis..... 85
Figure 8-3: Spectrum 2 - chemical composition analysis..... 86
Figure 8-4: Spectrum 3 - chemical composition analysis..... 87
Figure 8-5: Spectrum 4 - chemical composition analysis..... 88
Figure 8-6: Spectrum 5 - chemical composition analysis..... 89
Figure 8-7: Spectrum 6 - chemical composition analysis..... 90

Figure 8-8: Spectrum 7- chemical composition analysis 91
Figure 8-9: Spectrum 8 - chemical composition analysis 92
Figure 8-10: Spectrum 9- chemical composition analysis 93
Figure 8-11: SEM-EDX electron image (zone 2) 94
Figure 8-12: Spectrum 16- chemical composition analysis 95
Figure 8-13: Spectrum 17-chemical composition analysis 96
Figure 8-14: SEM-EDX electron image (zone 3) 97
Figure 8-15. Spectrum 22- chemical composition analysis 98
Figure 8-16. Spectrum 23-chemical composition analysis 99
Figure 8-17: SEM-EDX electron image, (a) elemental distribution map, (b) Al K series, (c) V K series of the master alloy, and (d) the average elemental composition of the scanned area (scan 2) 100
Figure 8-18: SEM-EDX electron image, (a) elemental distribution map, (b) Al K series, (c) V K series of the master alloy and (d) the average elemental composition of the scanned area (scan 3) 101
Figure 8-19: SEM-EDX electron image, (a) elemental distribution map, (b) Al K series, (c) V K series of the master alloy and (d) the average elemental composition of the scanned area (scan 4) 102
Figure 8-20: (a) SEM micrograph, and EDX spectra of (b) grey phase, (c) light grey phase, (d) dark grey phase after the DSC-TG test at the temperature of 1100 °C..... 103
Figure 8-21: (a) SEM micrograph, and EDX spectra of (b) the grey phase, (c) light grey and (d) dark grey phase after the DSC-TG test at the temperature of 1400 °C..... 105
Figure 8-22: The change in the heat flow of the 60Al-40V master alloy as a function of temperature at the temperature of 1100 °C 107
Figure 8-23: The change in the heat flow of the 60Al-40V master alloy as a function of temperature at the temperature of 1400 °C. 107

8. LIST OF TABLES

Table 2-1: Invariant phase reactions and melting temperatures of compounds in the Al-V binary system. 10
Table 2-2: Enthalpies and entropies of formation of phases in the Al-V binary system. 14
Table 2-3: Phase properties in the Al-V system 15
Table 4-1: Structural information in the Al-V phase diagram using Thermo-Calc™. (This work) 37
Table 4-2: Peritectic melting temperatures of compounds in the Al-V system 37
Table 4-3: The chemical composition AMETEK standard specification of the 60Al-40V master alloy [137]. 43
Table 4-4: Elemental chemical composition analysis by ICP of the produced 60Al-40V master alloy (this work) 44
Table 4-5. Oxygen content in the 60Al-40V master alloy analyzed using Leco TECH 600, the values are an average of three counts. 45
Table 4-6: Summary of phases and elemental compositions according to the EDX analysis 48
Table 4-7: EDX mapping analysis- Summary of the elemental chemical composition in the produced Al-V master alloy. 50
Table 4-8: Summary of phases formed in the material and elemental chemical compositions of the intermetallic phases obtained after the DSC-TG test at the temperature of 1300 °C. 54
Table 4-9: Peritectic temperatures [°C] of the compounds in Al-V alloys obtained by DSC-TG tests vs Thermo-Calc™ predictions. 59
Table 8-1. EDX analysis results for zone 1- spectrum 1 85
Table 8-2. EDX analysis results for zone 1- spectrum 2 86
Table 8-3. EDX analysis results for zone 1- spectrum 3 87
Table 8-4. EDX analysis results for zone 1- spectrum 4 88
Table 8-5. EDX analysis results for zone 1- spectrum 5 89
Table 8-6. EDX analysis for zone 1- spectrum 6 90
Table 8-7. EDX analysis results for zone 1- spectrum 7 91
Table 8-8. EDX analysis results for zone 1- spectrum 8 92
Table 8-9. EDX analysis results for zone 1- spectrum 9 93

Table 8-10. EDX analysis results for zone 2- spectrum 16 95
Table 8-11. EDX analysis results for zone 2- spectrum 17 96
Table 8-12. EDX analysis results for zone 3- spectrum 22 98
Table 8-13. EDX analysis results for zone 3- spectrum 23 99
Table 8-14. EDX analysis after DSC-TG test at a temperature of 1100 °C 104
Table 8-15. EDX analysis after DSC-TG test at the temperature of 1400 °C 106
Table 8-16. Summary of the elemental composition obtained from different spectra after DSC-TG analyses at temperatures of 1100 and 1400 °C, respectively. 106

9. ABBREVIATIONS

The abbreviations used in the present study in alphabetical order are listed below.

Al:	Aluminium
AM:	Additive manufacturing
ASTM:	American standards for testing and materials
bcc:	body centered cubic.
BE:	Blended elemental
BSE:	Backscattered electrons
CALPHAD:	Calculations of Phase diagrams
CP-Ti:	Commercially pure titanium
CSIR:	Council for Science and Industrial Research
DFT:	Density functional theory
DSC:	Differential scanning calorimetry
DTA:	Differential thermal analysis
EBM:	Electron bean melting
EBSD:	Electron backscattered diffraction
EBSDP:	Electron backscattered diffraction pattern
EDX:	Energy dispersive spectroscopy
EMF:	Electromotive force
EMPA:	Electron microprobe analyzer
fcc:	face centered cubic.
hcp:	hexagonal closed packed
ICP:	Inductively coupled plasma mass spectrometry.
LOM:	Light optical microscopy

NBSA:	Nickel-based superalloys
NECSA:	Nuclear Energy Corporation of South Africa
PA:	Pre-alloyed
PM:	Powder metallurgy
RPM:	Revolutions per minute
SEM:	Scanning electron microscopy
SER:	Stable element reference
SGTE:	Scientific Group Thermodata Europe
SiC:	Silicon Carbide
STA:	Simultaneous thermal analysis
TEM:	Transmission electron microscope
TG:	Thermogravimetry analysis
Thermo-Calc^{TM}:	Commercial Thermodynamic calculation program
Ti:	Titanium
V:	Vanadium
WDS:	Wavelength dispersive X-ray spectroscopy
XRD or XRPD:	X-ray powder diffraction
XRDP:	X-ray powder diffraction pattern

CHAPTER 1. INTRODUCTION

1.1 Background

The structural performances required for automobile and aerospace components are mechanical properties such as high strength retention, and corrosion resistance at ambient and high temperatures [1]. Alloys are designed to principally reduce the weight of materials and the overall cost of production of constituent materials while upholding their important properties. The optimisation of the alloy design is achieved when the overall cost of manufacturing is achieved while improving the properties of the alloy [2], [3]. Metal alloys are designed for applications requiring specific mechanical properties such as high strength, high-temperature resistance and high corrosive resistance [4]. However, the improvement of mechanical properties such as high strength comes at the expense of lowering the ductility and toughness of materials which is the penalty to be paid. Over the last two decades, there has been an increased interest in the use of Ti-based alloys for various applications due to their lightweight, oxidation resistance and high-temperature strength retention [5]. The wide range of industries in which light metals have gained increased attention in regards to these alloys includes automobile, aerospace [6], the general transport industry [7], households [8], and medicine [9]. One area that is attracting research is the design of alloys, in particular of their intermetallic phases due to their beneficial mechanical properties. Intermetallic phases exhibit superior characteristics such as low density, mechanical properties such as high strength and resistance against oxidation at elevated temperatures [4], [10].

Alloys with predominantly intermetallic phases are considered to fill the gap between superalloys and ceramics with respect to high-temperature applications and mechanical properties [11]. Intermetallic systems that have been studied widely include N_3Al, NiAl, Pt_3Al, PtAl, Ti_3Al, TiAl, Al_3V and AlV [12]. Ti and its alloys can also be defined as newly developed materials of very high tensile strength and toughness required applications [13]. Ti alloys stand out due to two main properties: high strength retention and outstanding corrosion resistance [14]. Ti and its alloys are widely investigated because of their attractiveness and abundant availability as an ore [15]. Amongst Ti alloys, the Ti-6Al-4V is considered as a workhorse metal that is used in a wide range of applications such as in the automobile [16], aerospace [17]–[19], marine, chemical and

biomedical industries [9], [20]–[22]. The Ti-6Al-4V has good tensile strength and toughness at temperatures below 600 °C, therefore, it is considered a high-temperature resistant material in this specific range of temperature.

In the production of Ti alloys, three classes of powder metallurgy (PM) feedstock can be distinguished namely, commercially pure (CP), pre-alloyed (PA) and blended elemental (BE) [23]. For the Ti-6Al-4V alloy, the two latter distinct PM methods can be used [24], namely the pre-alloyed (PA) and blended elemental (BE) approach. In the first method, the 60Al-40V alloy is used as raw materials and added to pure Ti to produce the Ti-6Al-4V [25]. Hence the pre-alloyed 60Al-40V, which is a master alloy is considered as a semi-finished product in the Ti industry [26].

Depending on the desired properties to be achieved, a specific production route is chosen for the manufacturing of the semi-finished product. The master alloy to be produced must contain 60 wt. % Al and 40 wt. % V, respectively. Master alloys are mainly used to adjust the alloy composition, to influence the as-cast-structure [27] and grain structure [28]. In Al-V alloys, the V is added to Al to improve the resistance to fatigue and homogeneity. The V also raises the crystallisation temperature and retards grain growth at elevated temperatures [29], [30]. Methods used to produce Al-based master alloys include mixing processes [31]–[33], sintering and mechanical alloying methods [34]. However, the high cost of the alloying elements and high material loss during the alloying process are the main disadvantages of these processes [35]. The two-steps process namely the aluminothermic-vacuum melting method allows obtaining Al-based master alloys that are highly pure, homogeneous, and with the lowest possible content of impurities [36]. However, these processes are complicated, and the cost involved is also high [37]. Therefore, the aluminothermic reaction process has been considered as an effective technique to use in the production of master alloys [38]–[40] because of reduced production costs.

The Al-V alloys are important pre-alloyed elements that use Al and V as basic elements in the making of the famous Ti-6Al-4V alloy, generally produced through an aluminothermic smelting process in which a refractory-lined or water-cooled copper vessel is used [41]. The 60Al-40V master alloy has been in considerable demand to develop Ti-6Al-4V and the aluminothermic reaction process can be proposed as a technique that can be used to produce the 60Al-40V master alloy.

The aluminothermy is a process for reducing metal oxides such as vanadium pentoxide (V_2O_5) using Al metal, the ignition of the mixture of Al and oxides causes the Al to be oxidised and the metal oxide to be reduced to the metal [42]. In the production of the alloy, V_2O_5 and Al metal needed to be mixed in such proportions to produce an exothermic reaction capable of generating the Al-V master alloy [43], [44]. The greater the affinity of oxygen to Al to form a metal oxide, the higher is the rate of reaction [40]. On the other hand, V can readily react and absorb oxygen (O), nitrogen (Ni), and carbon (C) [45], which are considered impurities. The reduction of V oxides in the electrical furnace leads to high carbon content, hence the aluminothermy technique is considered as an effective way to produce the 60Al-40V master alloy provided a suitable reaction vessel is available. In the process, an exothermic reaction in which Al metal and V_2O_5 mixed in the right proportion occurs to yield 60 wt. % Al and 40 wt. % V and slag rich in Al_2O_3.

However, it can be noted that experimental investigation to produce new alloys can be expensive and time-consuming because of the multiple possible combinations of the composition, the process, and the parameters for their production. Therefore, computational analysis using thermodynamic computer software and simulation [46] such as Thermo-Calc^{TM} can be an effective way to resolve the problem. Thermodynamic calculations using Thermo-Calc^{TM} software and database [47] prove to be a powerful tool that has long been used to quantitatively predict microstructural evolution [48] and the phases present in the material and thermodynamic properties of materials both in academia and industry [49]–[51]. This method gives expected results while greatly reducing experimental work through the selection of optimal compositions and temperatures. During the past decades, investigations on the development of thermodynamic models for the so-called binary and multicomponent alloys have been investigated and developed [47], [52]. These models are aimed at facilitating an easy prediction of microstructures, phases, and thermodynamic properties of materials.

1.2 Problem statement

The phase diagram and thermodynamic properties of systems are determined by empirical and numerical methods. However, there are deviations from the predicted phases and properties under non-equilibrium conditions. In the case of the Al-V system [53], although the basic phase diagram of the system has been fairly well-characterised, in which the solubility limit of V in Al liquid is well known, details of the liquidus line on the Al-rich side of the system remain unclear. The phase

diagrams available in the literature still show many uncertainties, particularly of the intermetallic phases. Therefore, due to the contradictions reported in the literature, the Al-V binary system's phases, thermodynamic properties, and activities of the elements in the system need to be more accurately established in order to achieve a more efficient production process of the Al-V master alloy for the production of the Ti-6Al-4V alloy. The aluminothermic process which is industrially used for the production of superalloys and iron-based alloys has been proposed to be used for the production of Al-V master [54], [55]. There is, however, limited information on the feasibility and the reliability of the aluminothermic process as a technique for the production of the 60Al-40V master alloy. This study seeks to present the phases and microstructures which are major determinants of the properties of the Al-V alloy that have not been identified for this alloy produced through the aluminothermic process.

1.3 Motivation

During the production of Al-V master alloy, intermetallic phases such as $Al_{21}V_2$, $Al_{45}V_7$, $Al_{23}V_4$, Al_3V, and Al_8V_5 are expected to form during phase transformations. To develop and produce the Al-V master alloy, it is necessary to determine the thermodynamic parameters (pressure, temperature, volume, etc.) at which thermodynamically distinct phases occur and coexist at equilibrium. This is in general presented in the form of a phase diagram. Phase diagrams' calculation of systems is proven to be principally based on thermodynamic models. Therefore, the phase diagram has become one of the most used and important tools for the development and improvement of materials. In this regard, this study focused on investigating the microstructures, phases, and thermodynamic properties of the Al-V binary system through experimental and computational calculations.

1.4 Aim of the study.

The study aims to calculate thermodynamic parameters using thermodynamic prediction software and analytical characterisation techniques to assist in the development and production of the 60Al-40V master alloy.

1.5 Objectives

The objectives of this study were:

- To produce the Al-V master alloy which must contain 60 wt.% Al and 40 wt. % V through the aluminothermic process;
- To predict the phases in the Al-V system using thermodynamic software;
- To calculate thermodynamic parameters such as Gibbs free energy and enthalpy of formation of Al-V intermetallic phases;
- To calculate the activities of the Al and V elements in the Al-V binary system;
- To determine the phases and characterise the microstructures of the 60Al-40V master alloy through thermal analysis and advanced material characterisation techniques and;
- To experimentally confirm thermodynamic predictions of the phases in the Al-V alloy system.

1.6 Thesis outline.

The thesis is subdivided into the following chapters: Chapter One is an introduction that provides the background of the study, problem statement, motivation, research aim and objectives, and outline of the research project. Chapter Two gives a literature review of the Al-V phase diagram, thermodynamics, microstructure and phases in the Al-V alloys, characterisation methods and thermal analysis of the Al-V master alloy as well as possible manufacturing techniques of Al-V intermetallic compounds. Chapter Three presents the methodology followed in this research work, which consists of thermodynamic calculations using Thermo-Calc^{TM} software, material characterisation techniques and thermal analysis. Chapter Four presents the research findings. Chapter Five discusses the results of thermodynamic calculations using the Thermo-Calc^{TM} software and those obtained experimentally. Chapter Six focuses on the conclusions and recommendations drawn from this work.

CHAPTER 2. LITERATURE REVIEW

2.1 The Al-V phase diagram.

The Al-V phase diagram is significant in the design and development of the Al-V alloy, with respect to the improvement of the manufacturing process [56]–[58]. The Al-V binary system is an essential subsystem of the ternary Ti-Al-V system and, therefore, a good knowledge of the binary phase diagram and thermodynamic data of the system is essential [59]. The different Al-V phase diagrams reported in the literature by several authors [56]–[64] contains eight stable phases namely, the liquid, the fcc (Al) and bcc (V) solid solution, and five intermetallic phases, namely the $Al_{21}V_2$, $Al_{45}V_7$, $Al_{23}V_4$, Al_3V, and the Al_8V_5. Figure 2-1 illustrates the assessed Al-V phase diagram based on experimental data [56].

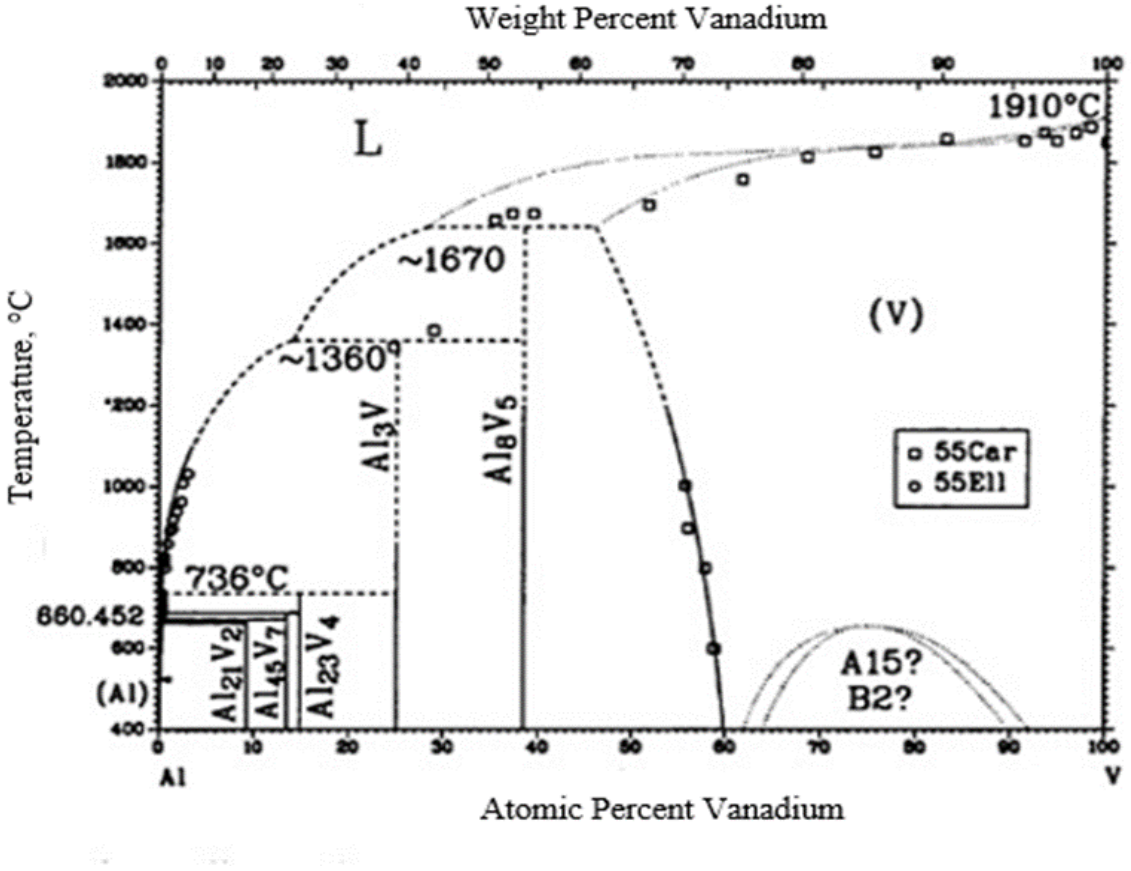

Figure 2-1: The Al-V phase diagram according to Murray [56]

Several authors have investigated the Al-V binary system. Supplementary investigation of the phase diagram was essential because of significant disagreement between the calculated phase diagrams [56] and the experimentally reported data [57], especially for the peritectic melting point of the two high-temperature intermetallic phases, i.e. Al_3V and the Al_8V_5. Furthermore, according to Okamoto [53], the intermetallic Al_3V phase has not been discussed in all its thermodynamic models, the reason being that the phase boundaries of the intermetallic Al_3V phase were merely copied from the phase diagram constructed by Murray [56]. A detailed review of the Al-V phase diagram based on that Al-V phase diagram proposed by Murray is given by Willey [62], illustrated in Figure 2-2.

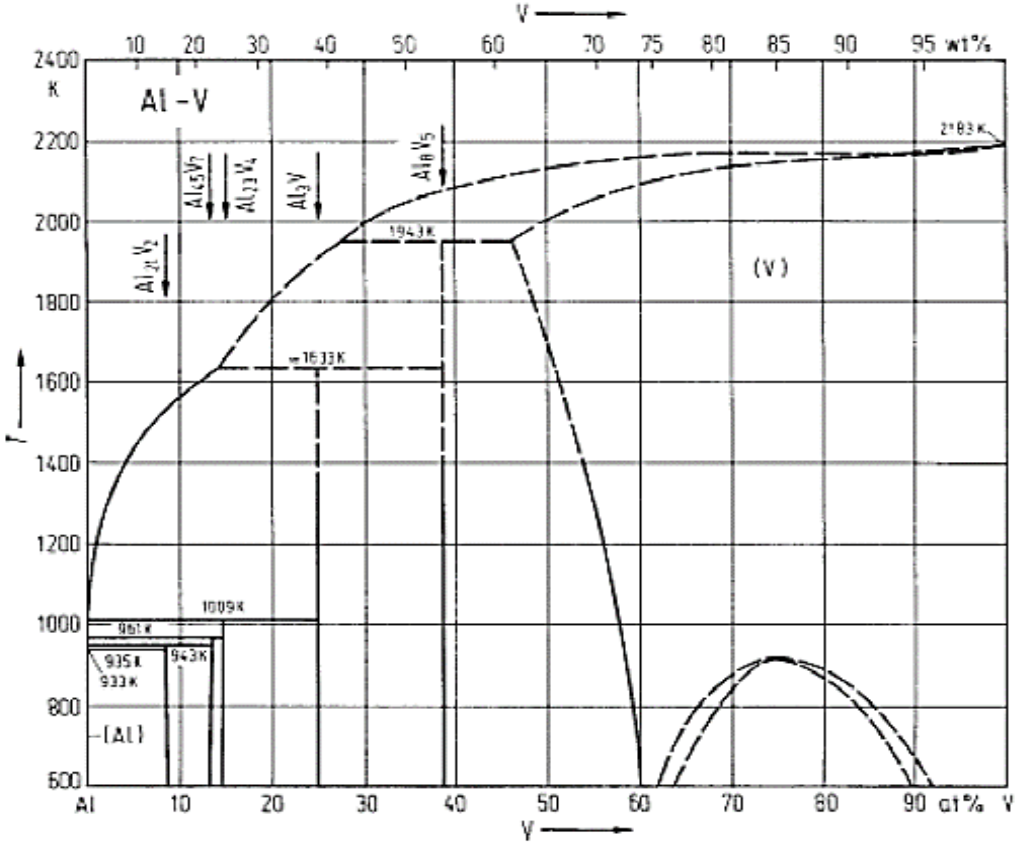

Figure 2-2: The Al-V phase diagram according to Murray and adopted by Willey [62]

Figure 2-2 provides a detailed review of the Al-V phase diagram adopted by Willey according to the Al-V phase diagram proposed by Murray and reported in Massalki's handbook of Binary Alloy phase diagrams [62]. Further investigations were needed because of the disagreement with the

experimental results that were reported in the Murray assessment [56]. The Al-V phase diagram was reviewed by Okamoto [61], using techniques such as differential thermal analysis (DTA), X-Ray diffraction (XRD) and electron probe microanalysis (EMPA). In the phase diagram as illustrated in Figure 2-3, Okamoto reinvestigated the Al-V phase diagram developed by Murray (dashed lines) and Richter (solid lines) for a composition range between 0-50 wt. % V. It was observed that the difference between the two-phase diagrams is significant considering the melting temperatures of Al_3V and Al_8V_5 phases [61]. Additionally, experimental data is required for the (V) liquidus and solidus in the completion of the phase diagram proposed by Richter [57].

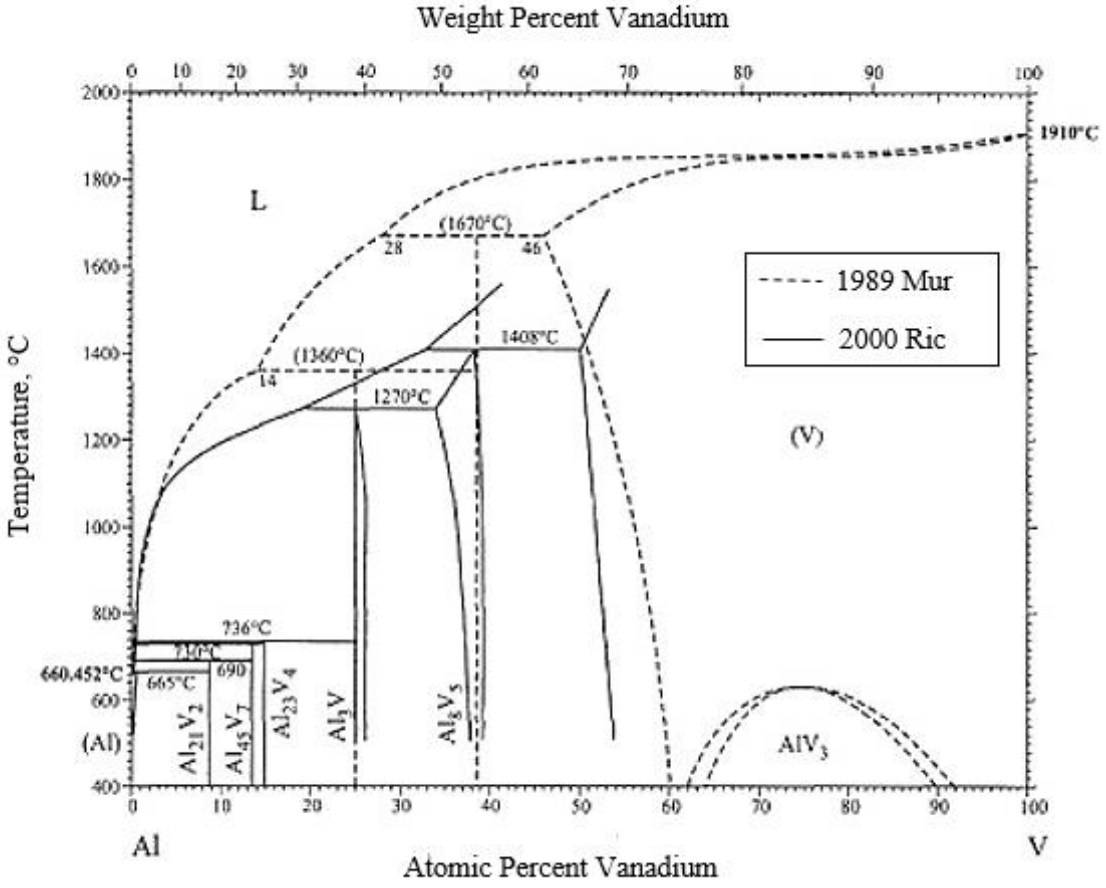

Figure 2-3: The Al-V phase diagram by Okamoto comparing Murray (solid lines) and Richter (dashed lines) [57], [61].

Several groups of researchers have repeatedly investigated the Al-V phase diagram based on microstructural observations, XRD and thermal analysis. In their study, Carlson et al. [63] determined the phase diagram of the Al-V system for the temperature of 600 °C and above. The change of the lattice parameter of the bcc (V) was considered and the phase boundary of the solid solution of Al in V was determined. It was observed that for the temperature of 600 °C, the composition of Al in V was 42.0 at. % and for the temperature of 800 °C was 43.5 at. %. The compositions for higher temperatures such as 900 and 1000 °C were 45.0 and 46.0 at. % Al, respectively. They also noticed the presence of a homogenous Al_8V_5 phase, although concise data was not proven [63].

Richter and Isper [64], on the other hand, investigated the system for the temperature range of 630 and 1050 °C and noticeable differences in the invariant reaction temperatures were observed. It was also observed that all the intermetallic phases melt peritectically except the two intermetallic phases, namely the Al_3V and the Al_8V_5, for which a small homogeneity range was observed. The measurements of the solubility of the Al in V have been found to be 48.5 at. % for the temperature of 1050 °C. Gong et al. [65] performed a thermodynamic reassessment of the Al-V phase diagram by optimising the results of Carlson [63] and Richter [64], on the maximum solubility of Al in bcc (V), reaching the temperature of the peritectic decomposition of the Al_8V_5 for a composition range 50 at. % Al compared to 54 at. % found by Carlson [63]. It was also found that there was a decrease in the at. % Al content in (V) to 46.5 and 39.0 for the temperatures of 1050 and 500 °C, respectively [65]. It was observed that the solubility limit of Al in bcc (V) increases with temperature increase.

Considering the various Al-V phase diagrams reported in the literature by several authors, three peritectic points and five intermetallic line compounds of the Al-V can be distinguished. In the Al-V phase diagram, eight distinct phases are formed, which includes the liquid, the Al (fcc) and V (bcc) and five intermetallic phases.

The six invariant reactions are characterised and described by the following equations:

$$L+Al_{21}V_2 \rightarrow Al\_fcc \qquad \text{Equation 2-1}$$

$$L+Al_{45}V_7 \rightarrow Al_{21}V_2 \qquad \text{Equation 2-2}$$

$$L+Al_{23}V_4 \rightarrow Al_{45}V_7 \qquad \text{Equation 2-3}$$

$L+Al_3V \rightarrow Al_{23}V_4$ Equation 2-4

$L+Al_8V_5 \rightarrow Al_3V$ Equation 2-5

$L+V\_bcc \rightarrow Al_8V_5$ Equation 2-6

The invariant phase reactions and peritectic melting temperatures of the compounds formed in the Al-V system are summarised in Table 2-1.

Table 2-1: Invariant phase reactions and melting temperatures of compounds in the Al-V binary system.

Phase reactions	Melting temperatures [°C]	Reference
$L+ Al_{21}V_2 \rightarrow (Al)$	660.45	[37], [56]
	664	[53], [57]
	665	[61], [64]
$L+ Al_{45}V_7 \rightarrow Al_{21}V_2$	670	[56]
	687	[53], [57]
	690	[61], [64]
$L+ Al_{23}V_4 \rightarrow Al_{45}V_7$	688	[37], [56]
	721	[53], [57]
	730	[61], [64]
$L+ Al_3V \rightarrow Al_{23}V_4$	734	[37], [61], [64]
	736	[53], [56], [57]
$L+ Al_8V_5 \rightarrow Al_3V$	1249	[53], [57]
	1270	[61], [64]
	1360	[56], [63]
	1362	[37]
$L+(V) \rightarrow Al_8V_5$	1405	[53], [57]
	1408	[61], [64]
	1670	[56], [63]
	1673	[37]

2.2 Thermodynamic properties

2.2.1 Theory and relationships between thermodynamic properties

Thermochemical and thermophysical properties present only indirect information about the structure of liquid solutions. However, the thermodynamic study of systems also includes parameters such as the activity of the constitutive elements, the Gibbs free energy of solutes and heat of formations such as enthalpies and entropies. These thermodynamic properties are essential parameters that contribute to a better understanding of the role of solutes in the molten solvents and of systems in general.

1. **Gibbs free energy: enthalpy and entropy relation**

The Gibbs free energy of a system at any moment in time is defined as the enthalpy of the system minus the product of the temperature times the entropy of the system. The Gibbs free energy (G) therefore determines, the stability of a phase considering other thermodynamic quantities such as the enthalpy (H) and the entropy (S) [66].

$$G = H - TS \qquad \text{Equation 2-7}$$

The free energy of a system is a state function because it is defined in terms of thermodynamic properties, which are state functions. The changes in the free energy of the system that occurs during a reaction measure the balance between the two driving forces that determine whether a reaction is spontaneous. These changes can be measured under any set of conditions. In the standard-state conditions, the standard-state free energy of reaction (ΔG^o) is expressed as follows [67]:

$$\Delta G^o = \Delta H^o - T\Delta S^o \qquad \text{Equation 2-8}$$

Considering equation 2-8, in which the free energy of the system is defined in terms of change in enthalpy and entropy, ΔG^o is negative for any reaction for which ΔH^o is negative and ΔS^o is positive. ΔG^o is therefore negative for any reaction that is favoured by both the enthalpy and entropy terms. We can therefore conclude that any reaction for which ΔG^o is negative should be favourable, or spontaneous [66]. Conversely, ΔG^o is positive for any reaction for which ΔH^o is positive and ΔS^o is negative which makes $\{-T\Delta S^o\}$ positive, and any reaction for which ΔG^o is positive is therefore unfavourable.

2. Gibbs free energy: activity of components

At a given temperature and pressure, the Gibbs free energy of a system also depends on the mole fraction (X_i) and the chemical potential (α_i) of the system for a certain number of components (i) in the system and it is given by the relationship [68]:

$$\Delta G = \Sigma_i a_i \Delta X_i \qquad \text{Equation 2-9}$$

where α_i is the chemical potential and X_i the mole fraction of component i, for i=1, 2, 3…. i

The total change in the Gibbs free energy is given by the sum of the partials in which free energy changes with the change of the instantaneous mole fractions.

$$\Delta G = \left(\frac{\Delta G}{\Delta X_i}\right) X_2, X_3 \ldots X_i \Delta X_i + \left(\frac{\Delta G}{\Delta X_2}\right) X_1, X_3 \ldots Xi \Delta X_2 + \left(\frac{\Delta G}{\Delta X_i}\right) X_1, X_2, X_3 \Delta X_i \qquad \text{Equation 2-10}$$

The chemical potential (α_i) of any component (i) in which mole fraction (X_i) of the other component remains unchanged in the system, yields the following equations:

$$\alpha_i = \frac{\Delta G}{\Delta X_i} X_2, X_3 \ldots \qquad \text{Equation 2-11}$$

The thermodynamic parameters change in alloy prediction and existing models have been used to explain these changes. Thermodynamically, an ideal solution is defined as one in which the activity of each component (a_i) is equal to the mole fraction of that component in the solution (X_i) at all concentrations and temperatures.

$$a_i = Xi, \ 0 \leq X_i \leq 1 \qquad \text{Equation 2-12}$$

In an ideal solution, the enthalpy of mixing is zero for all ranges of composition and temperature while the entropy of mixing is equivalent to the perfect random mixing of the components. However, in practice, very few systems approach ideality. In intermetallic systems, an ideal solution is thus a limiting case, and deviations are physically interesting. The basic concept of zero excess entropy involving the random distribution of atoms is unrealistic where there is a large deviation from Raoult ‘s law. Many models used to describe systems such as the regular solution model and the sub-regular model, are used to qualitatively describe the heat of mixing with many binary alloys [69].

2.2.2 Thermodynamic data of the Al-V binary system

Fewer investigations have been done on the Al-V binary system about the experimental determination and thermodynamic properties. Previously, the thermodynamic properties of the Al-V system were studied through first-principle methods by Wang et al.[70], including the elastic properties by Wang et al. [71] and Jahnatek et al.[72]. There is a lack of adequate information in the literature on thermodynamic properties such as enthalpy, entropy, and Gibbs free energy of the liquid Al-V phase of the system. Enthalpies of formation (ΔH_f) for the Al-V alloy system have been experimentally determined using calorimetry by Kubaschewski et al. [73] for the composition range between 40-75 wt. % Al. Neckel and Nowotny [74], determined the enthalpies of formation of the solid alloys in the composition range between 24-38 at. % V.

Meschel and Kleppa [75], on the other hand, measured the enthalpies of formation for the two intermetallic phases, Al_3V and Al_8V_5 accurately. The enthalpy and entropy of formation of phases in the Al-V system were reassessed using density functional theory (DFT) and the Calphad method [76]. The partial Gibbs energies of mixing (ΔG_m) of the wt.% Al composition in bcc (V) was estimated by Samkhval et al. [77] through electromotive force (EMF) measurements. The activity of V in the Al-rich liquid was studied by Batalin et al. [78] and the activity of Al between 12 and 76 wt.% for the temperature of 1000 °C was measured by Johnson et al. [79]. They have suggested a solubility limit of Al in V to be > 3 at.% V as determined by Carlson et al. [63].

Thermodynamic data in Table 2-2 gives a summary of the enthalpy and entropy of formation of phases in the Al-V binary system found in the literature.

Table 2-2: Enthalpies and entropies of formation of phases in the Al-V binary system.

Phases	Temperature	ΔH_f [KJ/mol atoms]	ΔS_f [J/mol-atom]	Reference
$Al_{21}V_2$	**298 K**	-8.40	-6.30	DFT [80]
		-10.73	-2.13	Calphad [80]
		-8.30		Calphad [58]
	0 K	-8.91		DFT [81]
$Al_{45}V_7$	**298 K**	-13.94	-9.03	DFT [80]
		- 16.50	-3.40	Calphad [80]
		-12.90		Calphad [58]
	0 K	-14.65		DFT [81]
$Al_{23}V_4$	**298 K**	-15.42	-8.32	DFT [80]
		-18.03	-3.69	Calphad [80]
		-14.20		Calphad [58]
	0 K	-16.04		DFT [81]
Al_3V	**298 K**	-26.91	-10.58	DFT [80]
		-28.11	-4.52	Calphad [80]
		-27.80		Calorimetry [82]
		-27.20		Calorimetry [74]
		-23.90		Calphad [58]
	598 K	- 27.20		Calorimetry [73]
	0 K	-27.32		DFT [81]
		-28.91		DFT [83]
Al_8V_5	**298 K**	-22.93	1.94	Calphad [80]
		-34.00		Calorimetry [82]
		-35.00		Calphad [58]
		-23.40		Calorimetry [74]
	598 K	-22.60		Calorimetry [73]
	706 K	-44.60		EFM [77]

2.3 Microstructures and phases in the Al-V system

The Al-V phase diagrams described in section 2.1 have been reported based on thermal, microscopic, chemical and X-ray evidence. It can be observed that a series of straight lines represent the effect of the elemental composition upon density which also defines the phase boundaries, these phase boundaries correlate with discontinuities in the slope of the straight lines. The possible intermetallic compounds to form in the Al-V system based on the elemental composition were, therefore, determined. Different solid phases include five intermetallics namely the $Al_{21}V_2$, $Al_{45}V_7$, $Al_{23}V_4$, Al_3V, and the Al_8V_5 were determined at ambient temperature with four of the intermediate phases being peritectic.

The properties of phases in the Al-V system are summarized in Table 2-3.

Table 2-3: Phase properties in the Al-V system

Phase	Wt.% V	Crystal Type	Space group	Pearson Symbol	Lattice parameters [Å]
(Al)	0-0.05	Cu	Fm-3m	cF4	a=4.0496
$Al_{21}V_2$	8.7-14.65	Own	Fd-3m	cF184	a=14.496
$Al_{45}V_7$	16.1	Own	C2/m	Mc104	a=2.563 b=7.637 c=11.088 β=12.886
$Al_{23}V_4$	21-24	Own	P63/mmc	hP54	a=7.6928 c=17.04
Al_3V	24-38	Al_3Ti	I4/mmm	tI8	a=3.838 c=8.379
Al_8V_5	> 38	Cu_5Zn_8	I4-3m	cI52	a=9.2345 c=9.243
V	> 51	W	Im-3m	cI2	a=3.0338

Micrographs through microscopic (LOM and SEM) analysis and X-Ray diffraction patterns revealed the phases present in the Al-V system. The procedure for the designation of a phase has been proposed by Willey [84]. The combination of microscopic and X-ray analysis is an excellent technique in phase identification. However, uncertainty in the assigning of the exact composition is observed for samples containing 40-70 wt.% V in the Al-V alloy [85].

Therefore, chemical analysis was employed to determine the elemental composition of the alloy to assign the corresponding phases as determined in Table 2-3. Different micrographs with the assigned wt. % V and the corresponding phases present assigned are presented below.

(a) The fcc (Al) phase

Al dissolves a small amount of V in the solid solution; the maximum solubility has been reported to be 0.2 wt. % (620 °C) [86], 0.37 (630 °C) [87], respectively. Figure 2-4 shows typical microstructures of the fcc- (Al) solid solution phase. Because of the softness of Al and its chemical reactivity, the Al matrix is usually gouged and pitted in a two-phase region. The (Al) phase is isotropic and therefore, it is optically inactive under polarized light. Fewer investigations have been observed on this phase since an extremely high purity of Al is required and only 99.9 % Al is available [88].

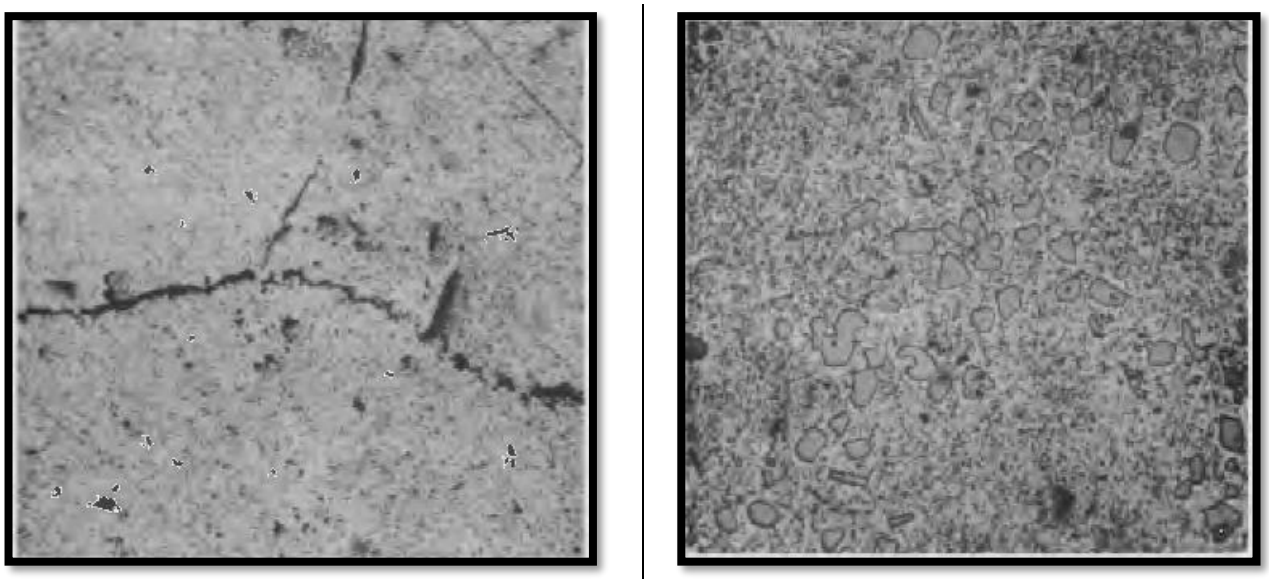

Al-0.4 wt. % V alloy quenched at 625 °C | Al-1.6 wt.% V alloy quenched at 625 °C

Figure 2-4: The (Al) solid solution phase in the Al-V alloy etched with KOH at 250 magnification [88].

(b) The $Al_{21}V_2$

The $Al_{21}V_2$ is the last intermediate phase to be detected in the Al-V system, the phase does not exist at a temperature above 685 °C and cannot be easily distinguished from the Al phase under

the microscope, occasionally found in the as-cast alloy. Figure 2-5 illustrates the typical morphology of the $Al_{21}V_2$ phase.

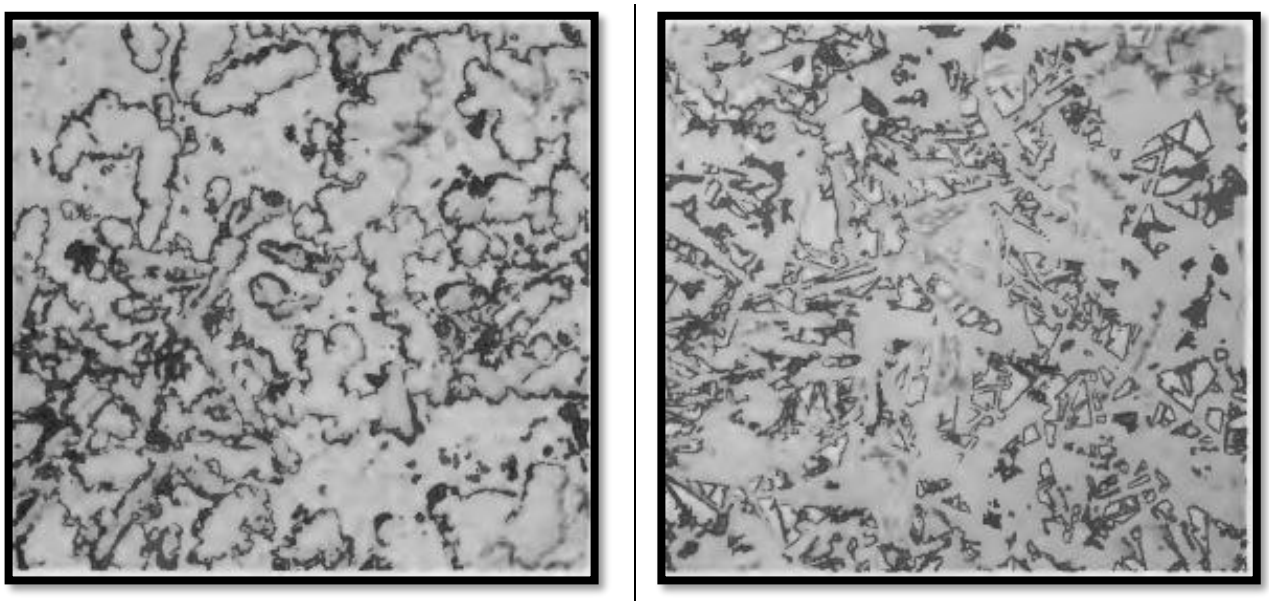

Al-6.3 wt.% V alloy quenched at 625 °C | Al-17 wt.% V alloy quenched at 625 °C

Figure 2-5: The $Al_{21}V_2$ phase in the Al-V alloy etched with KOH at 250 magnification [88].

(c) The $Al_{45}V_7$ and $Al_{23}V_4$

The $Al_{45}V_7$, denoted also as the Al_7V and the $Al_{23}V_4$ phase ranged from between 16-24 wt. % V as shown in Table 2-3. The typical morphology of the phases was obtained in the macrograph of an Al-23.8 wt. % V alloy as shown in Figure 2-6 below. This phase is usually porous since it can only be formed by a diffusion mechanism and not by a casting operation. The phase exists only with temperatures up to 735 °C.

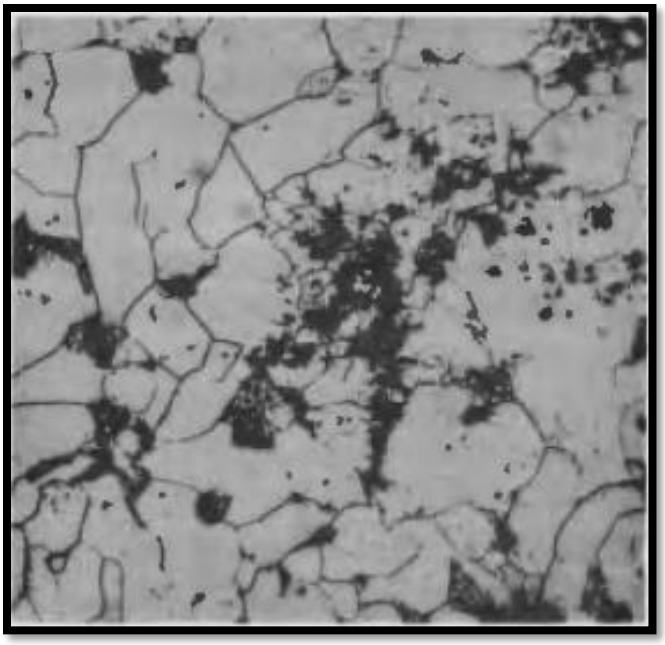

Figure 2-6: The typical morphology of the $Al_{45}V_7$ in Al-23. wt.% V alloy quenched at 710 °C, etched with Kroll reagent at 250 magnification [88].

(d) The Al_3V

The Al_3V phase has been reported by several authors [37], [89], [90]. The phase has a much greater optical activity and can be immediately detected under polarized light unlike the Al phase and the $Al_{45}V_7$. Its peritectic reaction occurs at a temperature of approximately 1360 °C [85]. The Al_3V phase exists in the two-phase region, the lattice parameter depending upon the other phase present, this is a classical illustration of a solubility range in an intermediate phase. Among the intermediate phases, the Al_3V phase has a wide solid solubility range from 27-38 wt. % V for the temperatures up to 1360 °C and decreases with a temperature decrease. The micrographs of the Al-V alloy in Figure 2-7 shows the morphology of the Al_3V phase.

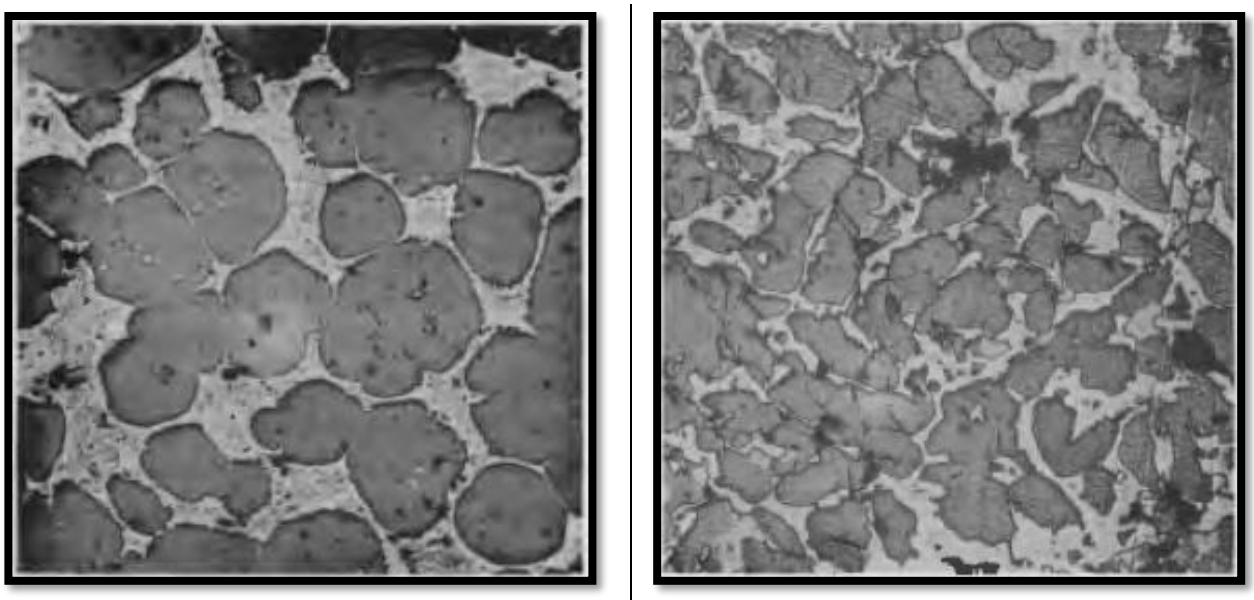

Al-27.2 wt.% V alloy quenched at 750 °C | Al-36.3 wt.% V alloy quenched at 710 °C

Figure 2-7: The Al_3V phase in the Al-V alloy etched with Kroll reagent at 250 magnification. [88]

(e) The Al_8V_5

Figure 2-8 illustrates typical micrographs of the Al_8V_5 phase, this phase shows no optical activity under polarized light and can be easily distinguished with other phases such as Al_3V. The phase is stable up to 1670 °C, its incongruent melting point and has a considerable solid solubility range at 1360 °C [56].

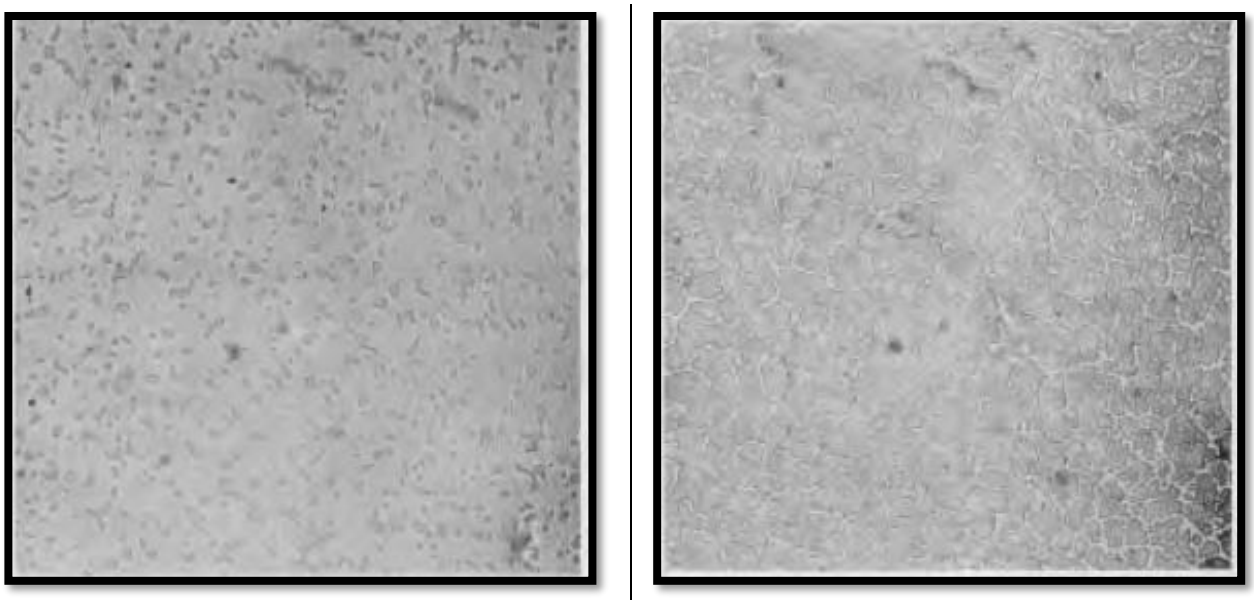

Al-42.7 wt.% V alloy quenched at 900 °C | Al-46 wt.% V alloy quenched at 650 °C

Figure 2-8: The Al_8V_5 phase in the Al-V alloy etched with Kroll reagent, at 250 magnification [88].

(f) The (V) phase

The (V) phase will remain in solid solution up to 25 wt. % Al when furnace cooled from high temperatures. For high vanadium alloys, the microstructure of the alloys is not satisfactory as the favourable etching procedure has not been obtained yet. In the microstructure of these alloys, the presence of small particles at the grain boundaries was observed in the 78.7 per cent V alloys, this was due to the precipitation mechanism occurring in the alloys [63]. From the observation, it was concluded that the limit of solubility of (V) was 78.7 %, then X-ray measurement limits the solubility to 73 wt.% V [85]. Figure 2-9 shows the one (V) phase in the Al-78.7 wt. % V alloy, in which small oxide or nitride impurities are observed at the grain boundaries.

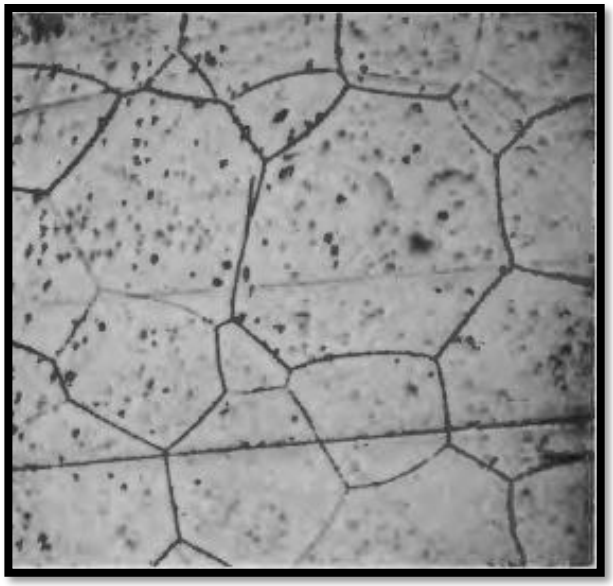

Al-78.7 wt.% V at 75 magnifications

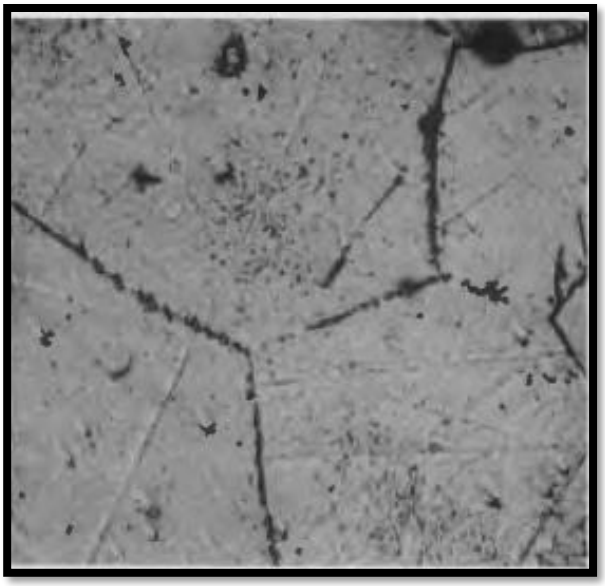

Al-78.7 wt.% V at 250 magnifications

Figure 2-9: The (V) phase observed in the V-rich Al-V alloy quenched at 900 °C at high and low magnification respectively [88].

2.4 Thermodynamic calculations

Thermodynamic calculations are an essential tool for many areas of modelling of phase transformations in materials. Thermodynamic calculations provide a framework for the quantitative description of solubilities and relative stabilities of different minerals and metals [91].

2.4.1 The Thermo-Calc™ software.

The thermodynamic simulation software considered in this study for the calculation of thermodynamic parameters and phase diagram determination of the Al-V system is the "Thermo-Calc™ software and its databases"[92]. Thermo-Calc™ is software designed for the calculation of thermodynamic properties and phase equilibrium of systems. Developed in the 1980s at the Royal Institute of Technology in Stockholm (Sweden), the method has undergone tremendous development and has become a worldwide benchmark in the field of computational engineering sciences. Calculations with the Thermo-Calc™ software require the selection of the database from which thermodynamic properties are obtained. These databases are developed based on the

CALPHAD approach, in which both the thermodynamics and phase equilibrium of systems are described as a function of composition and temperature in a self-consistent framework [93].

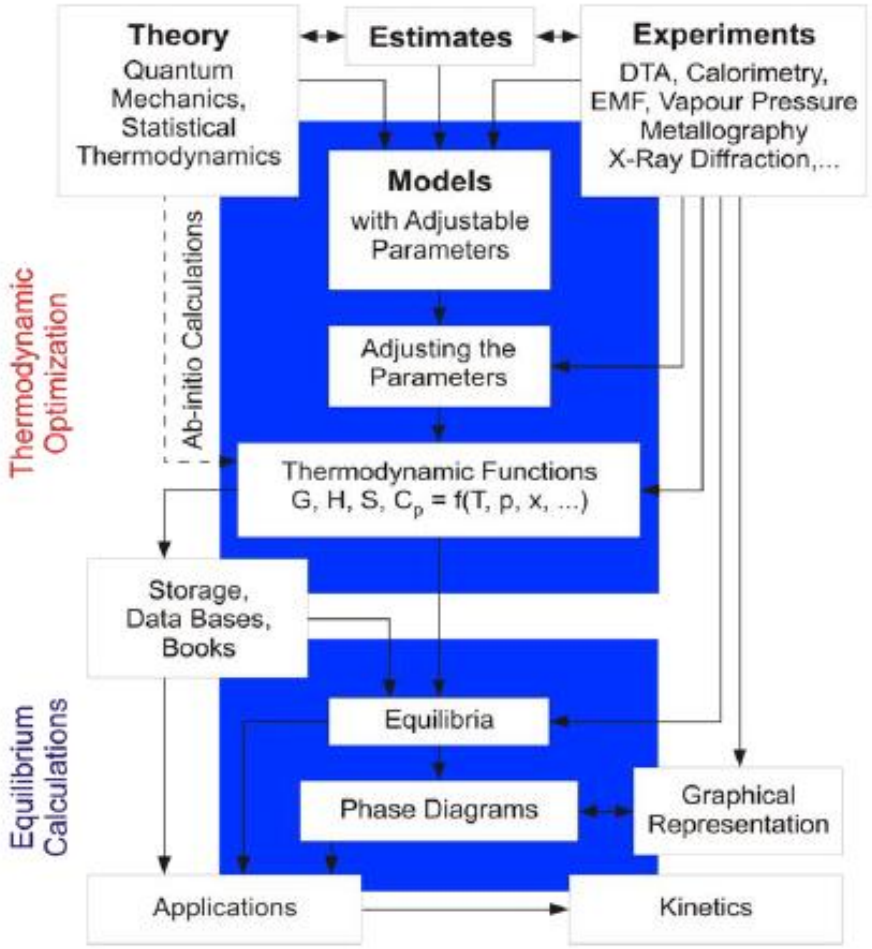

Figure 2-10: Frame-work of the Thermo-Calc™ software program based on the Calphad method [93].

Figure 2-10 presents the framework of Thermo-Calc™ software based on the Calphad method. It is an approach in which thermodynamic parameters of all phases in the systems are described through the determination of the Gibbs free energy, evaluated through critical assessment of the available experimental and theoretical information on phase equilibria and thermodynamic properties of the systems found in the literature.

The computational thermodynamic technique is a useful tool to critically design experiments. The accuracy of the calculations through Thermo-Calc™ software depends on the quality and completeness of the incorporated database [93]. The Calphad method within Thermo-Calc™ is used to construct databases that can predict the phases and property diagrams of systems, especially for cases where sufficient or adequate data is missing for accurate predictions. In this work, phase diagram determination using Thermo-Calc™ software was performed to permit the prediction and understanding of changes in the microstructure and its influence on the subsequent mechanical properties of the material. However, it is important to note that Thermo-Calc™ is used primarily as a guideline since the thermodynamic study of high-temperature systems such as the Al-V alloys has not been completely reported in the literature [62] and the calculations through Thermo-Calc™ are conducted under equilibrium conditions, which are different from reality (non-equilibrium conditions).

2.4.2 The Thermo-Calc™ database and usage.

The most important aspects of a thermodynamic software package are the accurate and validated databases that it contains. Thermodynamic data used in the thermodynamic software is derived from available various experimental results such as phase diagram determinations, calorimetry measurements, EMF measurements and structural determinations. Thermo-Calc™ software uses many critically assessed and high-quality databases from diverse thermodynamic software developer groups such as SGTE, CAMPADA, USTB, Thermo-Tech, etc. These databases incorporate different thermodynamic models for each phase in a certain heterogeneous interaction system. Thermo-Calc™ databases cover a wide range of materials from steels, alloys, melts, glasses, aqueous solutions, organic substances, and polymers to geochemical and environmental systems. Thermo-Calc™ databases are created and maintained in the so-called Thermo-Calc™ database format (TDB), which is considered an international standard for CALPHAD calculations and simulations.

The constant updates, as well as the many improvements, have resulted in the existence of various versions of Thermo-Calc™ software. Thermo-Calc™ is easy to use and does not require any expertise to perform thermodynamic calculations. It can be implemented on different platforms: Windows, Linux, or Mac OS. The latest version is 2020 b, existing in both the console mode and graphical mode. In this work, the limited version 2019 b [94] was used under the Windows

environment in console mode. It was composed of the following modules: Single Point Equilibrium, Scheil Solidification Simulation, Binary Calculator, Ternary Calculator, Property Model Calculator, Diffusion simulation, Precipitation simulation and, Process metallurgy. The BIN and TERN modules were designed to plot phase diagrams and property diagrams. More than 30 thermodynamic and properties databases were available for use in Thermo-Calc^{TM}. The Al-V binary phase diagram and property diagrams were constructed in this work using Thermo-Calc^{TM} 2019b. Databases that were used for the thermodynamic calculations include the TC binary solutions V1.1. and SSOL4: alloy solutions database V4.9g.

2.5 Basic thermal analysis

The most used thermal analyses techniques are differential scanning calorimetry (DSC), differential thermal analysis (DTA), and thermogravimetry analysis (TG) [95]–[98]. In these techniques, both temperature and time dependency are covered and both the thermodynamic and kinetic properties are evaluated, resulting in a large spectrum of possibilities [99]. The non-isothermal temperature program commonly used for which the temperature can be increased or decreased linearly in proportion to time is described by the equation:

$$T = T_0 + C * t \qquad \text{Equation 2-13}$$

where T is the actual temperature, T_0 is the initial temperature, C is the heating/cooling rate and t is the time.

In the DSC equipment, for example, the maximum temperature varies depending on the DSC manufacturers. The increase or decrease in temperature results in microstructure transformation as a consequence of shifting the stage of energy as the energy is released or absorbed. Differential thermal techniques are constructed to analyse how the change in energy is related to properties and affected in each specific case. The general significant properties to be obtained are enthalpy, heat capacity, thermal emissivity, and purity of metals.

2.5.1 Differential scanning calorimetry (DSC)

The DSC technique measures the heat flow of a sample as related to reference material. In the abbreviation of DSC, the term “calorimetry” refers to the technique that involves the heat flow measurement or evaluation of a sample, and the technique that is termed as “differential” is the

one that measures the heat flow of a sample compared to a reference [100]. The output is both time and temperature-dependent. The DSC is a rapid tool that is used to measure properties such as heat capacity, enthalpy and, most importantly, phase transformations [101].

Two types of DSC exist, namely the heat flow DSC and the power compensated DSC [101]. In the former, the crucible samples (test samples) and a reference crucible (reference) are located at specific crucible areas indicated with the symbol “S” and “R” in the DSC chamber (Figure 2-11). A thermocouple junction is situated just underneath the two crucibles (the test and the reference samples) [102] with an optimum contact for optimal heat transfer and precise measurements as illustrated in Figure 2-11. In the heat flow DSC, the heat flow between the sample and the reference is compared to the temperature changes according to the temperature program imposed [103].

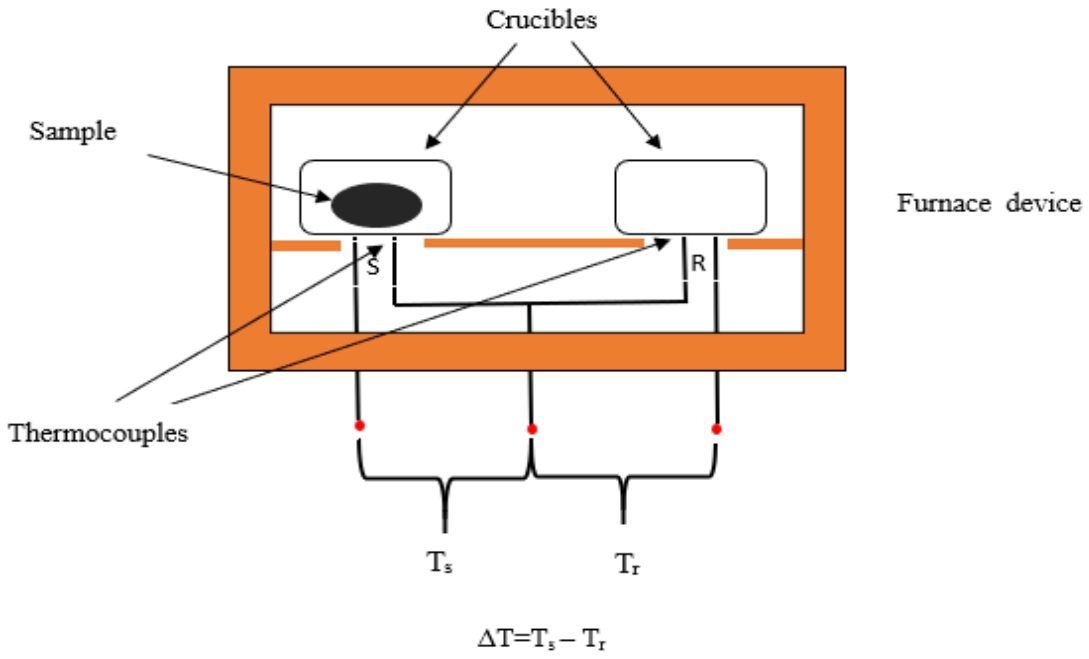

Figure 2-11: Schematic diagram of heat flux differential scanning calorimetry (DSC)

The thermocouples are the most useful instruments to measure the temperature both in the DSC and DTA equipment and are placed just underneath the test and reference samples respectively [103] and electrically connected as shown in Figure 2-11.

However, in the compensated DSC both the sample and the reference are kept at the same temperature throughout the complete temperature program. A slight deviation in heat flow from either the sample or the reference will result in power adjustment by proceeding with the balance between the two. This adjustment corresponds to an endothermic or exothermic reaction which is shown on the DSC trace as illustrated in Figure 2-12.

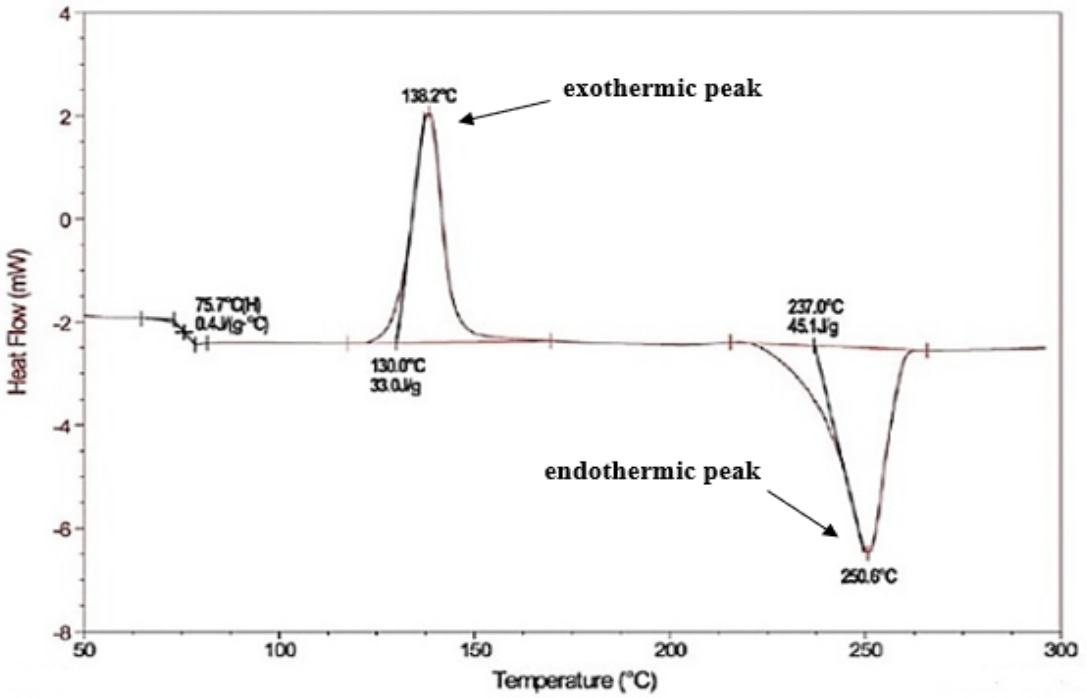

Figure 2-12: DSC plot for polyethylene terephthalate (PET) showing both the exothermic and endothermic reactions occurring during a temperature scan from 50 -300 °C [104].

Due to the temperature difference between the two samples, an electron loop is created. Given the sample and the reference of different heat conductivity, it is implied that with any increase in temperature, a different amount of heat will be conducted to the respective thermocouple junction. Therefore, a temperature potential will be generated proportional to the heat flow in the DSC. In the function of thermocouple, an instant temperature difference creates a current due to free electron density. According to Le Chatelier's principle [105], the energy is either absorbed or released from the system and the phase transformation rather than temperature change is recorded. Therefore, first-order transitions occur isothermally. This explains why sharp peaks are observed

in the melting and solidification process. However, ideal conditions would result in a straight vertical line in the DSC curves. This is not the case due to kinetic reasons. Electric resistance is used to heat the DSC furnaces, a technique based on electronic movement in electrically resistant materials which result in energy dissipation. The heat generated by frequent collisions in the lattice and the energy that is created is proportional to the current and the material resistance. Since increasing temperature increases the electric resistance, additional power must be generated to increase the temperature.

2.5.2 Simultaneous thermal analysis (STA)

STA, an acronym for "simultaneous thermal analysis", is a standard term used to indicate a simultaneous application of different types of techniques and most generally refers to the concurrent application of the DSC and TG [98]. The technique allows for the obtaining of a real-time measurement and analysis of the sample through the manipulation of one single instrument. Less time is required to perform the simultaneous measurements and properties recorded on one device than measuring and recording these properties on separate devices. In the STA, the test conditions are perfectly identical for the DSC and TG signals (same atmosphere, same gas flow rate, heating rate, thermal contact of the sample crucible and sensor, etc.). An accurate correlation of the different observed events is guaranteed. The total amount of information that one can obtain about the sample in the STA is greater than the summation of individual information obtained from the separate instruments. Equipped with innovative sensor technology and compact furnace design, STA's are suitable techniques to be implemented because of their possibilities of resulting measurements.

2.6 Manufacture technologies of high-temperature materials.

In the manufacturing of high-temperature resistant materials, which include ceramics, metals, alloys, and composites, two basic technologies such as melting and casting, and powder metallurgy (PM) methods are used. Therefore, high-temperature resistant alloys such as Ti-6Al-4V alloy, and its sub-system, the Al-V alloys can be produced through these methods. All these methods have their pros and cons.

2.6.1 Melting and casting technology

In metals processing, the melting, casting, and solidification processes are used to produce semi-finished products. The molten metals and alloys are cast by continuous methods or into individual ingot moulds. Subsequently, these castings are rolled or forged into semi-finished shapes (sheet, plate, rod, bars, etc..) [106]. The melting method is widely used in industries to produce alloys [107]. The method uses two types of crucibles namely, hot crucibles and cold crucibles. The combination of furnaces, alloys, working practices, metallurgical treatments, pouring arrangements and end products are not likely to be duplicated at any facility. The choice of the optimal crucible to provide maximum performance is an individualised and complex task based on the relationship between the metal melting/holding operations and specific crucible characteristics. Crucibles are used in fuel-fired furnaces, in electric resistance furnaces, in induction furnaces etc. The type of metals and alloys to melt or hold decide the characteristics of the optimal crucible selection. In melting of copper-based alloys, roller formed silicon carbide crucibles are used; carbon-bonded and ceramic-bonded clay graphite and silicon carbide crucibles are used in melting and holding of Al, Al alloys, Al-bronze, etc. [108].

Conventional alloy melting processes are typically used to produce ingots and casting. The most common ingot casting methods are vacuum-arc remelting (VAR), induction-skull melting (ISM) and plasma arc melting (PAM). In Al-V metal alloys, the melting and casting processing which has important advantages in terms of high purity alloys presents technical problems due to the high melting point of V [109] against the low melting point of Al and the potential of high-temperature reaction between the melt and the crucible. Crucible compatibility with metal alloys in the cold crucible (arc melting) is good enough to produce high purity alloys, however, no near-net-shape manufacturing is possible. For the hot crucible melting (induction melting), the reaction between the crucible and the metal leads to low alloy purity. However, near-net-shape manufacturing is possible with some alloys.

In the manufacture of some alloys such as Ti alloys or Ti-Al based intermetallic alloys via conventional methods (casting, forging, sheet forming, extrusion, etc) [110],[111], the low susceptibility to plastic deformation and the high tendency for brittle cracking of the produced intermetallic alloys have made very challenging the use of these conventional methods to produce near-net-shape components [112]. Another strong contender of alloy melting processes is an

additive manufacturing (AM) using electron beam (EBM) melting and casting technology [113]. The EBM technology produces ingots and casting by melting powders of materials in furnaces using an electron beam, which acts similar to a laser beam [114]. Therefore, EBM parts manufacturing necessitates finer metal powders as feedstock [115]. Commercially available materials produced by EBM technology are pre-alloyed metal powder of commercially pure (CP) Ti, and Ti- alloys (such as Ti-6Al-4V, Ti-6Al-4V-ELI, and Ti-Al based alloys) [116], Co-Cr-Mo, and Inconel 718 [117]. Others reported EBM-manufactured materials are stainless steel 316L [118] and high entropy alloys [119]. As compared to conventional manufacturing techniques such as machining, casting, and welding, the EBM technique significantly reduces the time, cost and challenges of machining or investment casting are disregarded [120]. In the principle of AM using powder bed fusion (PBF) in metal, the powder is distributed over a thin layer and then melted using a laser or an electron bean according to a computer-assisted design (CAD) model. A laser beam can propagate in an air or gas atmosphere, while electrons require a vacuum to propagate [114]. Moreover, in principle EBM components are near-net shape, like those made via casting processes. However, the surface roughness required some light secondary machining or grinding operations to refine the surface.

2.6.2 The possible manufacturing processes of the Al-V alloys in industry.

Various methods are used to produce Al-based master alloys. The mixing processes, the most basic one is that in which the molten Al and other elements are simply mixed. For example, with the addition of elements such as Mn, Ti, and Si to molten Al, the production of Al-Mn, Al-Ti, and Al-Si master alloys are possible [31], [38], [39]. Other methods for the production of the Al-based master alloys are sintering and mechanical alloying [34]. However, the high cost of the alloying elements and material loss during the alloying process are the main disadvantages of these processes [35].

Al-based alloys such as the Al-V master alloys have attracted the attention of researchers [121]–[123], with the 60Al-40V master alloy being in considerable demand to produce the Ti-6Al-4V alloy. The aluminothermic reaction is a process for reducing metal oxides using Al powder [54], [55]. During the reaction, the mixture of Al and oxides is ignited, causing the Al to be oxidised and the metal oxide to be reduced to the metal [42] resulting in the formation of the alloy metal. Al and vanadium pentoxide (V_2O_5) are used as starting materials in the production of the Al-V

alloys. In the aluminothermic reaction process, V_2O_5 and Al metal need to be mixed in such proportion (with the Al: V_2O_5 mass ratios 0.8:1 to 1:1) [124], [125], to produce an exothermic reaction capable of generating the master alloy [44]. However, the reaction rate is too fast and consequently, the control of the quality of the product becomes laborious. Furthermore, the amount of Al required to produce Al-V and Al_2O_3 slag is higher than the stoichiometric amount of Al to avoid the contamination of Al-V master alloy [124].

CHAPTER 3. RESEARCH METHODOLOGY

Thermodynamic calculations and experimental procedures for the development and production of the Al-V master alloy are provided in this chapter. Thermo-Calc^{TM} predictions were performed considering the master alloy to be produced which must contain 60 wt. % Al and 40 wt. % V, respectively. The Thermo-Calc^{TM} software was used to predict the phase equilibria and thermodynamic properties of the Al-V alloy system. The basic experimental procedures that were used in this study for the characterisation of the targeted 60Al-40V master alloy are also described. The aluminothermic reaction process, the material's composition, equipment, and experimental procedure used for the investigation of the produced master alloy are also provided. The samples were prepared for microstructural analysis and characterised using techniques such as light optical microscopy (LOM), scanning electron microscopy (SEM), scanning electron X-ray spectroscopy (EDX), and X-Ray diffraction (XRD). The thermal analysis was conducted using the differential scanning calorimetry and thermogravimetry (DSC-TG) technique. Microhardness testing was performed to determine the hardness of the material.

3.1 Thermodynamic calculations

The thermodynamic calculations were done to predict the Al-V phase diagram and thermodynamic parameters such as Gibbs free energy, enthalpy/ entropy, and activities of the constituents in the Al-V binary system. The equilibrium phase diagram of the Al-V binary system and the expected stable phases, as well as property diagrams of the Al-V binary system, were determined in this work using Thermo-Calc^{TM}, version 2019b. The phase diagram with the intermetallic phases formed and the property diagrams of the Al-V binary system were predicted using TC binary solutions V1.1 and SSOL4: alloys solutions database V4.9g, respectively. The predicted phases were calculated based on the 60 wt.% Al and 40 wt.% V, in the temperature range up to 2000 °C (2273 K). The activities of the constitutive V and Al elements as a function of Al/V concentration were calculated in the temperature range between 373 and 2273 K.

3.2 Raw materials and master alloy preparation (using the aluminothermic process)

The aluminothermic process was used to produce the master alloy. A bottom melt alloy was produced for the microstructural, chemical and phase composition analysis's interest. The starting

materials used in the process were pure Al metal (99 % purity), vanadium pentoxide (V_2O_5) and fluxes. In the production of the pre-alloyed 60Al-40V, an exothermic mixture consisting of V_2O_5, Al metal (99 % purity) and fluxes was melted in a water-cooled copper vessel. This type of vessel is found to be widely used for the production of high purity master alloys by the thermal process [126]. It is well known that water cooling affects the quality of the product by controlling the rate of heat transfer, thermal gradients and resulting thermal stresses [127].

Commercially produced vanadium pentoxide (V_2O_5) particles with a diameter of 7-20 mm and 99 % purity aluminium (Al) with particles sizes of diameter 1-3 mm and CaO powder ($\leq$ 50 μm), as by suppliers, were used in the current study. Pure Al metal (99 % purity) and V_2O_5 were mixed in a ratio of 1:2 (Al: V_2O_5) and then placed in a crucible. The CaO as an additive was used to flux the alumina forming during the reduction of vanadium oxide. High purity electrodes were used to ignite the mixture in the furnace. The measured furnace temperature reached 1900 °C due to the exothermic nature of the reaction which made the melting of the starting elements to form the Al-V alloy. The electrode voltage was ensured to be at 1.1kV while the material was continuously charged in the furnace. On completion of the reduction, the furnace was allowed to cool for 72 hours. The slag was observed to be separated from the alloy on cooling. The overall reactions in the aluminothermic process can be represented by the following equations:

$$\text{Flux} + 3\,V_2O_5 + 10\,Al \rightarrow 6\,V(\text{metal}) + 5\,Al_2O_3 + \text{heat} \qquad \text{Equation 3-1}$$

$$V\,(\text{metal}) + 3\,Al\,(\text{molten}) \rightarrow Al_3V \qquad \text{Equation 3-2}$$

3.3 Characterisation of the produced 60Al-40V master alloy

3.3.1 Chemical analysis

The 60Al-40V master alloy samples produced by the aluminothermic process were analysed using inductively coupled plasma mass spectrometry (ICP). This technique allows the determination of the level of elemental contamination in metals and alloys. In this report, the Leco TCH 600 inert gas fusion technique was used on the pre-master alloys to determine the level of oxygen content in the produced master alloys according to ASTM standard [128] because cast alloys are subjected to elemental contamination such as oxygen, nitrogen and hydrogen.

3.3.2 Microstructural and phase analysis

Samples of the aluminothermically produced master alloy were sectioned using high-quality carbide cutting blades. The sectioned samples were hot mounted using Polyfast (black Bakelite hot mounting resin with carbon filler) and mechanically grounded and polished to 0.25 µm diamond finish up to colloidal silica (OP-S) suspension until all mechanical scratches were removed. The samples were etched using "Kroll's reagent" made up of distilled water, hydrofluoric acid, and nitric acid. The polished specimens were chemically etched for approximately 1-2 minutes in the Kroll's reagent.

The light optical microscopy (LOM) and scanning electron microscopy (SEM) were used to study the morphology and phases of the master alloy. The computer-interfaced Olympus optical microscope and a JEOL scanning electron microscope were also used in this study.

The X-Ray diffraction (XRD) analysis was carried out using the Bruker X-ray diffractometer equipped with the detector and Cu Kα radiation. The sample was pulverised to a homogenous powder before XRD analysis according to the standardised PANalytical backloading system, which provides an almost random distribution of the particles. The sample was analysed using a PANalytical X'Pert Pro powder diffractometer in 2-θ configuration with an X'Celerator detector and variable divergence-and fixed receiving slits with Fe filtered Co-K_α radiation (λ= 1.789 Å). The crystal structure was determined by selecting the best-fitting patterns according to the standard X-ray diffraction powder patterns (ICCD database) [129], [130] to the measured diffraction using X'Pert High Score Plus software. The relative phase amounts and, the weight percentage of the crystalline portion were estimated using the Rietveld method using the same X'Pert High Score Plus software. The XRD and EDX were used to study the crystal structure and composition of the samples. In this work, the same SEM was used to perform energy-dispersive x-ray spectroscopy (EDX) on the as-cast samples. The EDX point analysis and mapping were carried out to analyse the chemical composition of the samples.

3.3.3 Thermal analysis

To investigate the phase transition temperatures of the master alloy, thermal analysis was performed using the TA Instruments SDT Q600 Thermogravimetric analyzer (TG) and differential

scanning calorimeter (DSC) in a Nitrogen-controlled environment at NECSA where two sets of experiments were successively performed namely,

- double heating from room temperature to 1100 ^{o}C at 20 ^{o}C /min and,
- double heating from room temperature to 1300 ^{o}C at 20 ^{o}C /min.

The NETZCH 404 DSC thermal analysis was performed by heating the master alloy from room temperature up to 1400 °C at the rate of 20 °C/ min in an argon-controlled environment.

Three sets of experiments in total were performed. The masses of the specimen used for DSC-TG analysis were successively 11.48, 11.06, and 55.70 mg. The high purity Al_2O_3 pan was used as reference material. The samples were heated from room temperature to 1100, 1300 (at NECSA) and 1400 °C (at CSIR) at 20 °C /min and, cooled down to room temperature. The heating and cooling cycles were repeated once.

3.3.4 Microhardness testing

One of the most used methods to measure the hardness of materials in very localised areas i.e., different microstructural phases, is the Vickers micro-hardness test method, which was performed in this study. The Vickers hardness test with a specifically applied load (P) of 50 g was performed on the samples, with a dwell time of 15 s and different indentations were made. The Micro Met Scientific cc digital microhardness tester was used to measure the hardness values of the samples according to the ASTM E-384 [131].

CHAPTER 4. RESULTS

This chapter presents the thermodynamics, material characterisation, and thermal analysis results of the as-cast Al-V master alloy produced by the aluminothermic reaction process. The equilibrium phase diagram and expected stable phases, as well as property diagrams of the Al-V binary system, were determined in this work using Thermo-Calc^{TM} software. Samples of the produced 60Al-40V master alloy were prepared and characterised through LOM, SEM, EDX, and X-Ray diffraction (XRD) analysis. The thermal analysis of the material was conducted through the simultaneous DSC-TG technique. The hardness values of the samples were measured through microhardness testing. The phase transformation predictions, microstructural characterization and hardness measurement results are presented in sections 4.1, 4.2, and 4.3, respectively.

4.1 Phase transformation predictions using Thermo-Calc^{TM} software.

4.1.1 Phase diagram

The phase diagram of the Al-V binary system and the expected intermetallic phases are given in Figure 4-1. The predicted reactions and their invariant temperatures are summarized in equations 4-1 to 4-6.

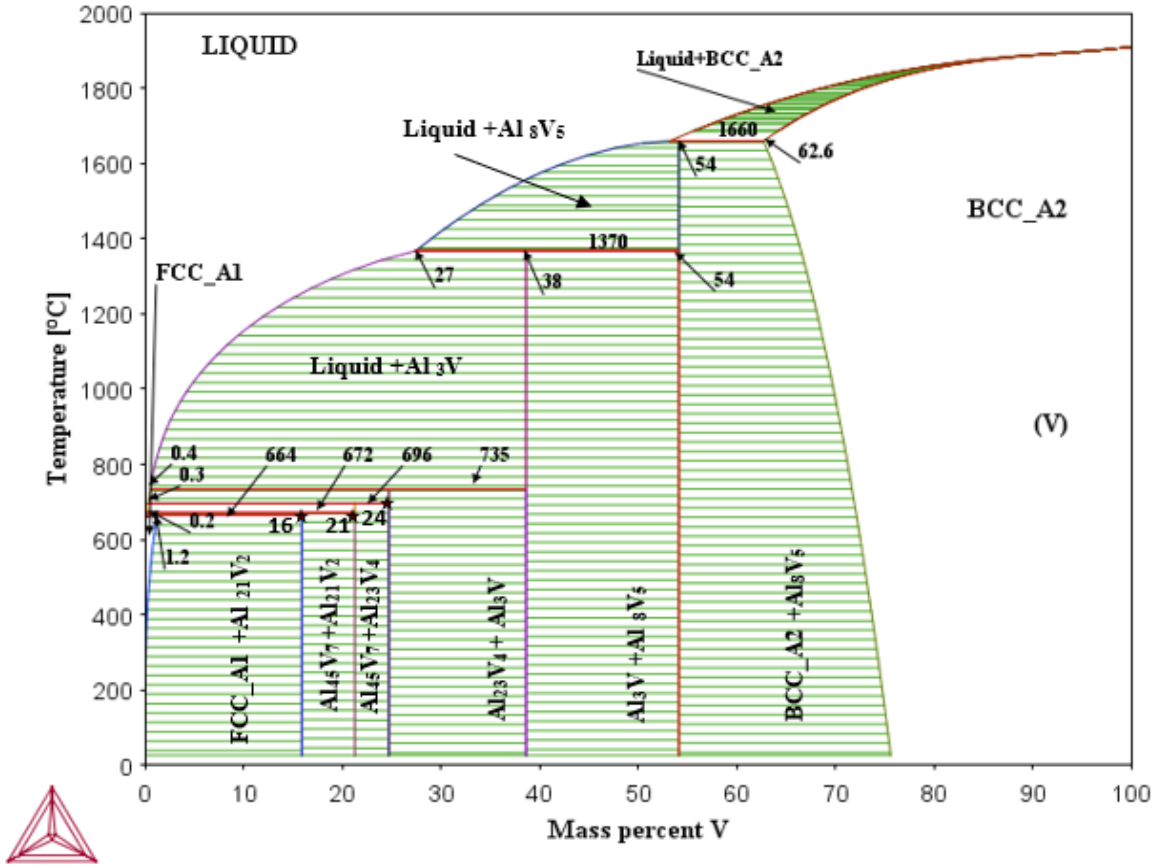

Figure 4-1: The Thermo-Calc™ predicted Al-V phase diagram.

664 °C: $L + Al_{21}V_2 \rightarrow Al\_fcc$ Equation 4-1

672 °C: $L + Al_{45}V_7 \rightarrow Al_{21}V_2$ Equation 4-2

696 °C: $L + Al_{23}V_4 \rightarrow Al_{45}V_7$ Equation 4-3

735 °C: $L + Al_3V \rightarrow Al_{23}V_4$ Equation 4-4

1370 °C: $L + Al_8V_5 \rightarrow Al_3V$ Equation 4-5

1660 °C: $L + V\_bcc \rightarrow Al_8V_5$ Equation 4-6

The summary of the structural information in the Al-V phase diagram is given in Table 4-1.

Table 4-1: Structural information in the Al-V phase diagram using Thermo-Calc™. (This work)

Phase names	Other names	Weight range (%)	Structure	Space group	Pearson symbol	Model
liquid						(Al, V)
(Al)	fcc	0-0.05V	A1	Fm-3m	cF4	(Al, V)
$Al_{21}V_2$	$Al_{10}V$	8.7-15.9		Fd-3m	cF184	$(Al)_{10}(V)_1$
$Al_{45}V_7$	Al_7V	16 V		C2/m	Mc104	$(Al)_7(V)_1$
$Al_{23}V_4$		21-24V		P63/mm	hP54	$(Al)_{23}(V)_4$
Al_3V		27-38V	D022	I4/mmm	tl8	$(Al)_3(V)_1$
Al_8V_5		38V-54V	D82	I4-3m	cl2	$(Al)_8(V)_5$
(V)	bcc	62.6-100V	A2	Im-3m	cl2	(Al, V)

Table 4-2. presents a comparison of the phases and the invariant temperatures found in this current work by DSC-TG and as predicted by Thermo-Calc™ versus available data in the literature. As maybe seen in Table 4-2, there is a good agreement between what was found and what was predicted in this work and in the literature.

Table 4-2: Peritectic melting temperatures of compounds in the Al-V system

Phase	fcc	$Al_{21}V_2$	$Al_{45}V_7$	$Al_{23}V_4$	Al_3V	Al_8V_5	Process	Ref
Melting T (°C)	660	685		735	1360	1670	Optical pyrometry	[63], [132]
	660	688		736	1362	1673		[37]
	661.8						XRD	[133]
	661.8	670					XRD	[134]
		727		>850				[135]
	665	690	730	736	1270	1408	Calorimetry	[57]
						1405		[65]
	660	672	696	735	1334	1539		[136]
Melting T (°C)	664	672	696	735	1370	1660	Thermo-Calc™.	This work
	656/661	-	-	728	1272	-	DSC-TG	This work

Figure 4-2 presents the variation of the volume fraction of phases as a function of temperature. The phases of interest in the Al-V binary system for high-temperature applications are the intermetallic phases namely the Al_3V and Al_8V_5, respectively.

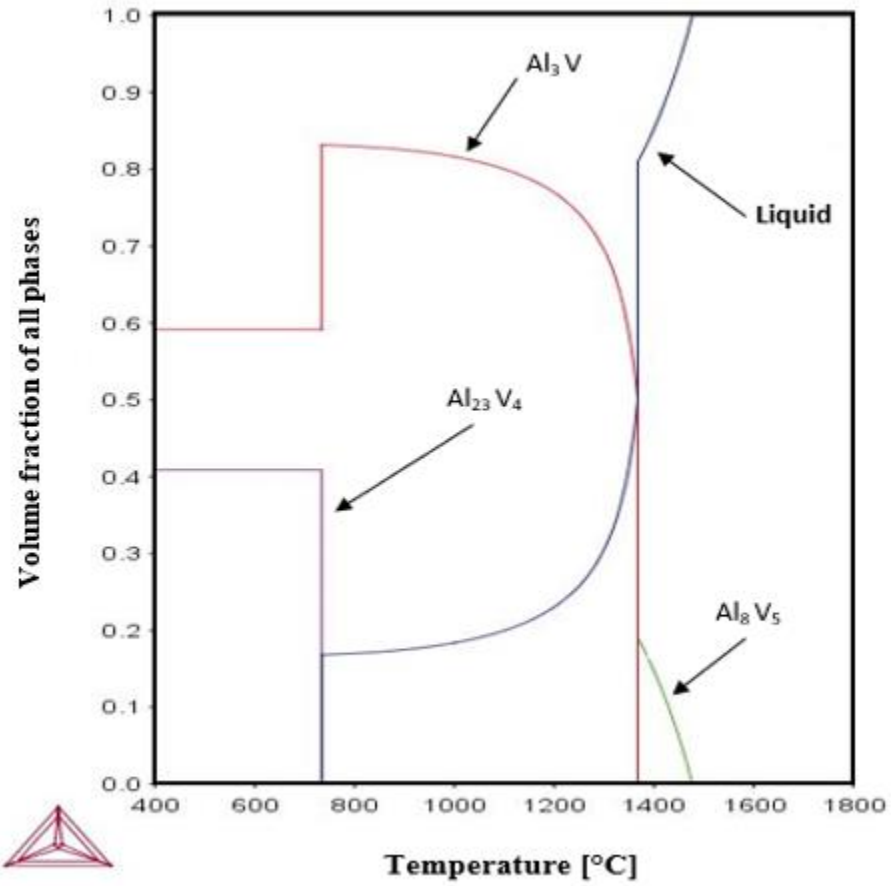

Figure 4-2: The volume fraction of all phases in the Al-V binary system as a function of temperature.

4.1.2 Thermodynamic properties

Through the same Thermo-Calc^{TM} software, thermodynamic parameters of the Al-V binary system such as the Gibbs free energy of mixing, enthalpy of mixing and activities of the components in the system were determined.

4.1.2.1 Gibbs free energy of mixing

The calculated Gibbs free energies of mixing of the system are given in Figure 4-3. The negative and lower Gibbs free energy values as a function of the V content are an indication of the more stable phases. As observed the more negative Gibbs free energy which indicates the most stable phase in the system is that of the Al_3V intermetallic phase.

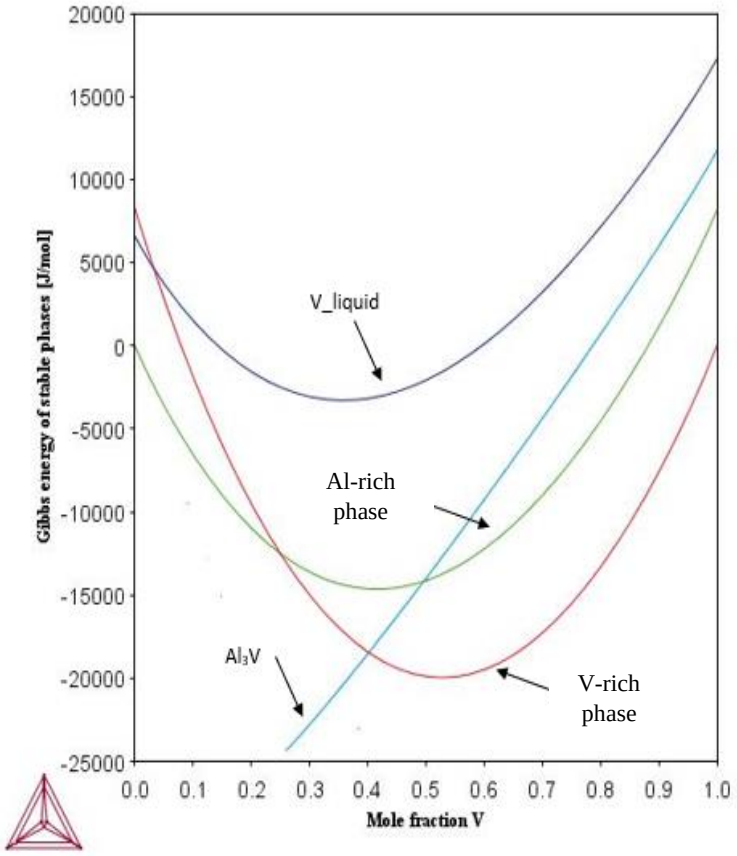

Figure 4-3: The variation of the calculated Gibbs free energy (phase stability) of the phases as a function of the mole fraction of V.

4.1.2.2 Enthalpy of mixing

Figure 4-4 shows the calculated enthalpy of mixing of the Al-V binary system. Negative values were observed for the Al_3V intermetallic phase above 0.2 moles of vanadium indicating that the Al_3V is the product of an endothermic reaction.

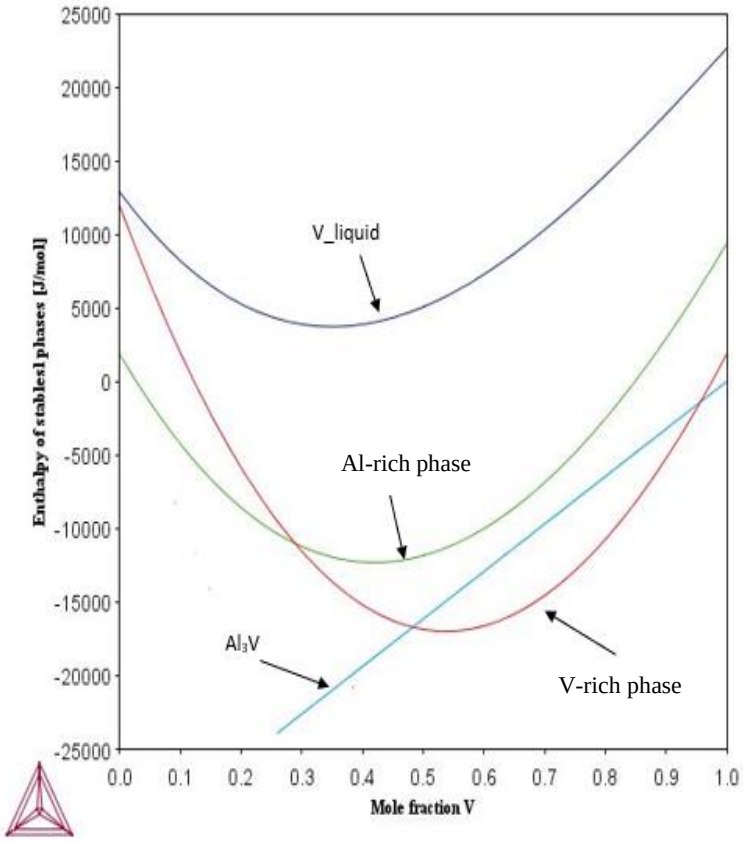

Figure 4-4: The change in the calculated enthalpy of formation of the Al-V binary system as a function of the mole fraction of V.

4.1.2.3 Activities of the components in the Al-V binary system

The activity of vanadium and aluminium in the Al-V binary system is calculated in this work using Thermo-Calc^{TM} thermochemical software and databases [92]. The activity of V and Al as a function of Al/V concentration is calculated in the temperature range between 373 and 2273 K. To assess the stability of compounds in the Al-V binary system, the activities of V and Al as a function of temperature need to be determined, and the resulting equation used to express the activity-temperature relationship is given by:

$$\ln a_i = A + B/T \qquad \text{Equation 4-7}$$

where A and B are coefficients to be determined.

The activity (a_i) relationship based on the composition (X_i) is also expressed as:

$$\ln a_i = A + B X_i + CX_i + DX_i \qquad \text{Equation 4-8}$$

where T = constant; i = Al, V

The activity-composition diagrams of V and Al compounds in the Al-V binary system at a temperature of 2273 K done in Thermo-Calc^{TM} software are shown in Figure 4-5.

Figure 4-5 presents the activity of V/Al components in the Al-V binary system as a function of mole fraction of Al and V, respectively. The activities of both constitutive elements in the Al-V binary system showed a strong negative deviation from the ideal behaviour. Therefore, a good mixing ability between the corresponding compounds was observed. It was also observed that the activity values of V increase proportionally with an increase in the V content while the activity values of Al decrease with the increase in the V content. Inversely the activity values of V decrease while the activity values of Al increase with the increase of Al content.

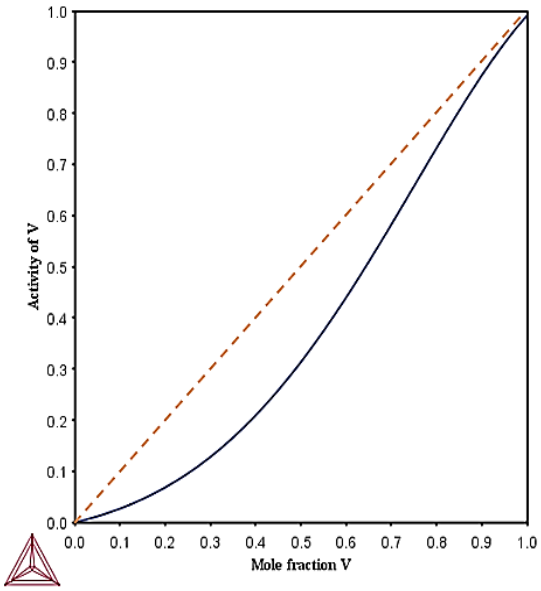

(a).

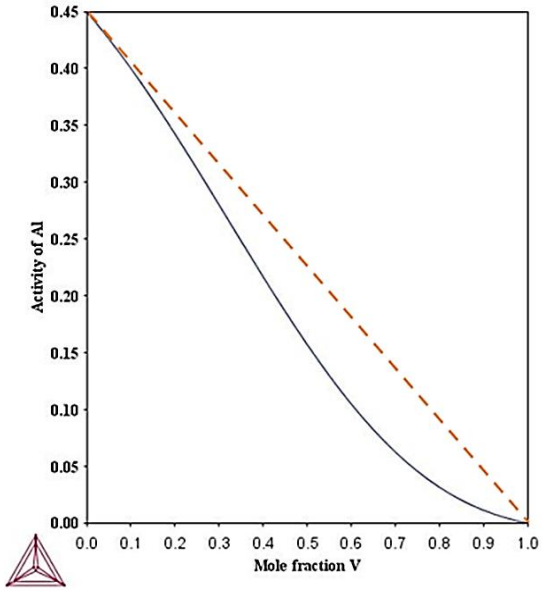

(b).

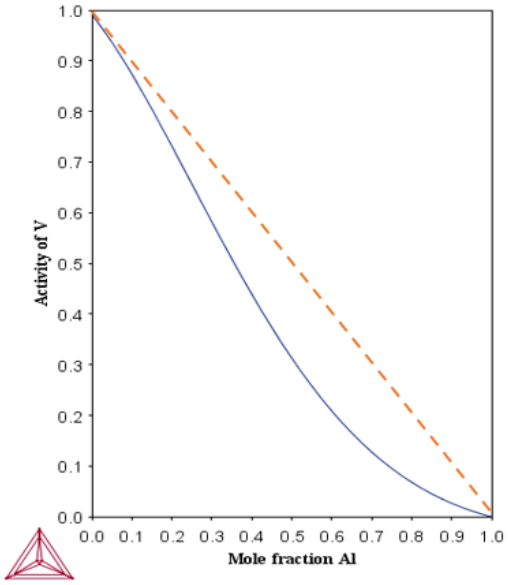

(c).

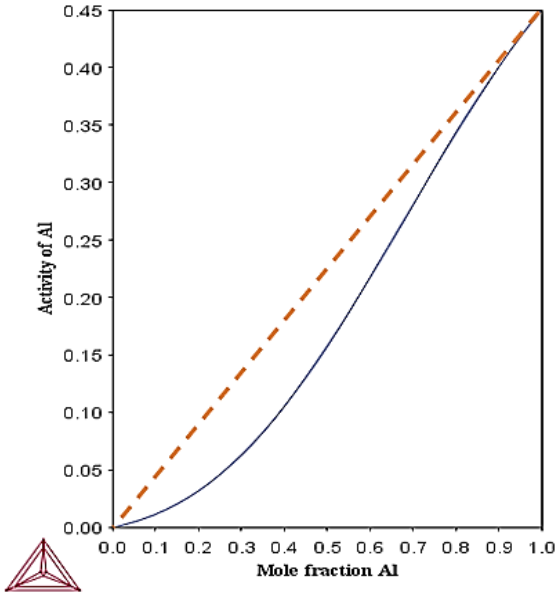

(d).

Figure 4-5: The activity of (a), (c) the V element and (b), (d) of the Al element, in the Al-V binary system as a function of mole fraction of V and Al, respectively.

4.1.3 Expected intermetallic phases in the Al-V alloy as a function of composition.

The predicted Al-V phase diagram (Figure 4-1) and thermodynamic property diagrams (Figure 4-2 to Figure 4-4) calculated by Thermo-Calc^{TM} predictions software can be used to determine the expected intermetallic alloys to use for high-temperature applications. Therefore, intermetallic phases have attracted the attention of many researchers such as the Al_3V and Al_8V_5 phases due to their mechanical properties which are required, are to be found in the alloys. Considering the Thermo-Calc^{TM} predicted Al-V phase diagram in Figure 4-1, it can be observed that the expected phases to be formed in the theoretical 60Al-40V master alloys are the Al_8V_5 and Al_3V intermetallic phases, with Al_3V the most stable phase as this phase exists over a wide range of composition (27-38 wt. % V) and temperature (800-1360 °C) as shown in Figure 4-2. The thermodynamic property diagrams in Figure 4-3 and Figure 4-4 also indicate that the most stable phase to form is the Al_3V intermetallic phase in the interval of 0.27- 0.4 and 0.27-0.48 mole fraction V respectively. Based on the elemental composition of the theoretical master alloy which contains 60 wt.% and 40 wt.% of Al and V respectively as well as the actual composition of the aluminothermic produced master alloy, which contained 63 wt.% Al and 37 wt.% V, the presence of the Al_3V intermetallic as a stable phase is expected in the produced master alloy.

4.2 Characterisation of the aluminothermy produced 60Al-40V master alloy.

4.2.1 Chemical composition

The chemical composition of the aluminothermically produced 60Al-40V master alloy must comply with the specifications. Table 4-3 and Table 4-4 give the chemical composition according to the AMETEK standard specifications of the commercial 60Al-40V master alloy [137] and the elemental chemical composition analysis by ICP of the aluminothermically produced 60Al-40V master alloy, respectively.

Table 4-3: The chemical composition AMETEK standard specification of the 60Al-40V master alloy [137].

Elements %	Symbol	Wt. [%]
Aluminium	**Al**	54-60 %
Vanadium	**V**	40-45 %
Nickel	**Ni**	0.05 % Max
Boron	**B**	0.003 % Max
Carbon	**C**	0.10 % Max
Chromium	**Cr**	0.20 % Max

Copper	**Cu**	0.10 % Max
Iron	**Fe**	0.50 % Max
Magnesium	**Mn**	0.05 % Max
Manganese	**Mg**	0.05 % Max
Molybdenum	**Mo**	0.30 % Max
Phosphorous	**P**	0.02 % Max
Silicon	**Si**	0.50 % Max
Sulfur	**S**	0.03 % Max
Tungsten	**W**	0.05 % Max
Hydrogen	**H**	0.015 % Max
Nitrogen	**N**	0.05 % Max
Oxygen	**O**	0.10% Max

Table 4-4: Elemental chemical composition analysis by ICP of the produced 60Al-40V master alloy (this work)

Composition in wt. %													
Elements	**Al**	**V**	**Si**	**Fe**	**Cu**	**Mn**	**Mg**	**Cr**	**Ni**	**Zn**	**Ti**	**Sn**	**Pb**
Sample 1	62.9	36.1	0.31	0.17	0.02	≤0.01	≤0.01	≤0.01	≤0.01	0.008	0.054	0.013	0.072
Sample 2	64.9	33.2	0.087	0.23	0.14	≤0.01	≤0.01	≤0.01	≤0.01	0.018	0.047	0.014	0.069

Samples of the pre-master alloy produced by the aluminothermic reaction process were analysed in their as-cast conditions by ICP (inductively coupled plasma mass spectrometry) analysis. As may be seen in Table 4-4, the average compositions of the Al and V element content of the samples were found to be between 62.9 and 64.9 wt. % for the Al, and 36.1 and 33.2 wt. % for the V.

The oxygen contamination is a major concern during the processing of these alloys, and thus, an analysis of the oxygen content was performed prior to commencing the experiments to determine the maximum and minimum oxygen content in the as-received master alloys using the gas fusion technique [138]. The oxygen content analysis using the Leco TECH 600 technique was performed and the results are shown in Table 4-5.

Table 4-5. Oxygen content in the 60Al-40V master alloy analyzed using Leco TECH 600, the values are an average of three counts.

Name	Description	Method	Mass	H [ppm]	O [%]	N [%]
60Al-40V	Sample 1	SCAW	0.2861	258	0.222	0.00173
	Sample 2		0.2567	73.8	0.107	0.00011
	Sample 3		0.1078	34.3	0.189	0.00015
	Average		0.2169	44.6	0.172	0.00066

From the results of the Leco TECH analysis, the average oxygen content in the master alloy was found to be 0.172%, which is within the allowable limit of < 0.2% oxygen content in commercial Ti-alloys as required in the ASTM E-1409 standard specifications [139]. But this oxygen content can be considered very high in the production of Ti-6Al-4V ELI (Grade 23) with a maximum oxygen content of 0.13 % [140]. The oxygen content in the final product of Ti alloys is relatively dependent on the application as the oxygen influences their mechanical properties, i.e., the yield strength increases with an increase in the oxygen content, while the ductility inversely decreases. Therefore, the amount of oxygen in the final product of Ti alloys needs to be quantified and controlled. In the Leco TECH analysis, the hydrogen (H) content varied significantly in one of the investigated samples (Table 4-5). The levels of H content in Al and its alloys are responsible for gas porosities in casting and defects such as pores. The H dissolves in Al at high temperature and generates porosity as the temperature declines which in turn adversely influences the mechanical properties. Increasing the H content leads to an increase in both the number and the average size of the pores formed because H occupies interstitial positions in Al alloys causing expansion of the crystal lattices. The presence of H in the master alloy is because of the production process of the master alloy which uses elemental gas or water atomized powder. Therefore, precautions must be taken to reduce the exposure of the molten metal to atomic hydrogen.

4.2.2 Microstructural and phases analysis of the as-received master alloy.

The micrograph of the as-cast 60Al-40V master alloy produced by the aluminothermic process exhibited its microstructure, which is typically a dendritic structure, as illustrated in Figure 4-6.

Dendrite microstructures form by segregation solidification in most alloys during processes such as casting or welding. Therefore, the solidified morphology consisted of large dendrite grains in which primary dendrite grains form along the direction of the cooling and secondary dendrites form on both sides of the primary dendrite.

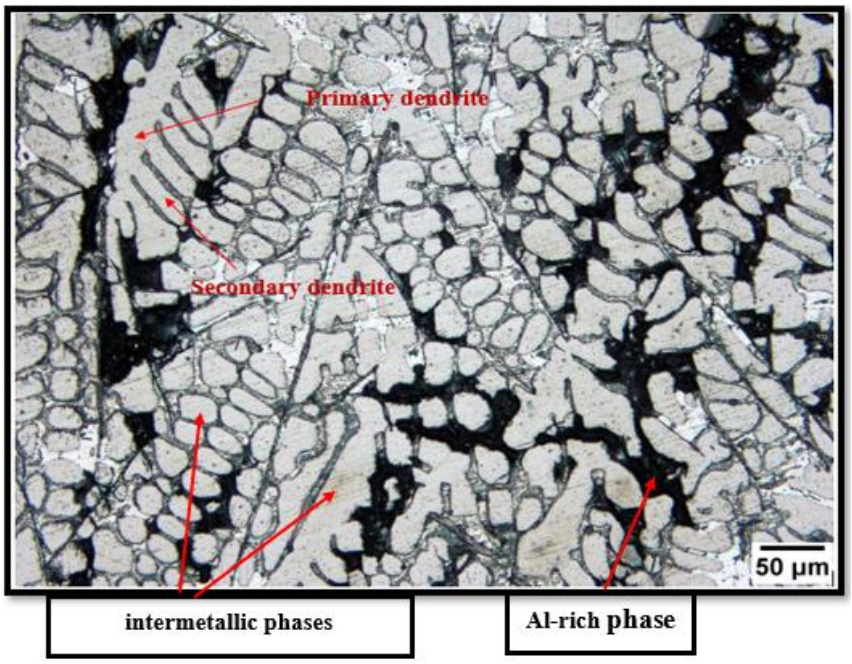

Figure 4-6: Micrograph of the as-cast 60Al-40V master alloy produced by the aluminothermic process.

In Figure 4-6, the microstructure depicts the dendritic growth of the dominant phase represented by the grey colour (primary dendrite) with secondary arms (secondary dendrites) forming on both sides of the primary dendrite. The SEM micrographs of the as-cast 60Al-40V show a similar morphology of Al-V intermetallic phases as was observed under the light optical microscope. This is a typical dendritic structure, characteristic of Al-based metals. Three phases were identified namely, the grey, light grey and dark grey (black) phases indicated by 1, 2, and 3 respectively as shown in Figure 4-7 (b). The details about the identity of these phases are given in Table 4-6.

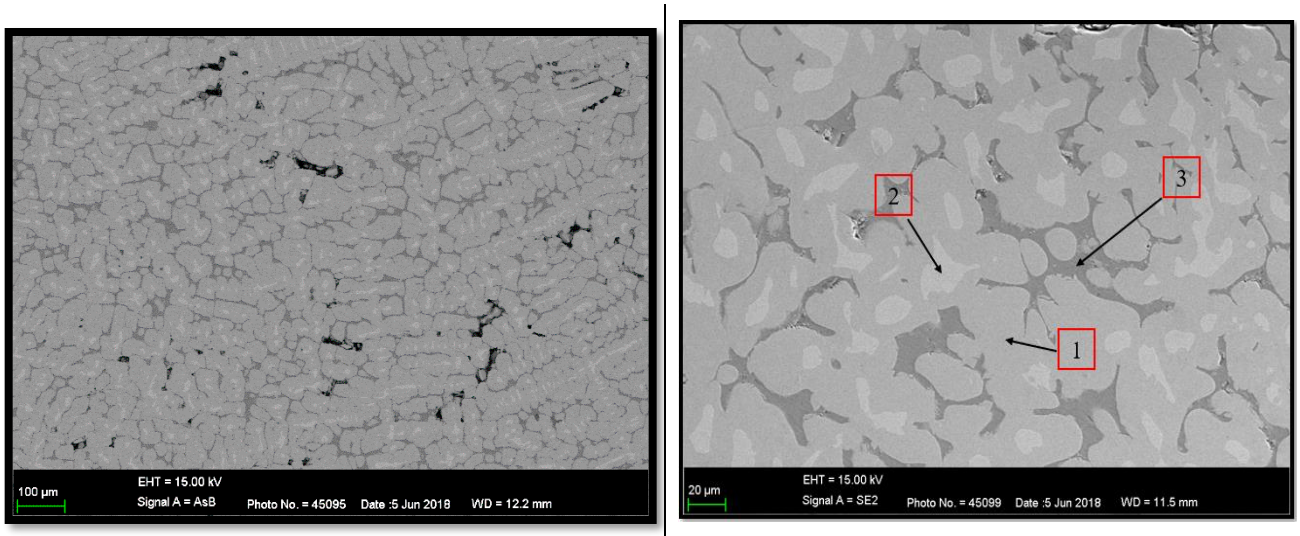

(a). (b).

Figure 4-7: SEM micrographs of the 60Al-40V master alloy at low and high magnifications, (a) and (b) respectively.

Figure 4-8 shows the typical micrograph and the EDX spectrum taken from a large area, region 1 of the as-cast master alloy. The EDX's elemental analysis revealed that the alloy was dominated by Al and V elements with 61.8 wt. % Al and 38.2 wt. % V.

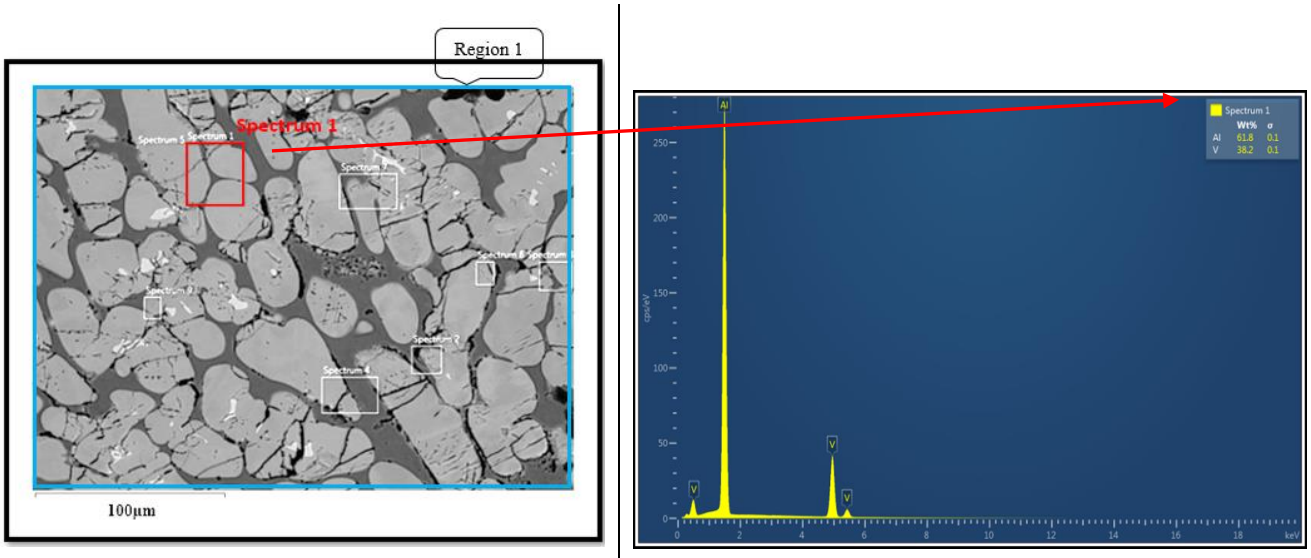

(a). (b).

Figure 4-8: (a) Micrograph and (b) the EDX spectrum taken from region 1.

Results of several EDX analyses carried from the same sample in order to establish the homogeneity of the alloy are presented in Figure 8-1 to Figure 8-16 in (Appendix A). Table 4-6 gives a summary of all the observed elemental compositions of Al and V in the alloy following the EDX analysis done on the samples. The results further confirm the microstructural findings which reveal three phases namely the grey, light grey and dark grey (black) to be dominated by the Al and V elements. The intermetallic phases were found to be the $Al_{21}V_2$, $Al_{23}V_4$, Al_3V and Al_8V_5.

Table 4-6: Summary of phases and elemental compositions according to the EDX analysis

Region	**Spectrum**	**Phase description**	**Composition**		**Phases**
			Al [wt.%]	V [wt.%]	
1	1	Grey phase	61.77	38.23	$Al_3V + Al_8V_5$
	2	Dark grey phase	96.61	3.39	Al_fcc +$Al_{21}V_2$
	3	Dark grey phase	97.21	2.79	Al_fcc + $Al_{21}V_2$
	4	Grey phase	62.58	37.42	$Al_3V + Al_8V_5$
	5	Grey phase	62.90	37.10	$Al_3V + Al_8V_5$
	6	Light grey phase	71.33	28.67	$Al_{23}V_4 + Al_3V$
	7	Grey phase	62.98	37.02	$Al_3V + Al_8V_5$
	8	Dark grey phase	98.30	1.70	Al_fcc +$Al_{21}V_2$
	9	Dark grey phase	98.90	1.10	Al_fcc +$Al_{21}V_2$
2	16	Grey phase	61.20	38.80	$Al_3V + Al_8V_5$
	17	Dark grey phase	92.20	7.80	Al_fcc +$Al_{21}V_2$
3	22	Grey phase	61.22	38.78	$Al_3V + Al_8V_5$
	23	Light grey phase	48.23	51.77	$Al_{23}V_4 + Al_3V$

The EDX mapping analysis, typically, shown in Figure 4-9, was performed on four selected regions and their spatial elemental composition is summarised in Table 4-7.

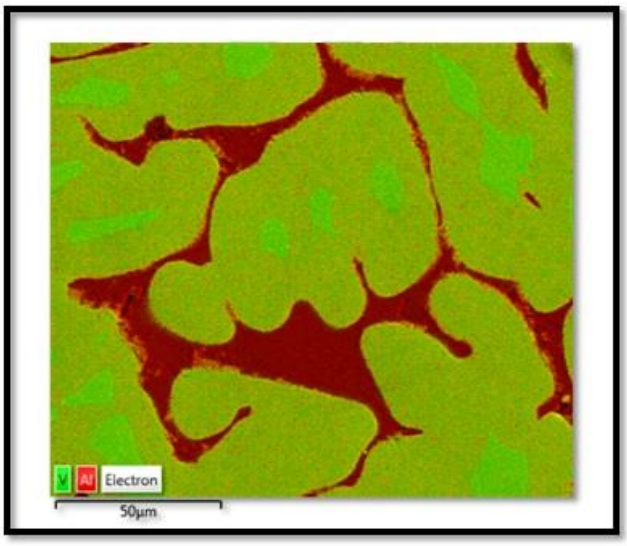

(a).

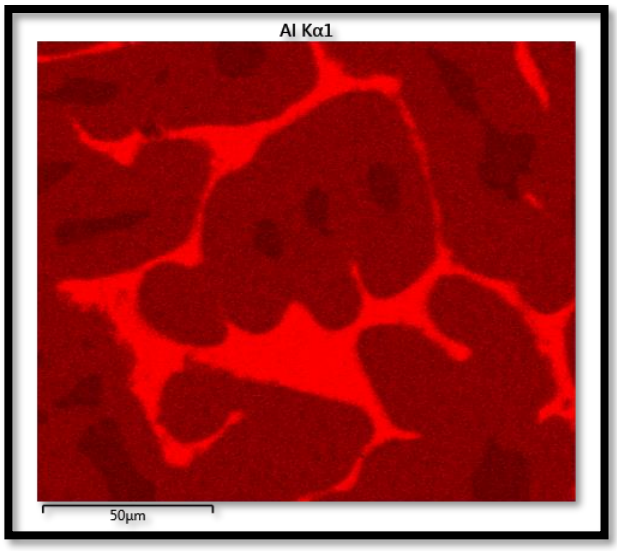

(b).

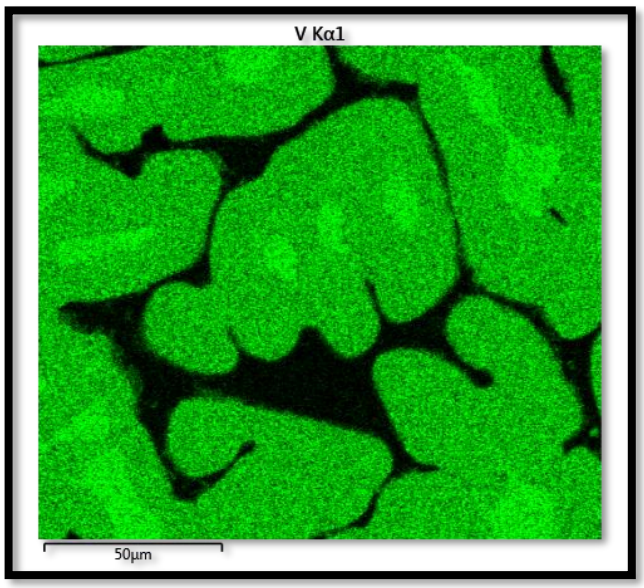

(c).

Voltage:15kV

Time of each analysis: 10 min (maps)

Element	wt.%	% Error	Atomic %
Al	65.00	± 0.03	77.81
V	35.00	± 0.03	22.19
Total:	100.00		100.00

(d).

Figure 4-9: SEM-EDX electron image (Scan 1), (a) elemental distribution, (b) Al K series, (c) V K series of the master alloy, (d) the average elemental composition of the scanned area (scan 1).

Figure 4-9, shows the typical SEM/EDX electron image (Scan 1) and the elemental distribution in the material. The selected regions on the sample were scanned to reveal the spatial distribution of the Al and V elements contained in the material. Different EDX spectra were taken on similar micrographs of the 60Al-40V master alloy and their respective spatial elemental distribution in the material (scan 2 to 4) are presented in Figure 8-17 to Figure 8-19 in (Appendix A). Table 4-7 presents the EDX- analysis' summary of the elemental chemical compositions in the produced 60Al-40V master alloy.

Table 4-7: EDX mapping analysis- Summary of the elemental chemical composition in the produced Al-V master alloy.

Analysis	**Elements**	**Wt. %**	**% Error**	**Atomic %**
EDX scan 1	**Al**	65.00	± 0.03	77.81
	V	35.00	± 0.03	22.19
EDX scan 2	**Al**	62.13	± 0.07	75.60
	V	37.87	± 0.07	24.40
EDX scan 3	**Al**	61.44	± 0.06	75.05
	V	38.56	± 0.06	24.95
EDX scan 4	**Al**	63.05	± 0.03	76.31
	V	36.95	± 0.03	23.69
Average	**Al**	**62.91**	± **0.05**	**76.20**
	V	**37.09**	± **0.05**	**23.80**

As may be seen from Figure 4-9 and Table 4-7, the average composition of Al was found to be 63 wt. % and that of V 37 wt. % with a standard deviation of 5 and 4 wt. % respectively. The average elemental composition of the produced alloy was found to be comparable to the theoretical 60Al-40V master alloy as well as the ICP analysis.

4.2.3 Microstructures and EDX results after DSC-TG thermal analysis.

Figure 4-10 compares the optical microstructures before and after the DSC-TG tests and as may be seen, the dendritic morphology remained the same. In other words, the dendrites microstructures did not dissolve after the two heating/cooling cycles during the DSC-TG tests but simply globularised. The three phases depicted as grey, light grey and dark grey (black) in the as-cast microstructures were still observed after the two DSC-TG heating/cooling tests.

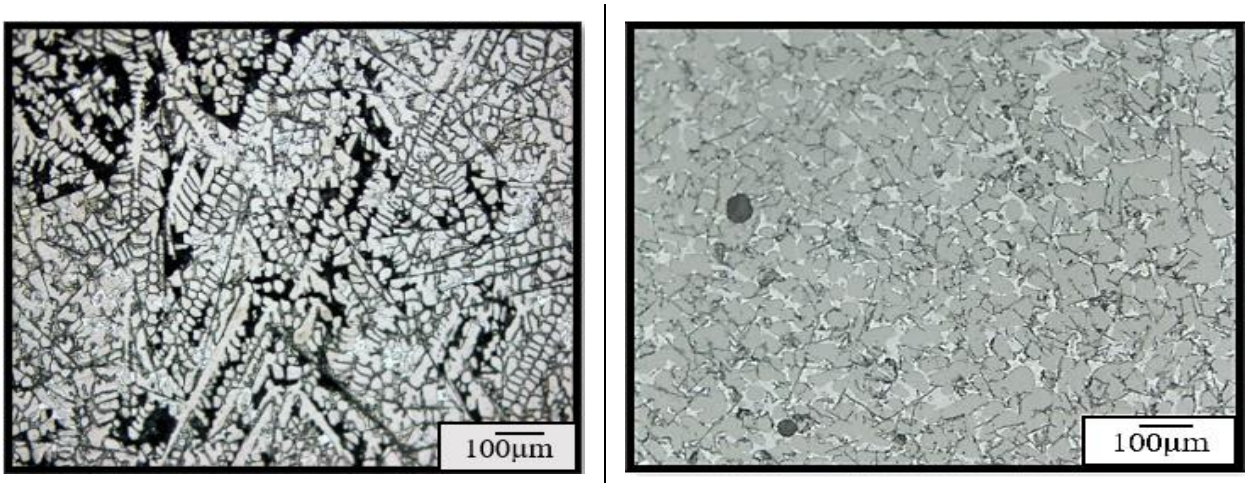

(a). (b).

Figure 4-10: The optical micrographs a) before the DSC-TG test, and b) after the DSC -TG test at a temperature of 1300 °C

Figure 4-11 compares the SEM micrographs of the 60Al-40V alloy before and after the thermal phase stability DSC-TG tests at temperatures of 1100, 1300 and 1400 °C respectively, after the double heating-cooling cycles. The phases identified in the SEM images are grey; labelled as A (the Al_3V and Al_8V_5 phases), light grey; labelled as B (the $Al_{21}V_2$ phase) and (black) or dark grey as C (the Al-rich phase) in Figure 4-11.

Figure 4-11 (a) shows the dendritic structure of the dominant Al_3V phase in the Al-matrix before heat treatment (as-cast conditions), the same dendritic morphology is observed after DSC-TG tests in the material shown in (b) at 1100 °C (c) at 1300 °C, and (d) at 1400 °C, respectively.

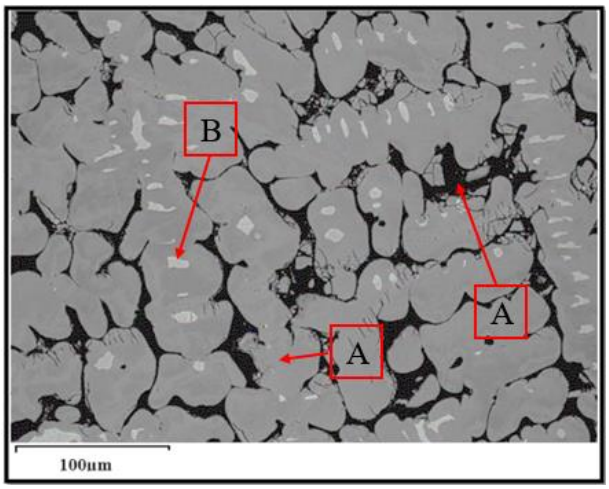

(a).

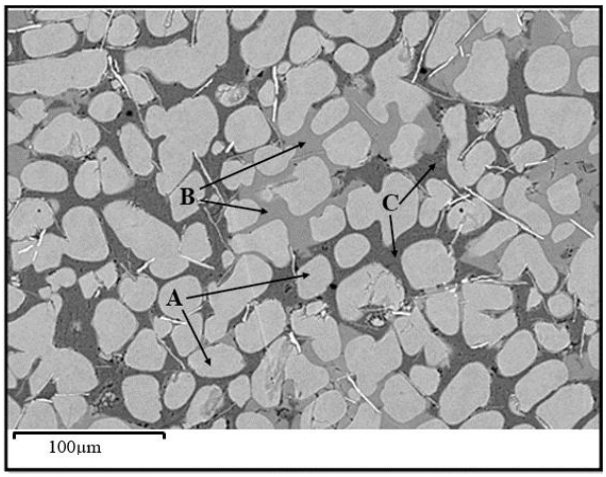

(b).

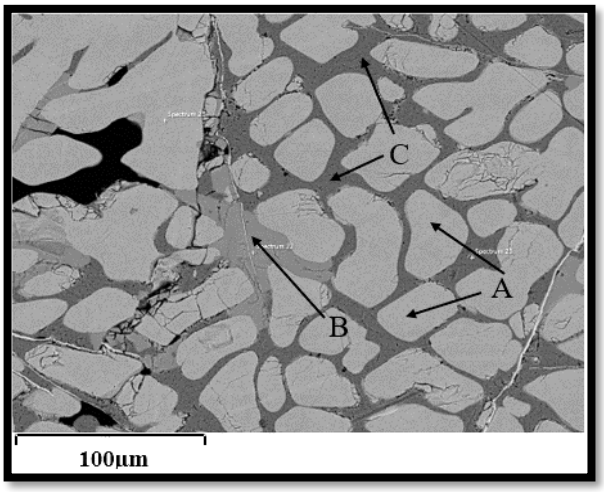

(c).

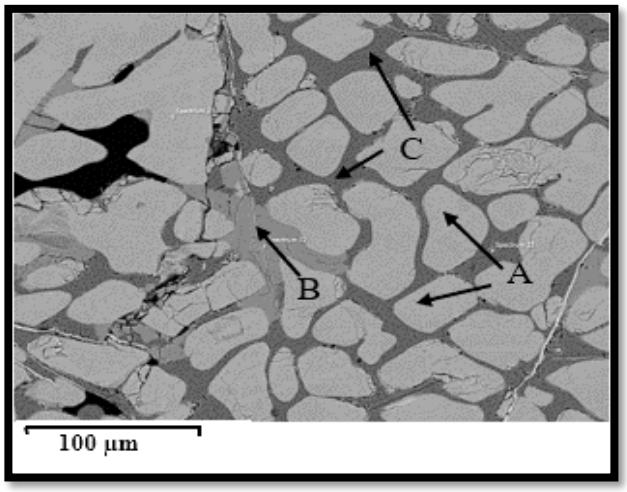

(d).

Figure 4-11: SEM micrographs of the 60Al-40V master alloy, (a) before DSC-TG test; (b) after DSC-TG test at 1100, (c) at 1300, and (d) at 1400 °C, respectively.

Combined with SEM images, EDX (point count) analysis was performed on the samples of the produced master alloy after DSC-TG tests at temperatures successively of 1100, 1300 and 1400 °C. Figure 4-12 shows a typical micrograph and EDX analysis after the DSC-TG test at the temperature of 1300 °C.

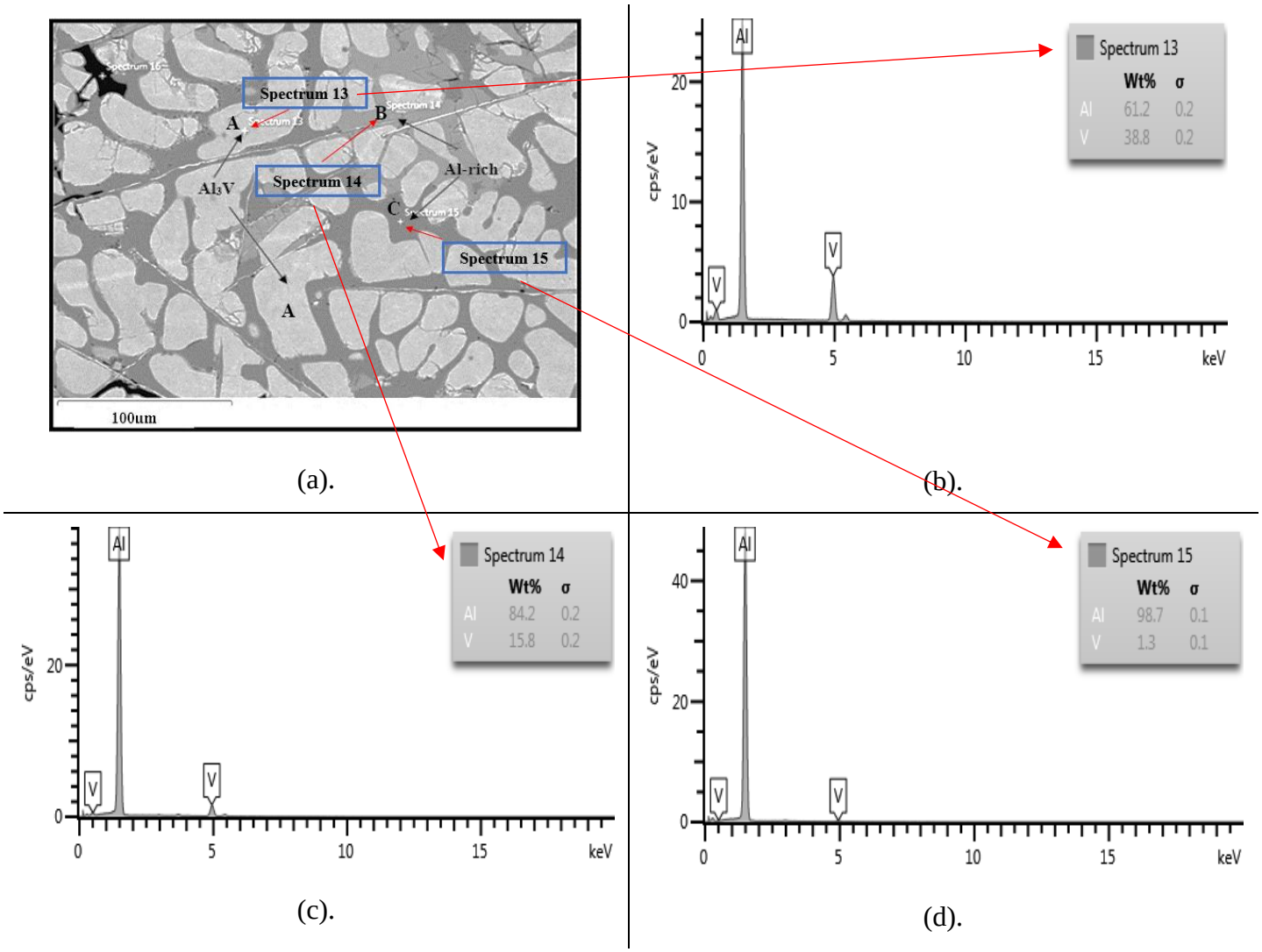

Figure 4-12: (a) SEM image, and EDX- spectra of (b) the grey (A), (c) light grey (B) (d) dark grey phase (C) after the DSC-TG test at the temperature of 1300 °C

Figure 4-12 shows the microstructure and EDX spectra after DSC-TG tests at the temperature of 1300 °C. Figure 8-20 and Figure 8-21 in (Appendix A) at temperatures of 1100 and 1400 °C, respectively. Similar observations were obtained for the three successive temperatures. It indicates that the three phases depicted as grey, light grey and dark grey were dominated by Al and V. The grey phase (A) was V rich (< 40 wt.% V), the light grey phase (B) and the dark grey phase (C) were Al-rich phases. The elemental composition of the Al and V in the material after DSC-TG at a temperature of 1300 °C is given in Table 4-8.

Table 4-8: Summary of phases formed in the material and elemental chemical compositions of the intermetallic phases obtained after the DSC-TG test at the temperature of 1300 °C.

Phase description	**Elemental composition**		**Phases**
	Al [wt.%]	V [wt.%]	
Grey (A)	61.2 ± 0.2	38.8 ± 0.2	Al_3V + Al_8V_5
Light grey (B)	84.2 ± 0.2	15.8 ± 0.2	Al-fcc + $Al_{21}V_2$
Dark grey (C)	98.7 ± 0.1	1.3 ± 0.1	Al-fcc + $Al_{21}V_2$

As indicated, the dominant grey phase (marked as A) was confirmed by the EDX analysis to be the Al_3V intermetallic with small homogeneous Al_8V_5. The light grey and dark grey phases which are Al-rich phases marked as B and C respectively consisted of the Al_fcc, with traces of V in the solution, namely the $Al_{21}V_2$ phase that did not dissolve completely in the alloy.

The microstructural evolution was determined using the thresholding, with the aid of Image J® software, and the linear intercept method after the heat treatment between 1100 and 1400 °C. The volume of the dominant Al_3V phase was determined through a combination of manual point count and thresholding methods. The results revealed the stability of the phases during heat treatment between 1100 and 1400 °C, Figure 4-13. The volume fraction of the Al_3V phase was determined to be between 78 and 81 % as shown in Figure 4-14. As may be seen, there wasn't a significant change in the volume fraction of this phase which confirmed its stability in this temperature interval. This agrees with the Thermo-Calc^{TM} predictions, i.e., the Al_3V phase was predicted to be the most stable phase in the Al-V system in the temperature range of 800 to1360 °C, (Figure 4-2).

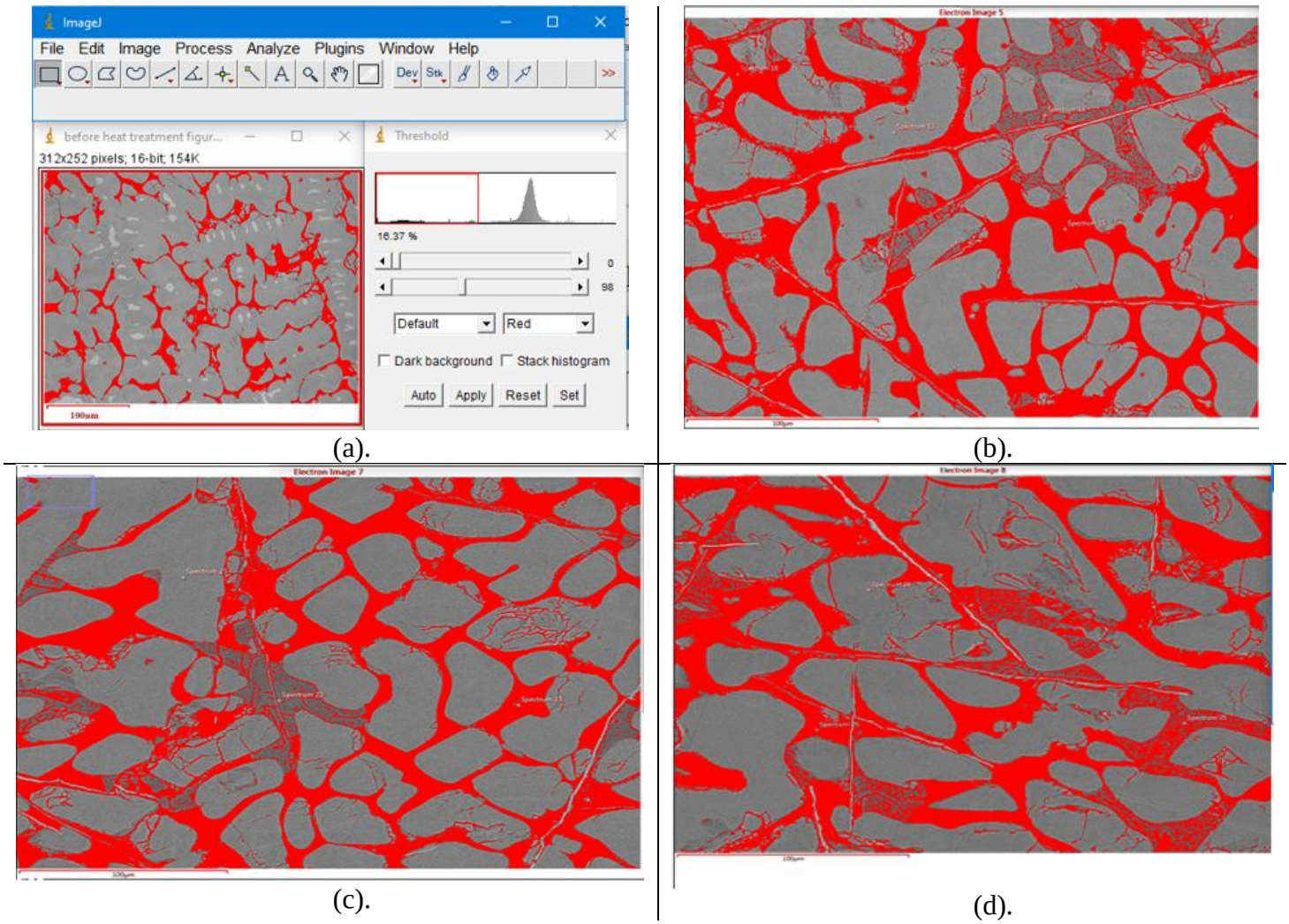

Figure 4-13:An illustration of the volume fraction of the Al_3V phase through thresholding procedure using the Image J ® software (a) before, and after DSC-TG test, (b) at 1100, (c) 1300, (d) 1400 °C, respectively.

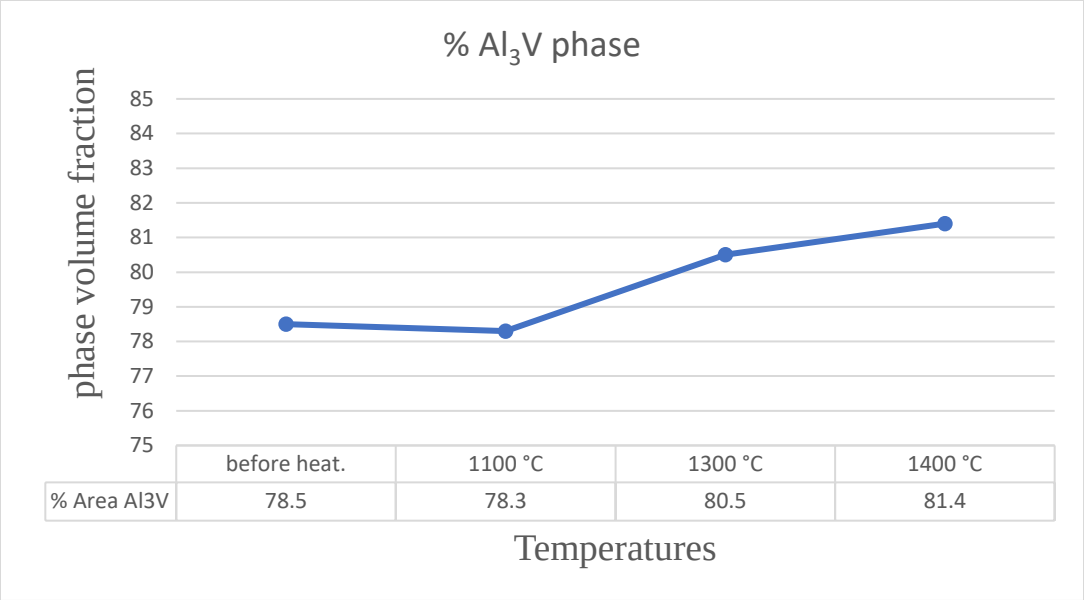

Figure 4-14: The Volume fraction of the Al_3V phase as a function of temperature

Figure 4-15 shows the X-ray diffraction (XRD) 2Θ scan of the alloy in the as-cast conditions. The XRD patterns showed peaks of diffraction, which corresponded to the crystalline intermetallic phases. The intensity peaks of the two intermetallic phases, namely the Al_3V and Al_8V_5 were detected in the analysis. However, the identified dominant peaks were of the Al_3V illustrated by high-intensity diffraction peaks and some low-intensity peaks of the Al_8V_5. The crystal structures were analysed to be cubic Al_3V (I4/mmm, tl8) and cubic Al_8V_5 (I-43m cl2) as illustrated in the International Centre of Diffraction Data (ICDD) [141]. It was observed that the main phases of the material both in the as-cast conditions and after reheating by the DSC-TG tests were the Al_3V and the Al_8V_5 intermetallic phases which were detected without any additional phase forming in the material.

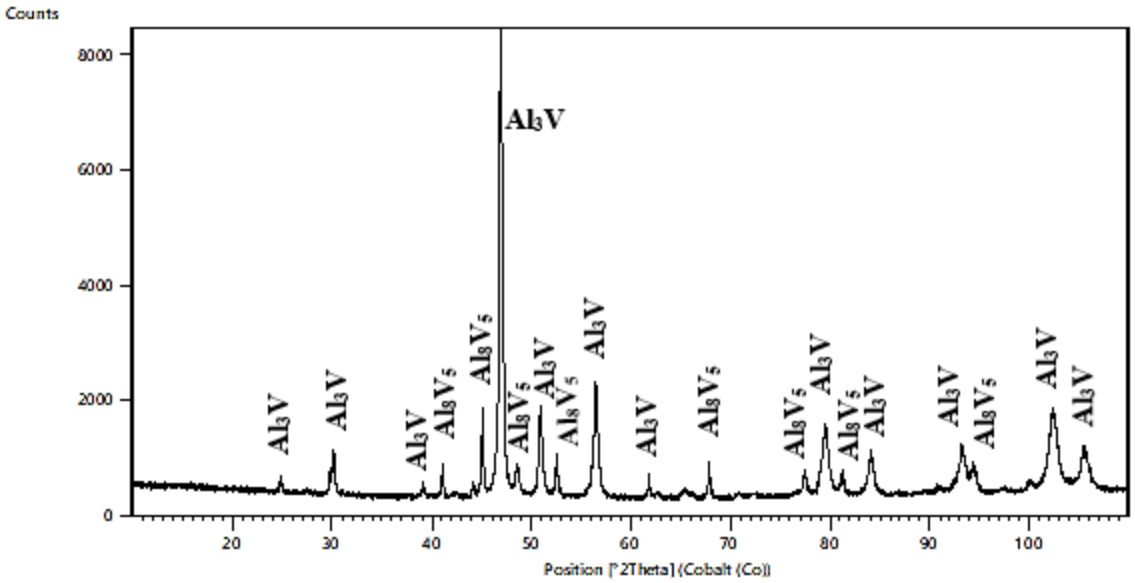

Figure 4-15: XRD spectrum of the as-cast 60Al-40V master alloy obtained by X' Pert High Score Plus software.

4.2.4 Thermal Analysis

Figure 4-16 shows, a typical DSC-TG graph showing the change in the heat flow as a function of temperature and the stability of phases in the material after the double heating-cooling cycle up to the temperature of 1300 °C. Figure 8-22 and Figure 8-23 in (Appendix A) show the change in the heat flow as a function of temperature and the stability of phases at the studied temperatures of 1100 and 1400 °C, respectively. As shown in Figure 4-16, the heating and cooling curves show peaks of transition temperatures, and no significant differences were observed between the two cycles. The same trend was observed in Figure 8-22 and Figure 8-23 in (Appendix A), for temperatures of 1100 and 1400 °C, respectively.

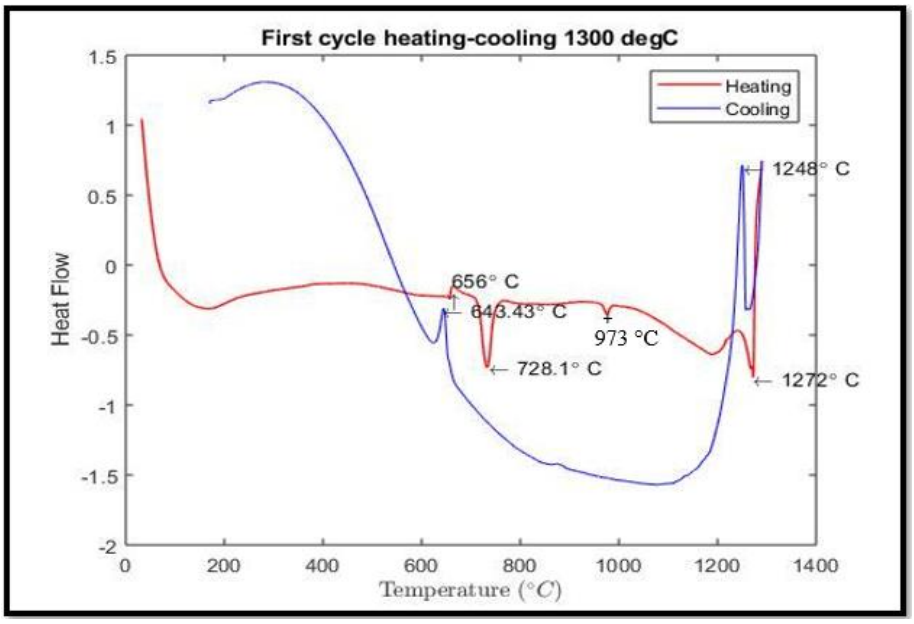

(a).

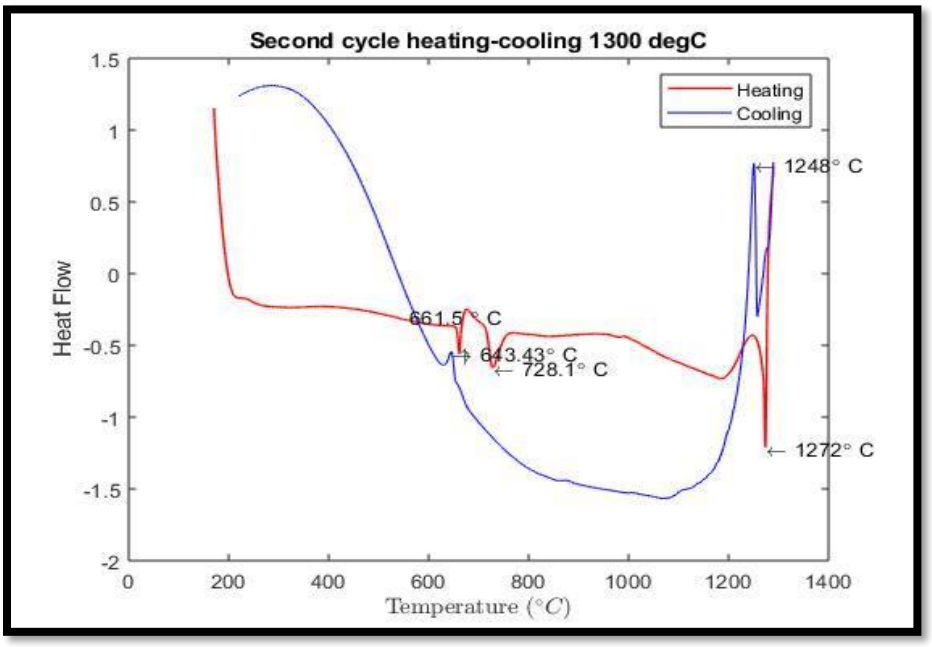

(b).

Figure 4-16: The change in the heat flow of the 60Al-40V master alloy as a function of temperature showing the phase stability, (a) for the 1st heating-cooling cycle, (b) for the 2nd heating-cooling cycle up to the temperature of 1300 °C.

The DSC trace curves in Figure 4-16(a) show that the phase transformations occurred at temperatures of 656, 728, 973 and 1272 °C for the heating process and 643 and 1248°C for the cooling in the 1st heating-cooling cycle. For the 2nd heating-cooling cycle, Figure 4-16(b) shows the transition temperatures occurring at 661, 728 and 1272 °C for the heating and 643 and 1248 °C for the cooling cycle, respectively. It also shows that phase transformations at 643 and 1248 °C were observed during both cooling processes which explain the presence of the Al_fcc with traces of V in the solution (the $Al_{21}V_2$ intermetallic phase) that did not dissolve completely in the material and the transformation of the Al_8V_5 intermetallic to Al_3V phase, respectively. The transformation temperatures with their corresponding phases are presented in Table 4-9. As expected, the transformation temperatures are not exactly the same due to the fact the Thermo-Calc™ assumes equilibrium conditions while the DSC-TG does not. Furthermore, there was a slight deviation in the V content from the ideal 60Al-40V master alloy.

Table 4-9: Peritectic temperatures [°C] of the compounds in Al-V alloys obtained by DSC-TG tests vs Thermo-Calc™ predictions.

Phases	**fcc**	**$Al_{21}V_2$**	**$Al_{45}V_7$**	**$Al_{23}V_4$**	**Al_3V**	**Al_8V_5**	**Process**
60Al-40V	664	672	696	735	1370	1660	Thermo-Calc™
63Al-37V	656/661	-	-	728	1272	-	1st and 2nd heating cycles (DSC-TG)
	643	-	-	-	1248	-	1st and 2nd cooling cycles (DSC-TG)

4.3 Microhardness

Intermetallic compounds provide higher hardness values in the material as compared to unalloyed metals. The hardness values of the dominant phases namely, the grey phase made of Al_3V+ Al_8V_5 ranged between 299 and 390 $HV_{0.05}$ and that of the Al-rich phases ranged between 117 and 208 $HV_{0.05,}$ respectively. Microhardness measurements indicated that higher hardness values were observed in the grey phases due to the two high-temperature intermetallic (Al_3V and Al_8V_5) components as compared to the Al-rich phase which was composed of Al_fcc, which is a softer

$Al_{21}V_2$ intermetallic phase. In other words, the average hardness value of the grey phase (with the dominant Al_3V) was found to be 337 $HV_{0.05}$ while that of the softer phase was found to be 154 $HV_{0.05}$. The higher hardness value observed in the grey phase was due to the presence of the dominant Al_3V which is known to enhance and improve the mechanical properties of the master alloy.

From the obtained results, the hardness values of the various phases were found to be relatively lower as compared to the conventionally fabricated 60Al-40V master alloy. In conventional PM methods, the key factor in the compactability of the powder blend of the matrix CP-Ti is to form a continuous contact with the hard MA (60Al-40V) particles. The final alloy product must be controlled for the master alloy to make it into fine powder for laser AM.

CHAPTER 5. DISCUSSION

5.1 Expected intermetallic phases based on the thermodynamic predictions.

The Al-V phase diagram in Figure 4-1 and the volume fractions of phases in Figure 4-2 were constructed using Thermo-Calc^{TM} software and databases, and the presence of intermetallics such as the $Al_{23}V_4$, Al_3V and Al_8V_5 were predicted as phases to form in the Al-V system.

It was observed that the predicted Al-V phase diagram did not show much difference in the compositions of the phases and the invariant temperatures (equations 4-1 to 4-6) as observed or calculated by [53], [63], [132], [142], [143] in the literature. The results of the peritectic temperatures of compounds compared to the literature (Table 4-2) are in agreement with the theoretical composition and experimental observations reported by other researchers [63],[37]. However, the main difference was in the solubility of Al in (V)_bcc at the invariant peritectic reactions of liquid + (V)_bcc $\rightarrow$ Al_8V_5 and liquid + Al_8V_5 $\rightarrow$ Al_3V which agrees with results observed by Massalki [132] but deviates from the findings of Richter and Ipser [57] with the two peritectic melting temperatures found to be 100 and 252 °C below the previously observed temperatures in the literature. This is because Thermo-Calc^{TM} presumed equilibrium conditions while in these experiments, non-equilibrium conditions were experienced.

The Al_3V phase with a large range of stability was observed in Figure 4-2, implying that the calculated Gibbs energy of the phase is stable too. The intermetallic phases in the Al-V system were described by the sublattice models, therefore, the values of the Gibbs free energy of mixing and enthalpy of formation of phases were found to be negatives as shown in Figure 4-3 and Figure 4-4, respectively. In the system, the Al_3V phase had the more negative values of the Gibbs free energy and enthalpy of formation, demonstrating its relatively higher stability. Negative values of the Gibbs free energy of the Al_3V were also reported by Bonnie at al. [76], Samokhval [77] and Dragana et al [142], [144], and for the enthalpy of formation by [80], Kubaschewski and Heymer [73], Z. Chen et al. [145], and E. Ghasali et al. [146]. However, other workers [49], [74] suggested that the enthalpy of formation of the Al_8V_5 should be more negative than that of the Al_3V phase. The argument is that the stable phase should be the one that can be found at low temperatures. In this work, from the predictions using Thermo-Calc^{TM} software, it can be concluded that the most

stable phase found in the Al-V system is the intermetallic Al_3V because a wide range of stability of the phase was found at lower temperatures as shown in Figure 4-2.

The mixing ability of components in the Al-V system was also investigated as shown in Figure 4-5. The results match very closely with the literature [76], [78], [79]. In the activity values of V and Al in the Al-V system, a strong negative deviation from ideal behaviour in the whole range of compositions was observed, as reported by many authors [126], [128]. The reason being, that the concept of zero excess entropy involving the random distribution of atoms for an ideal solution is unrealistic in practice, only a few systems approached ideality. Therefore, a deviation from Raoult's law is observed in most of the systems such as the Al-V system which are described as non-ideal solutions. The deviation from Raoult's law of activities of the Al and V components in the Al-V system indicates that a good mixing ability exists between the components. Therefore, it can be seen that the predicted Al-V phase diagram in relation to experimental data and thermodynamic properties of the system using the Thermo-Calc^{TM} software and databases are in good agreement with results in the literature.

5.2 Microstructures and phases in the produced Al-V master alloy

Both LOM and SEM micrographs obtained in Figure 4-6 and Figure 4-7, respectively compared to microstructures found in the literature [85], revealed a dendrite morphology with three coexisting phases characteristic of intermetallic Al-V alloys and much bigger grains that grow as dendritic structure. The reason is that the dendrite microstructure is the main microstructural constituent that forms during the solidification process of most Al-based alloys [89]. In fact, in the aluminothermic production of a master alloy such as the 60Al-40V alloy, heat is projected out due to the exothermic nature of the reaction during the reduction process, and when the temperature in the furnace rises to about 1900 °C (the melting point of V), the material melts and forms the intermetallic phases upon cooling. First, the Al powder reduces the V_2O_5 to V metal, and then the latter reacted with the molten Al to form intermetallic compounds. Upon solidification, this aluminothermic reaction results in an inhomogeneous Al-V alloy of the required compositions and the intermetallic phases formed, based on the Al-V phase diagram in Figure 4-1 and peritectic reactions at the invariant temperatures illustrated by equations 4-1 to 4-6.

The growth of dendritic microstructures is realised by the movement of the liquid/solid interface as a result of the deviation of the chemical equilibrium state at the solidification front. To support this, considering the solidification process of metals and alloys, dendritic structures result from constitutional supercooling at the liquid-solid interface. The homogeneous dendritic microstructures obtained in this work agreed with what is observed in most Al-based metals [37], [84], [89]. The same morphology was obtained after DSC-TG analysis, i.e., the dendritic structure did not dissolve completely due to the fast-cooling rate as shown in Figure 4-10 and Figure 4-11. Therefore, after the DSC-TG tests, the dendrite structure transformed to the globular structure. The globularisation was attributed to the dendrite fragmentation obtained when heating the as-cast materials in the solid-liquid region. It has been reported that the microstructural features are cooling rate-sensitive [147]. In other words, fast cooling rates led to significant microstructural refinement of the dendritic structure as well as globularisation, the latter was contrary to what others observed [148],[149].

The SEM was employed to determine the relationship between the composition of the phases and their final microstructures and to confirm the presence of the intermetallic phases. The analysis of the alloying elements by EDX spectra in Figure 4-8 and Figure 8-1 to Figure 8-16 in (Appendix A) show that the alloy's microstructures consisted of only the Al and V, which were presented in the form of intermetallic phases (Table 4-6). In other words, no other trace element was analysed.

Since the aluminothermic master alloy was non-stoichiometric, the EDX results showed that besides the expected Al_3V and Al_8V_5 intermetallic phases, the Al-rich phases ($Al_{23}V_4$ and $Al_{21}V_2$) were also found, Figure 4-8 and Table 4-6, respectively. This is contrary to what was observed by Masikane [25] using SEM and XRD analyses in an exactly 60 wt.% Al and 40 wt.% V master alloy whereby only the Al_3V and Al_8V_5 intermetallic phases were analysed. This master alloy was produced from the powder through the vacuum induction melting (VIM). This observation is in agreement with the Thermo-Calc^{TM} predictions in Figure 4-1 and Figure 4-2 as well as what others have found [84], [89], [150]. Figure 4-9 and Figure 8-17 to Figure 8-19 in (Appendix A) show that the EDX elemental composition of scanned areas and the average composition in the alloy of 62.9 wt.% Al and 37.1 wt.% V (Table 4-7) was found to be comparable to the theoretical 60Al-40V master alloy, this indicates that the aluminothermic process is an effective way of producing the master alloy when a suitable refractory-lined or water-cooled copper vessel is used.

However, after the DSC-TG tests, only the three intermetallic phases namely the $Al_{21}V_2$, Al_3V and Al_8V_5 were observed. Therefore, the intermediate $Al_{21}V_2$ phase observed in this work (Table 4-8) can be attributed to the increased Al content, which was above 60%, and the cooling rate. In other words, the $Al_{23}V_4$ phase could either be Al content or cooling rate dependent or both. The $Al_{21}V_2$ phase is occasionally found in as-cast alloys and cannot be easily distinguished from the Al phase especially under the optical microscope [63]. It is also worth noting that the $Al_{21}V_2$ phase and Al-rich phase are very close in chemical compositions and, therefore their transformations are indistinguishable, Table 4-9 and Figure 4-16.

The XRD patterns in Figure 4-15 show two major peaks of the intermetallic phases namely Al_3V and Al_8V_5. These were indexed and identified based on the crystallographic structure of phases in the International Centre for Diffraction Data (ICDD) [141]. The Al_3V consisted of a cubic crystal structure (a= 3.78 Å, belonging to the space group I4/mmm, # 139 space group number) and the Al_8V_5 reported had a cubic crystal structure (a= 9.234 Å, belonging to the space group I-4 3m cl2, # 139 space group number). The EDX technique was successfully used to analyse all the predicted phases namely, the Al_3V, the Al_8V_5 and the $Al_{21}V_2$ phase, whereas the XRD technique could reveal correctly only major phases namely, the Al_3V and Al_8V_5 phase. This can be attributed to the fact that compounds with lesser intensity peaks such as the $Al_{21}V_2$ and $Al_{23}V_4$ phases cannot be observed in the XRD patterns when in presence of the highly crystalline compounds such as the Al_3V and Al_8V_5 with high-intensity peaks. The reason being that minor peaks can sometimes be lost in the background noise and, therefore, are not detectable [151].

It was also observed that the samples of the as-cast master alloy were brittle. This is observed in most intermetallic phases because high strength materials are expected to be brittle at room temperature [152]. The micro-Vickers hardness measurements on localized phases, namely the grey phase composed of the Al_3V and Al_8V_5 phases were found to be higher than the light grey or dark grey phase which were composed of the softer phases namely the Al-rich phase ($Al_{21}V_2$) and $Al_{23}V_4$. This was expected because, in Al-V alloys, the hardness increases with an increase in the V content [153]. The high hardness values are attributed to grain refinement [154], [155] and solid strengthening by the V [156]. The 60Al-40V master alloy is considered a semi-finished product in the Ti industry for the production of the Ti-6Al-4V alloy. However, Ti is known to suffer from grain growth during annealing under continuous heating conditions and this affects the properties

including mechanical strength and hardness [25]. It is also known that the hardness of the intermetallic compounds is higher than the unalloyed metals [157], therefore, the presence of the Al_3V and Al_8V_5 intermetallic phases with their higher hardness in the produced 60Al-40V master alloy will enhance and improve the mechanical properties and hardness of Ti-6Al-4V alloy.

The DSC-TG analysis was performed to confirm if the transformation temperatures agreed with the Thermo-Calc^{TM} phase transformation predictions. A slight difference in the transformation temperatures was observed (Table 4-9). As may be seen, all transformation temperatures measured by the DSC-TG were found to be lower than those predicted by the Thermo-Calc^{TM} (Table 4-9). This was expected because the Thermo-Calc^{TM} calculations assume equilibrium conditions. It can be seen that during the solidification process, undercooling occurred, and the temperature peaks tend to be lower during the cooling than during the heating cycle as shown in Table 4-9. Another reason has been that the transformation temperatures are heating/cooling rate dependent. A high heating rate generally tends to move the peaks to higher temperatures [158], while a high cooling rate tends to suppress the nucleation start temperature [159].

Furthermore, it is worth noting that the transformation temperatures in Figure 4-16 observed at 1272 and 728 °C, corresponded to the invariant reactions of the $L+Al_8V_5 \rightarrow Al_3V$ and $L+Al_3V \rightarrow Al_{23}V_4$, respectively. This was found to be in agreement with Richter [57], especially for the invariant reaction $L+Al_8V_5 \rightarrow Al_3V$ (1270 °C) and to the lesser degree $L+Al_3V \rightarrow Al_{23}V_4$ at 728 instead of 736 °C. The peak that occurred at 643°C corresponded to the invariant reaction of the $L+ Al_{21}V_2 \rightarrow$ Al_fcc (664 °C) as predicted by Thermo-Calc^{TM}. This suggests that these reactions are cooling rate and Al content-sensitive.

In total, three phase transformations were observed using the DSC-TG and EDX methods as opposed to the XRD method. This could be attributed to the higher sensitivity of the two former techniques in detecting phase transformations and, therefore, it was possible to identify all the three possible phase transformations under non-equilibrium conditions in this 63Al-37V master alloy.

CHAPTER 6. CONCLUSIONS AND RECOMMENDATIONS

6.1 Conclusions

The thermodynamic calculation of the Al-V binary system, as well as microstructural, and phases characterisation analyses were performed on the 60Al-40V master alloy produced via the aluminothermic process. From the thermodynamic predictions, the production of 60Al40V master alloy and its phases analyses, the following conclusions were drawn:

1. The thermodynamic parameters such as enthalpy, Gibbs free energy and activities of constituents and phases predicted in the Al-V binary system using Thermo-Calc^{TM} software were found to be in good agreement with the experimental results from this work in particular the phase transformation temperatures of the constituent phases.
2. A master alloy with an average composition of 63 wt.% Al -37 wt.% V was produced by the aluminothermic reaction process.
3. The average EDX elemental analysis found agreed well with the average elemental composition range of the combination of the two major phases namely the Al_3V and Al_8V_5 phases of the Al-V alloy system.
4. Besides the two major phases (Al_3V and Al_8V_5 phases), the $Al_{21}V_2$ and $Al_{23}V_4$ phases were found to be prevalent in the 60Al-40V master alloy, although in small amounts during the aluminothermic production process. These phases were still persistent even after the two heating and cooling cycles to and from a temperature of 1400 ^oC respectively.
5. The amount of Al_8V_5 phase formed was found to decrease with decreasing temperature and decreasing V content, while the converse was found to be true for the Al_3V.
6. The dendritic microstructures remained unchanged even after the two heating and cooling cycles to a temperature of 1400 ^oC and this signified the microstructural stability of this master alloy.

6.2 Recommendations

Based on results obtained from this work, the following recommendations have been made for further work:

1. Further work to quantitatively determine the volume fraction of the two major phases (Al_3V and Al_8V_5 phases), and the $Al_{21}V_2$ and the $Al_{23}V_4$ phases prevalent in the 60Al-40V master alloy must be done through the EBSD technique.
2. These persistent phases can be also measured and determined using TEM measurements (morphology or microstructure of phases) to provide further information on the $Al_{21}V_2$ and the $Al_{23}V_4$ phases which could not be detected under optical and scanning electron microscopy.

CHAPTER 7. REFERENCES

[1] K. Jayakrishna, V. R. Kar, M. T. H. Sultan, and M. Rajesh, *Materials selection for aerospace components*, no. July 2019. Elsevier Ltd, 2018.

[2] V. Arkel, "hardness. Unlike other substances that may contain metallic," pp. 1–13, 2020.

[3] O. M. Ivasishin, V. M. Anokhin, A. N. Demidik, and D. G. Sawakin, "Cost-effective blended elemental powder metallurgy of titanium alloys for transportation application," *Key Eng. Mater.*, vol. 188, pp. 55–62, 2000, doi: 10.4028/www.scientific.net/kem.188.55.

[4] H. Wang, "Thermodynamic modelling of high strength, high toughness Ti alloys," no. February, p. 157, 2012, [Online]. Available: https://drive.google.com/open?id=0B0fTxDBXtHZMdy1PQUhEbXlERzg.

[5] C. Veiga, A. J. R. Loureiro, and J. P. Davim, "Properties and applications of titanium alloys," *Rev. Adv. Mater. Sci.*, vol. 32, p. s. 133-148, 2012.

[6] N. Haghdadi, A. B. Phillion, and D. M. Maijer, "Microstructure Characterization and Thermal Analysis of Aluminum Alloy B206 During Solidification," vol. 46, no. May, pp. 2073–2081, 2015, doi: 10.1007/s11661-015-2780-0.

[7] J. R. Davis, "Aluminum and Aluminum Alloys," pp. 351–416, 2001, doi: 10.1361/autb2001p351.

[8] C. Karthikeyan, D. Veeraragavathatham, D. Karpagam, and S. A. Firdouse, "Traditional tools in agricultural practices," vol. 8, no. April, pp. 212–217, 2009.

[9] M. Niinomi, M. Nakai, and J. Hieda, "Development of new metallic alloys for biomedical applications," *Acta Biomaterialia*. 2012, doi: 10.1016/j.actbio.2012.06.037.

[10] C. B. Carter and M. G. Norton, *Ceramic materials: Science and engineering*. 2013.

[11] H. L. Bosman, "Influence of powder particle size distribution on the press – and – sinter titanium and Ti – 6Al – 4V preforms," no. March 2016.

[12] Willey and Son, *Intermetallic compounds-Principles and Practice*, John Wiley., vol. 3, no. 9. New York, USA, 2015.

[13] H. Warlimont, "Titanium and titanium alloys," in *Springer Handbooks*, 2018.

[14] M. Peters, J. Hemptenmacher, J. Kumpfert, and C. Leyens, "Structure and Properties of Titanium and Titanium Alloys," in *Titanium and Titanium Alloys*, 2005.

[15] S. J. Oosthuizen, "Titanium: the innovators' metal - Historical case studies tracing titanium process and product innovation," *J. South. African Inst. Min. Metall.*, vol. 111, no. 11, pp. 781–786, 2011.

[16] D. Carou, E. M. Rubio, B. Agustina, and M. M. Marín, "Experimental study for the effective and sustainable repair and maintenance of bars made of Ti-6Al-4V alloy. Application to the aeronautic industry," *J. Clean. Prod.*, vol. 164, pp. 465–475, 2017, doi: 10.1016/j.jclepro.2017.06.095.

[17] M. Peters and C. Leyens, *Titanium and Titanium Alloys: Fundamentals and Applications*. 2003.

[18] R. R. Boyer, "An overview on the use of titanium in the aerospace industry," *Mater. Sci. Eng. A*, 1996, doi: 10.1016/0921-5093(96)10233-1.

[19] I. Inagaki, T. Takechi, Y. Shirai, and N. Ariyasu, "Application and features of titanium for the aerospace industry," *Nippon Steel Sumitomo Met. Tech.*, vol. 106, no. 106, pp. 22–27, 2014, [Online]. Available: https://www.nipponsteel.com/en/tech/report/nssmc/pdf/106-05.pdf.

[20] M. Niinomi, "Mechanical biocompatibilities of titanium alloys for biomedical applications," *Journal of the Mechanical Behavior of Biomedical Materials*. 2008, doi: 10.1016/j.jmbbm.2007.07.001.

[21] H. J. Rack and J. I. Qazi, "Titanium alloys for biomedical applications," *Mater. Sci. Eng. C*, 2006, doi: 10.1016/j.msec.2005.08.032.

[22] I. Gurrappa, “Characterization of titanium alloy Ti-6Al-4V for chemical, marine and industrial applications,” *Mater. Charact.*, 2003, doi: 10.1016/j.matchar.2003.10.006.

[23] R. M. German, “German, Sintering theory and practice,” *Chapitre*. 1996.

[24] J. Capus, “Conventional PM still a challenge for titanium and alloys,” *Met. Powder Rep.*, vol. 69, no. 6, pp. 18–20, 2014, doi: 10.1016/S0026-0657(14)70274-7.

[25] M. A. Masikane, “Investigation into the microstructure and tensile properties of unalloyed titanium and Ti-6Al-4V alloy produced by powder metallurgy, casting and layered manufacturing,” 2015.

[26] I. Technology, “The AI-Pt-Ru ternary phase diagram.”

[27] I. Polmear, D. StJohn, J.-F. Nie, and M. Qian, “Casting of Light Alloys,” in *Light Alloys*, 2017.

[28] K. Jiang and X. Liu, “The effect of melting temperature and time on the TiC particles,” *J. Alloys Compd.*, 2009, doi: 10.1016/j.jallcom.2009.04.112.

[29] P. Sepehrband, R. Mahmudi, and F. Khomamizadeh, “Effect of Zr addition on the ageing behavior of A319 aluminium cast alloy,” *Scr. Mater.*, 2005, doi: 10.1016/j.scriptamat.2004.10.025.

[30] H. A. Elhadari, H. A. Patel, D. L. Chen, and W. Kasprzak, “Tensile and fatigue properties of a cast aluminium alloy with Ti, Zr and V additions,” *Mater. Sci. Eng. A*, 2011, doi: 10.1016/j.msea.2011.07.018.

[31] Qui, Z. Yue, Y. Grjotheim, and K. Kvande, “Formation of Al-Mn master alloys by thermal reduction and by electrolysis of manganese dioxide in cryolite-alumina melts,” *Aluminium*, vol. 64, no. 2, pp. 603–605, 1988.

[32] Zhuxian, Q. and Zhondlin, Z. and Grjotheim, and H. Kvande, “Formation of Al-Si alloys by electrolysis and by thermal reduction of silica in cryolite-alumina melt,” *Aluminium*, vol. 63, pp. 1247–1250, 1987.

[33] Z.Qui, M.Zhang, Y. Yue, Z.Che, K. Grjotheim, and H. Kvande, “Formation of aluminium-titanium alloys by electrolysis and by thermal reduction of titania in cryolite-alumina melts,” *Aluminium*, vol. 64, no. 6, pp. 606–609, 1988.

[34] C. C. Koch, “Intermetallic matrix composites prepared by mechanical alloying - A review,” *Mater. Sci. Eng. A*, 1998, doi: 10.1016/S0921-5093(97)00824-1.

[35] C. Nishimura and C. T. Liu, “Reaction sintering of Ni3Al to near full density,” *Scr. Metall. Mater.*, 1992, doi: 10.1016/0956-716X(92)90616-M.

[36] “PRODUCTION OF MASTER ALLOYS FOR THE TITANIUM INDUSTRY BY THE GfE-two-STAGE-PROCESS R. Hahn, H.,” pp. 109–114.

[37] H. Wan, B. Xu, L. Li, B. Yang, D. Li, and Y. Dai, “A Novel Method of Fabricating Al-V Intermetallic Alloy through Electrode Heating,” *Metals (Basel).*, vol. 9, no. 5, p. 558, 2019, doi: 10.3390/met9050558.

[38] Y. M. Gorji, M. Soltanieh, and A. Habibolahzadeh, “Production of Al-Si master alloy by aluminothermic reduction of silica in molten cryolite,” *Can. Metall. Q.*, vol. 46, no. 4, pp. 385–390, 2007, doi: 10.1179/cmq.2007.46.4.385.

[39] M. Hosseinpouri, S. A. Mirmonsef, and M. Soltanieh, “Production of Al-Ti master alloy by aluminothermic reduction technique,” *Can. Metall. Q.*, vol. 46, no. 2, pp. 139–144, 2007, doi: 10.1179/cmq.2007.46.2.139.

[40] S. Hassan-Pour, C. Vonderstein, M. Achimovičová, V. Vogt, E. Gock, and B. Friedrich, “Aluminothermic production of titanium alloys (Part 2): Impact of activated rutile on process sustainability,” *Metall. Mater. Eng.*, vol. 21, no. 2, pp. 101–114, Jun. 2015, doi: 10.30544/100.

[41] A. M. G. T. Alloys, “GfE Metalle und Materialien GmbH MASTER ALLOYS Future Security of Supply With Master Alloys From a European Point of View,” 2013.

[42] D. D. Akerkar, “Physico Chemical Aspects Of Alumino-Thermic Reduction In The

Production Of Low Carbon Ferro-Alloys by," 1994.

[43] Z. Gao and H. Lu, "Preparation of Ti-Al-V alloys by aluminothermic reaction," *Energy Technol. 2016 Carbon Dioxide Manag. Other Technol.*, pp. 65–72, 2016, doi: 10.1007/978-3-319-48182-1_8.

[44] L. L. Wang, Z. A. Munir, and Y. M. Maximov, "Thermite reactions: their utilization in the synthesis and processing of materials," *Journal of Materials Science*. 1993, doi: 10.1007/BF00353167.

[45] G. K. Gupta and N. Krishnamurthy, "Extractive metallurgy of rare earths," *Int. Mater. Rev.*, 1992, doi: 10.1179/imr.1992.37.1.197.

[46] J. O. Andersson, T. Helander, H. L., P. F. Shi, and B. Sundman, "Computational tools for materials science," *Calphad*, 2002, doi: http://dx.doi.org/10.1016/S0364-5916(02)00037-8.

[47] J. O. Andersson, T. Helander, L. Höglund, P. Shi, and B. Sundman, "Thermo-Calc & DICTRA, computational tools for materials science," *Calphad Comput. Coupling Phase Diagrams Thermochem.*, vol. 26, no. 2, pp. 273–312, 2002, doi: 10.1016/S0364-5916(02)00037-8.

[48] S. Jin, Q. Chen, and J. Bratberg, "Thermodynamic calculations and precipitation simulations of HSLA steels," *7th Int. Conf. High Strength Low Alloy Steels, HSLA Steels 2015, Int. Conf. Microalloying 2015, Microalloying 2015 Int. Conf. Offshore Eng. Steels 2015, OES 2015*, vol. 1, pp. 173–177, 2015, doi: 10.1007/978-3-319-48767-0_16.

[49] Y. A. Chang *et al.*, "Phase diagram calculation: Past, present and future," 2004, doi: 10.1016/S0079-6425(03)00025-2.

[50] R. Schmid-Fetzer, "Phase Diagrams: The Beginning of Wisdom," *J. Phase Equilibria Diffus.*, 2014, doi: 10.1007/s11669-014-0343-5.

[51] P. Mason, A. Hope, and A. N. Grundy, "Applications of CALPHAD based tools to additive manufacturing," *2018 Stock. User Gr. Meet.*, p. 26, 2018, [Online]. Available:

https://drive.google.com/open?id=1L6i_7maAmUG29CBjjObbqZ_NVnveYJul.

[52] J. L. Murray, “Calculation of the titanium-aluminium phase diagram,” *Metall. Trans. A*, vol. 19, no. 2, pp. 243–247, 1988, doi: 10.1007/BF02652532.

[53] H. Okamoto, “Al-V (Aluminum-Vanadium),” *J. Phase Equilibria Diffus.*, vol. 33, no. 6, p. 491, 2012, doi: 10.1007/s11669-012-0090-4.

[54] S. Hassan-Pour, C. Vonderstein, M. Achimovičová, V. Vogt, E. Gock, and B. Friedrich, “Aluminothermic production of titanium alloys (Part 2): Impact of activated rutile on process sustainability,” *Metall. Mater. Eng.*, vol. 21, no. 2, pp. 101–114, 2015, doi: 10.30544/100.

[55] J. H. Choi, H. Chang, T. Ryu, C. W. Nam, and B. S. Kim, “Investigating the aluminothermic process for producing ferrotitanium alloy from ilmenite concentrate,” *Metals (Basel).*, vol. 10, no. 11, pp. 1–14, 2020, doi: 10.3390/met10111493.

[56] J. L. Murray, “AI-V (Aluminum-Vanadium),” vol. 10, no. 4, pp. 351–357, 1989.

[57] K. W. Richter and H. Ipser, “Al-V phase diagram between 0 and 50 atomic percent vanadium,” *Zeitschrift fuer Met. Res. Adv. Tech.*, vol. 91, no. 5, pp. 383–388, May 2000.

[58] W. Gong, Y. Du, B. Huang, R. Schmid-Fetzer, C. Zhang, and H. Xu, “Thermodynamic reassessment of the Al-V system,” *Zeitschrift fuer Met. Res. Adv. Tech.*, 2004, doi: 10.3139/146.018057.

[59] A. Kroupa, M. Mazalová, and K. W. Richter, “The reassessment of the Al-V system and new assessment of the Al-Si-V system,” *Calphad Comput. Coupling Phase Diagrams Thermochem.*, vol. 59, no. July, pp. 47–60, 2017, doi: 10.1016/j.calphad.2017.08.001.

[60] H. Okamoto, “Al-V (Aluminum-Vanadium),” *Journal of Phase Equilibria and Diffusion*, vol. 33, no. 6. Springer New York LLC, p. 491, Dec. 01, 2012, doi: 10.1007/s11669-012-0090-4.

[61] H. Okamoto, “Al-V (Aluminum-Vanadium),” *J. Phase Equilibria*, vol. 22, no. 1, p. 86,

2001, doi: 10.1361/105497101770339355.

[62] A. Kostov, D. Zivkovic, and B. Friedrich, “Thermodynamic study of Ti-V and Al-V systems using FactSage,” *J. Min. Metall. Sect. B Metall.*, vol. 42, no. 1, pp. 57–65, 2006, doi: 10.2298/jmmb0601057k.

[63] H. W. O. Carlson, D. Kennedy, “The aluminium-vanadium alloy system,” *Am. Soc. Met.*, vol. 47, pp. 520–537, 1955.

[64] K. W. Richter and H. Ipser, “Al-V phase diagram between 0 and 50 atomic percent vanadium,” *Zeitschrift fuer Met. Res. Adv. Tech.*, 2000.

[65] Q. Li, Z. Chen, Q. Luo, and B. Li, “Experimental investigation and thermodynamic calculation of the Al-rich corner in the ternary Al-Ti-V system,” vol. 115, pp. 339–347, 2017.

[66] C. Oceanography, “Thermodynamics2012.pdf,” pp. 1–18, 2012.

[67] I. Muller, *A history of thermodynamics: the doctrine of energy and entropy*. Springer Science/ Media business, 2007.

[68] A. Achari, “Thermodynamic properties of some liquid alloys,” 1969.

[69] Y. a. Çengel, “Thermodynamics: An Engineering Approach,” *McGraw-Hill*, 2004.

[70] Z. Chen *et al.*, “First-principles investigation of thermodynamic, elastic and electronic properties of Al3V and Al3Nb intermetallics under pressures,” *J. Appl. Phys.*, 2015, doi: 10.1063/1.4913664.

[71] S. L. Shang *et al.*, “First-principles calculations of pure elements: Equations of state and elastic stiffness constants,” *Comput. Mater. Sci.*, 2010, doi: 10.1016/j.commatsci.2010.03.041.

[72] M. Jahnátek, M. Krajči, and J. Hafner, “Interatomic bonding, elastic properties, and ideal strength of transition metal aluminides: A case study for Al 3(V, Ti),” *Phys. Rev. B* -

Condens. Matter Mater. Phys., 2005, doi: 10.1103/PhysRevB.71.024101.

[73] O. Kubaschewski and G. Heymer, "Heats of formation of transition-metal aluminides," *Trans. Faraday Soc.*, 1960, doi: 10.1039/tf9605600473.

[74] R. Kieffer, H. Nowotny, A. Neckel, P. Ettmayer, and L. Usner, "Zur Entmischung von kubischen Mehrstoffcarbiden," *Monatshefte für Chemie*, 1968, doi: 10.1007/BF00913751.

[75] S. V. Meschel and O. J. Kleppa, "Standard enthalpies of formation of some 3d transition metal silicides by high-temperature direct synthesis calorimetry," *J. Alloys Compd.*, 1998, doi: 10.1016/S0925-8388(97)00528-8.

[76] B. Lindahl, X. L. Liu, Z. K. Liu, and M. Selleby, "A thermodynamic re-assessment of Al-V toward an assessment of the ternary Al-Ti-V system," *Calphad Comput. Coupling Phase Diagrams Thermochem.*, 2015, doi: 10.1016/j.calphad.2015.07.002.

[77] V. A. samokhval V, Poleshchuk P., "Thermodynamic properties of aluminium-titanium- and aluminium-vanadium alloys," *Russ.J.Phys.chem*, vol. 45, no. 8, pp. 1174–1176, 1971.

[78] N. and M. Batalin, G. and Sudavtsova, "Thermodynamic properties of liquid binary alloys of the Al-Sc, Al-V and Al-Ti system," *Ukr. Khimicheskij Zhurnal*, vol. 51, no. 8, pp. 817–819, 1985.

[79] K. and M. Johnson, W. and Komarek, "Thermodynamic properties of the Cr-Al and Al-V systems," vol. 64, no. 285, 1967.

[80] B. Lindahl, X. L. Liu, Z. Liu, and M. Selleby, "CALPHAD : Computer Coupling of Phase Diagrams and Thermochemistry A thermodynamic re-assessment of Al – V toward an assessment of the ternary Al – Ti – V system," vol. 51, pp. 75–88, 2015.

[81] J. Wang *et al.*, "First-principles calculations of binary Al compounds: Enthalpies of formation and elastic properties," *Calphad Comput. Coupling Phase Diagrams Thermochem.*, 2011, doi: 10.1016/j.calphad.2011.09.009.

[82] S. V. Meschel and O. J. Kleppa, "The Standard Enthalpies of Formation of Some 3d

Transition Metal Aluminides by High-Temperature Direct Synthesis Calorimetry," in *Metallic Alloys: Experimental and Theoretical Perspectives*, 1994.

[83] R. Boulechfar, S. Ghemid, H. Meradji, and B. Bouhafs, "FP-LAPW investigation of structural, electronic, and thermodynamic properties of Al3V and Al3Ti compounds," *Phys. B Condens. Matter*, 2010, doi: 10.1016/j.physb.2010.06.053.

[84] T. American Society for Metals and Lyman, *Metals Handbook: metallography, structures and phase diagrams*. American society for metals, 1973.

[85] D. J. Kenney, "Aluminum-vanadium system," 1953.

[86] L. Varich, K. Burov, A. Kolesnichenko, and Maksimenko, "Highly supersaturated Al-V, Al-Mo, and Al-W solid solutions obtained at a high rate of cooling," *Metallography*, vol. 15, no. 2, pp. 111–113, 1963.

[87] A. Roth, "An investigation of the aluminium-vanadium system," *Metallography*, vol. 32, pp. 356–359, 1940.

[88] H. Carlson, ON and Kenney, DJ and Wilhelm, "The aluminium-vanadium alloy system," 1955.

[89] Q. Feng Zhu, Y. Meng, Y. Lei Kang, S. ping Kong, Y. peng Ou, and Y. bo Zuo, "Effect of cooling rate on morphology and type of vanadium-containing phases in Al-10V master alloy," *China Foundry*, vol. 16, no. 5, pp. 300–306, 2019, doi: 10.1007/s41230-019-9017-6.

[90] A. N. M. Omran, "Fabrication and characterization of Al-based in situ composites reinforced by Al3V intermetallic compounds," *Mater. Sci. Technol. Conf. Exhib. 2013, MS T 2013*, vol. 2, no. 2, pp. 1389–1400, 2013.

[91] J. M. Dick, "CHNOSZ: Thermodynamic calculations and diagrams for geochemistry," *Front. Earth Sci.*, vol. 7, no. July, pp. 1–18, 2019, doi: 10.3389/feart.2019.00180.

[92] Thermocalc Software, "TCS Al-based Alloy Database (TCAL7)," 2020, [Online].

Available: https://thermocalc.com/content/uploads/Documentation/Databases/Thermodynamic/tcal7-technical-info.pdf.

[93] A. S. Foundation, “Overview of Thermodynamic Databases - 2020a A Strong Foundation.”

[94] C. T. Stockholm, “Release Notes : Thermo-Calc Software Package Version 2015a,” *Thermo*, 2015.

[95] ASTM-E473, “Standard Terminology Relating to Thermal Analysis and Rheology,” *ASTM Int.*, 2014, doi: 10.1520/E0473-14.controlled-temperature.

[96] C. Dsc, M. Dsc, and L. C. Thomas, “An Introduction to the Techniques of Differential Scanning Δ Q = dt dt.”

[97] M. E. Brown and M. E. Brown, “Differential thermal analysis (DTA) and differential scanning calorimetry (DSC),” *Introd. to Therm. Anal.*, pp. 23–49, 1988, doi: 10.1007/978-94-009-1219-9_4.

[98] C. Potter, T. Application, S. Sarah, R. Application, S. Fred, and T. Manager, “Materials Characterization by Thermal Analysis (DSC & TGA), Rheology, and Dynamic Mechanical Analysis (Part 2).”

[99] W. J. Boettinger, U. R. Kattner, K. Moon, and J. H. Perepezko, *DTA and Heat-Flux DSC Measurements of Alloy Melting and Freezing*. Elsevier Ltd, 2007.

[100] D. Scanning, “Differential Scanning Calorimetry (DSC) A Beginner ’ s Guide.”

[101] C. Michaelsen, K. Barmak, and T. P. Weihs, “Investigating the thermodynamics and kinetics of thin-film reactions by differential scanning calorimetry,” *J. Phys. D. Appl. Phys.*, vol. 30, no. 23, pp. 3167–3186, 1997, doi: 10.1088/0022-3727/30/23/001.

[102] N. Gao, M. J. Starink, and T. G. Langdon, “Using differential scanning calorimetry as an analytical tool for ultrafine-grained metals processed by severe plastic deformation,” *Mater. Sci. Technol.*, vol. 25, no. 6, pp. 687–698, 2009, doi: 10.1179/174328409X408901.

[103] M. J. Starink, “Analysis of aluminium based alloys by calorimetry: Quantitative analysis of reactions and reaction kinetics,” *Int. Mater. Rev.*, vol. 49, no. 3–4, pp. 191–226, 2004, doi: 10.1179/095066004225010532.

[104] E. Laboratories, “Using Differential Scanning Calorimetry to Characterize Polymers The Importance of Characterizing Thermal Behaviour of Polymers,” pp. 1–15, 2018.

[105] N. ÅNMARK, “A calorimetric analysis and solid-solubility examination of aluminium alloys containing low-melting-point elements, Master of Science Thesis. Stockholm, 2., 4., 9.-11. str.,” p. 121, 2012, [Online]. Available: http://urn.kb.se/resolve?urn=urn:nbn:se:kth:diva-103199%0Ahttps://drive.google.com/open?id=1-fuaIP5n7TyZOw0mwoY5kCJ-1vwMbbgT.

[106] L. Zhao, Y. Pan, H. Liao, and Q. Wang, “Degassing of aluminium alloys during re-melting,” *Mater. Lett.*, vol. 66, no. 1, pp. 328–331, 2012, doi: 10.1016/j.matlet.2011.09.012.

[107] M. Rettenmayr, “Melting and remelting phenomena,” *Int. Mater. Rev.*, vol. 54, no. 1, pp. 1–17, 2009, doi: 10.1179/174328009X392930.

[108] D. F. D. Heumannskaemper, “Matching Your Crucible to Your Application,” *Morgan Adv. Mater.*, 2020.

[109] R. R. Moskalyk and A. M. Alfantazi, “Processing of vanadium : a review,” vol. 16, pp. 793–805, 2003, doi: 10.1016/S0892-6875(03)00213-9.

[110] P. Mcquay, V. K. Sikka, Y. Khalfalla, and K. Benyounis, “Casting of Intermetallics,” in *Reference Module in Materials Science and Materials Engineering*, 2016.

[111] B. P. Bewlay, S. Nag, A. Suzuki, and M. J. Weimer, “TiAl alloys in commercial aircraft engines,” *Mater. High Temp.*, 2016, doi: 10.1080/09603409.2016.1183068.

[112] P. Jozwik, W. Polkowski, and Z. Bojar, “Applications of Ni3Al Based Intermetallic Alloys—Current Stage and Potential Perceptivities,” pp. 2537–2568, 2015, doi:

10.3390/ma8052537.

[113] A. Nouri and A. Sola, *Electron beam melting in biomedical manufacturing*, no. August. 2020.

[114] R. K. Ek, *Electron beam melting : Impact of part surface properties on metal fatigue and bone ingrowth*. 2019.

[115] J. Karlsson, *Optimization of Electron Beam Melting for Production of Small Components in Biocompatible Titanium Grades*, vol. 80. 2015.

[116] T. C. Dzogbewu, "Additive Manufacturing of Ti-based Intermetallic Alloys : A Review and Conceptualization of a Next-Generation Machine," 2021.

[117] Arcam EBM, "Arcam brochure," pp. 1–20, 2017, [Online]. Available: http://www.arcam.com/technology/electron-beam-melting/hardware/.

[118] L. E. Rännar, A. Koptyug, J. Olsén, K. Saeidi, and Z. Shen, "Hierarchical structures of stainless steel 316L manufactured by Electron Beam Melting," *Addit. Manuf.*, vol. 17, pp. 106–112, 2017, doi: 10.1016/j.addma.2017.07.003.

[119] M. Cagirici, P. Wang, F. L. Ng, M. L. S. Nai, J. Ding, and J. Wei, "Additive manufacturing of high-entropy alloys by thermophysical calculations and in situ alloying," *J. Mater. Sci. Technol.*, vol. 94, pp. 53–66, 2021, doi: 10.1016/j.jmst.2021.03.038.

[120] L. E. Murr and S. M. Gaytan, "Electron Beam Melting," *Compr. Mater. Process.*, vol. 10, no. March, pp. 135–161, 2014, doi: 10.1016/B978-0-08-096532-1.01004-9.

[121] C. M. Allen, K. A. Q. O'Reilly, B. Cantor, and P. V. Evans, "Intermetallic phase selection in 1XXX A1 alloys," *Progress in Materials Science*. 1998, doi: 10.1016/S0079-6425(98)00003-6.

[122] S. Camero, E. S. Puchi, and G. Gonzalez, "Effect of 0.1% vanadium addition on precipitation behavior and mechanical properties of Al-6063 commercial alloy," *J. Mater. Sci.*, 2006, doi: 10.1007/s10853-006-0794-0.

[123] Y. Meng, J. Cui, Z. Zhao, and Y. Zuo, “Effect of vanadium on the microstructures and mechanical properties of an Al-Mg-Si-Cu-Cr-Ti alloy of 6XXX series,” *J. Alloys Compd.*, vol. 573, pp. 102–111, 2013, doi: 10.1016/j.jallcom.2013.03.239.

[124] Y. Xu, H. Jiao, M. Wang, and S. Jiao, “Direct preparation of V-Al alloy by molten salt electrolysis of soluble NaVO3 on a liquid Al cathode,” *J. Alloys Compd.*, vol. 779, pp. 22–29, 2019, doi: 10.1016/j.jallcom.2018.11.232.

[125] H. Li Wan, B. Qiang Xu, L. Jie Li, B. Yang, L. Wang, and Y. nian Dai, “Electrode heating effects on the preparation of Al-65V alloy,” *J. Cent. South Univ.*, vol. 27, no. 1, pp. 0–1, 2020, doi: 10.1007/s11771-020-4272-7.

[126] R. Alloys, “United States Patent (19),” vol. 475, no. 19, 1982.

[127] J. Sengupta, B. G. Thomas, and M. A. Wells, “The use of water cooling during the continuous casting of steel and aluminium alloys,” *Metall. Mater. Trans. A Phys. Metall. Mater. Sci.*, vol. 36 A, no. 1, pp. 187–204, 2005, doi: 10.1007/s11661-005-0151-y.

[128] M. Containing *et al.*, “Standard Specification for Powder Metallurgy (PM) Titanium and Titanium Alloy,” pp. 1–4, 2020, doi: 10.1520/B988-18.

[129] M. Hellenbrandt, “The inorganic crystal structure database (ICSD) - Present and future,” 2004, doi: 10.1080/08893110410001664882.

[130] M. C. Morris *et al.*, “STANDARD X-RAY DIFFRACTION POWDER PATTERNS.,” *NBS Monogr. (United States)*, 1982.

[131] ASTM, “ASTM E384: Standard Test Method for Microindentation Hardness of Materials,” *Annu. B. ASTM Stand.*, pp. 1–42, 2016, doi: 10.1520/E0384-10.2.

[132] R. Wriedds, HA and Gokcen, NA and Nafziger, “Binary Alloy phase diagrams, ed. by TB Massalki,” *Okomoto, PR subramanian L Kacprzak, ASM, Met. Park. ohio*, vol. 1729, 1990.

[133] W. Rostoker and A. Yamamoto, “A Survey of vanadium binary systems,” *Trans. Am. Soc. Met.*, vol. 46, p. 1136, 1954.

[134] J. S. D.Bailey, O.Carlson, “The aluminium-rich end of the aluminium-vanadium system.,” *Trans. Am. Soc. Met.*, vol. 51, pp. 1097–1102, 1959.

[135] R. Elliott, “Written discussion in the aluminium-vanadium alloys system.,” *Trans. Am. Soc. Met.*, vol. 47, pp. 538–542, 1955.

[136] I. Ansara, A. T. Dinsdale, and M. H. Rand, *Thermochemical database for light metal alloys*. 1998.

[137] C. Overview, “Master Alloys – Vanadium,” no. 43, pp. 23–26.

[138] S. T. Methods, “Standard Test Methods for Determination of Carbon, Sulfur, Nitrogen, and Oxygen in Steel, Iron, Nickel, and Cobalt Alloys by Various Combustion and Inert Gas Fusion Techniques 1,” vol. i, pp. 1–22, 2019, doi: 10.1520/E1019-18.2.

[139] ASTM committee and others, “ASTM standards E 1409-05 standard test method for determination of oxygen and nitrogen in titanium and titanium alloys by the inert gas fusion technique,” *ASTM 2005*, 2005.

[140] “Ti-6Al-4V (Grade 5),” no. Grade 5, p. 5273331, 1930.

[141] C. R. Hubbard and G. J. McCarthy, “JCPDS-International Centre for Diffraction Data,” *Acta Crystallogr. Sect. A Found. Crystallogr.*, vol. 37, no. a1, pp. C344–C344, Aug. 1981, doi: 10.1107/S0108767381089368.

[142] A. Kostov and D. Zivkovic, “Thermodynamic analysis of alloys Ti-Al, Ti – V, Al – V and Ti-Al – V ˇ,” vol. 460, pp. 164–171, 2008, doi: 10.1016/j.jallcom.2007.05.059.

[143] A. Kostov and B. Friedrich, “THERMODYNAMIC STUDY OF Ti-V AND Al-V SYSTEMS USING FACTSAGE,” pp. 57–65, 2006.

[144] D. Zivkovic and B. Friedrich, “Thermodynamic study of Ti-V and Al-V systems using FactSage THERMODYNAMIC STUDY OF Ti-V AND Al-V SYSTEMS USING FACTSAGE,” no. June 2014, 2006.

[145] Z. Chen *et al.*, "First-principles investigation of thermodynamic, elastic and electronic properties of Al3V and Al3Nb intermetallics under pressures," *J. Appl. Phys.*, vol. 117, no. 8, 2015, doi: 10.1063/1.4913664.

[146] E. Ghasali, A. H. Pakseresht, M. Alizadeh, K. Shirvanimoghaddam, and T. Ebadzadeh, "Vanadium carbide reinforced aluminium matrix composite prepared by conventional, microwave and spark plasma sintering," *J. Alloys Compd.*, vol. 688, pp. 527–533, 2016, doi: 10.1016/j.jallcom.2016.07.063.

[147] A. Das, S. Sunil, and R. Kapoor, "Effect of Cooling Rate on the Microstructure of a Pressure Vessel Steel," *Metallogr. Microstruct. Anal.*, vol. 8, no. 6, pp. 795–805, 2019, doi: 10.1007/s13632-019-00585-6.

[148] N. Haghdadi, A. B. Phillion, and D. M. Maijer, "Microstructure characterization and thermal analysis of aluminium alloy B206 during solidification," pp. 1–22.

[149] B. Benjunior, A. H. Ahmad, M. M. Rashidi, and M. S. Reza, "Effect of Different Cooling Rates Condition on Thermal Profile and Microstructure of Aluminium 6061," *Procedia Eng.*, vol. 184, pp. 298–305, 2017, doi: 10.1016/j.proeng.2017.04.098.

[150] Y. Meng, J. Cui, Z. Zhao, and Y. Zuo, "Study on microstructures of Al-4 wt pct V master alloys," *Metall. Mater. Trans. A Phys. Metall. Mater. Sci.*, 2014, doi: 10.1007/s11661-014-2314-1.

[151] S. A. Speakman and D. Ph, "Introduction to X-Ray Powder Diffraction Data Analysis An X-ray diffraction pattern is a plot of the intensity of X-rays scattered at different angles by a sample."

[152] C. Tiwary, V. V. Gunjal, D. Banerjee, and K. Chattopadhyay, "Intermetallic eutectic alloys in the Ni-Al-Zr system with attractive high-temperature properties," *MATEC Web Conf.*, vol. 14, no. January 2015, p. 01005, 2014, doi: 10.1051/matecconf/20141401005.

[153] J. Esquivel and R. K. Gupta, "Influence of the V content on microstructure and hardness of high-energy ball-milled nanocrystalline Al-V alloys," *J. Alloys Compd.*, vol. 760, pp. 63–

70, Sep. 2018, doi: 10.1016/J.JALLCOM.2018.05.132.

[154] P. Paupler, “G. E. Dieter. Mechanical Metallurgy. 3rd ed., Mc Graw-Hill Book Co., New York 1986. XXIII + 751 p., DM 138.50, ISBN 0–07–016893–8,” *Cryst. Res. Technol.*, 1988, doi: 10.1002/crat.2170230211.

[155] R. W. Armstrong, “Hall-Petch Relationship : Use in Characterizing Properties of Aluminum and Aluminum Alloys,” *Encycl. Alum. Its Alloy.*, 2016.

[156] T. J. Rupert, J. C. Trenkle, and C. A. Schuh, “Enhanced solid solution effects on the strength of nanocrystalline alloys,” *Acta Mater.*, 2011, doi: 10.1016/j.actamat.2010.11.026.

[157] K. Kim, D. Kim, K. Park, M. Cho, S. Cho, and H. Kwon, “Effect of intermetallic compounds on the thermal and mechanical properties of Al-Cu composite materials fabricated by spark plasma sintering,” *Materials (Basel).*, vol. 12, no. 9, pp. 1–13, 2019, doi: 10.3390/ma12091546.

[158] D. Zhang, H. V. Atkinson, H. Dong, and Q. Zhu, “Differential Scanning Calorimetry (DSC) and Thermodynamic Prediction of Liquid Fraction vs Temperature for Two High-Performance Alloys for Semi-Solid Processing (Al-Si-Cu-Mg (319s) and Al-Cu-Ag (201)),” *Metall. Mater. Trans. A Phys. Metall. Mater. Sci.*, vol. 48, no. 10, pp. 4701–4712, 2017, doi: 10.1007/s11661-017-4235-2.

[159] L. Tian, Y. Guo, J. Li, F. Xia, M. Liang, and Y. Bai, “Effects of solidification cooling rate on the microstructure and mechanical properties of a cast Al-Si-Cu-Mg-Ni piston alloy,” *Materials (Basel).*, vol. 11, no. 7, pp. 3–11, 2018, doi: 10.3390/ma11071230.

CHAPTER 8. APPENDIX A

8.1 SEM-EDX analysis (point count analysis)

The SEM-EDX point count analyses were performed on the selected regions of the aluminothermic produced master alloy. Spectra were selected as shown in the micrograph. The elemental composition was dominated by the Al and V elements. Similar observations were made on identical micrographs of the same 60Al-40V alloy on similar samples of the aluminothermy produced master alloy. The general trend of the elemental composition obtained from the different spectra is, therefore, presented below.

Figure 8-1 represents the SEM-EDX electron image of the master alloy and the selected spectra (spectra 1 to 9 respectively) on which the elemental chemical determination was performed.

Region 1- SEM electron image

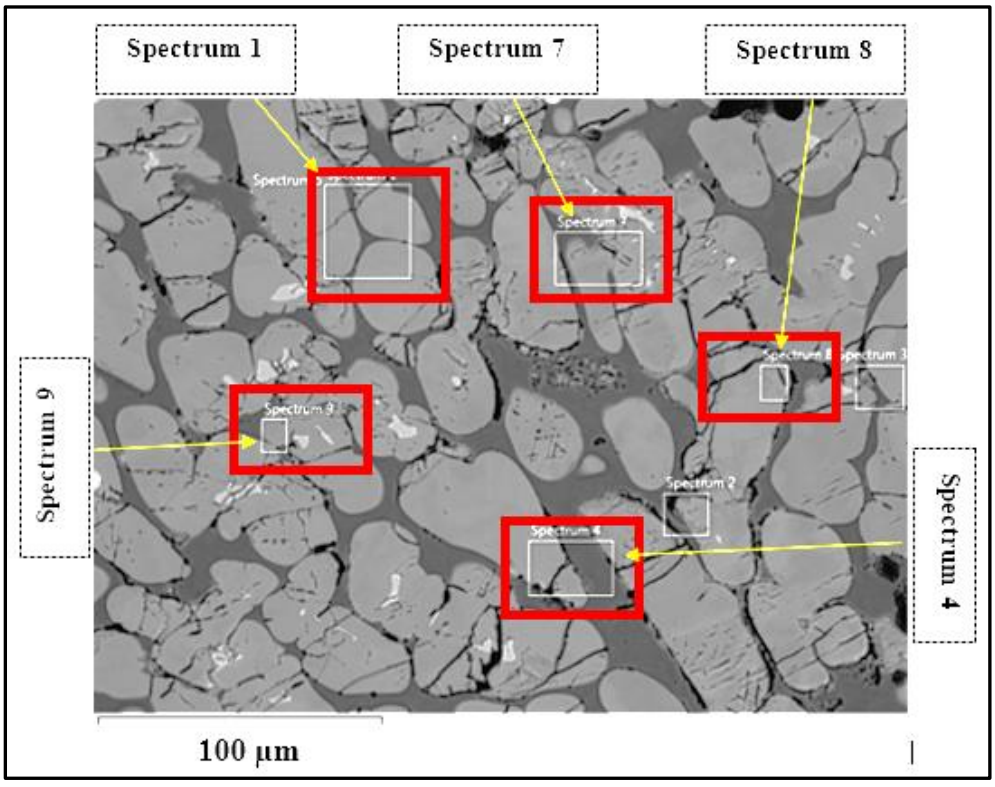

Figure 8-1: SEM-EDX electron image (region 1)

The corresponding chemical composition graph and table of EDX results for the selected spectra are illustrated below.

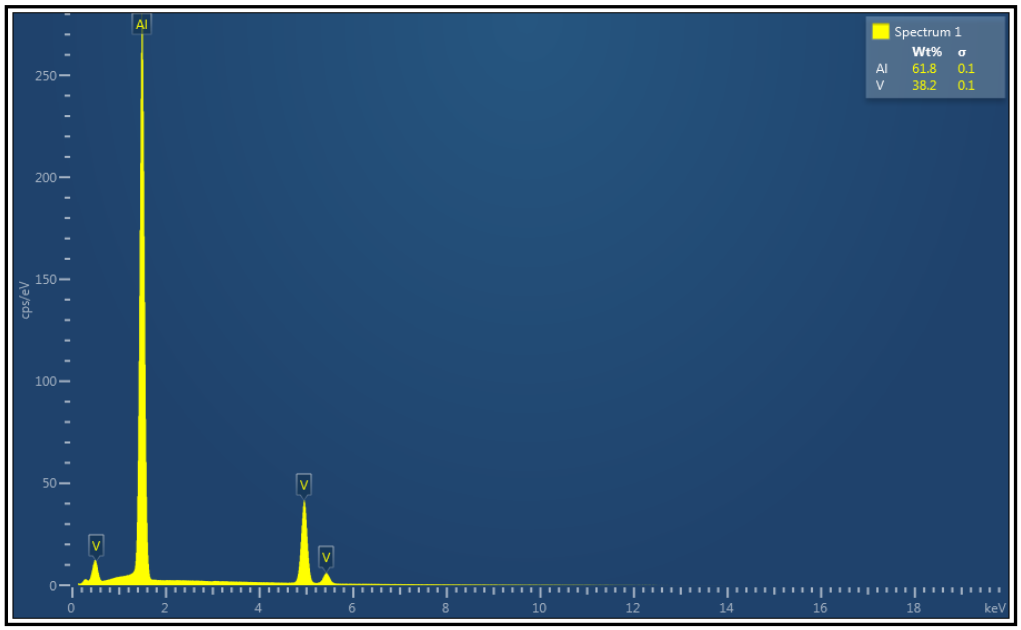

Figure 8-2: Spectrum 1- chemical composition analysis.

Table 8-1. EDX analysis results for zone 1- spectrum 1

Element	**Line Type**	**Apparent Concentration**	**k Ratio**	**Wt.%**	**% Error**	**Standard Label**	**Factory Standard**
Al	K series	19.08	0.13701	61.77	0.07	Al_2O_3	Yes
V	K series	9.21	0.09208	38.23	0.07	V	Yes
Total:				100.00			

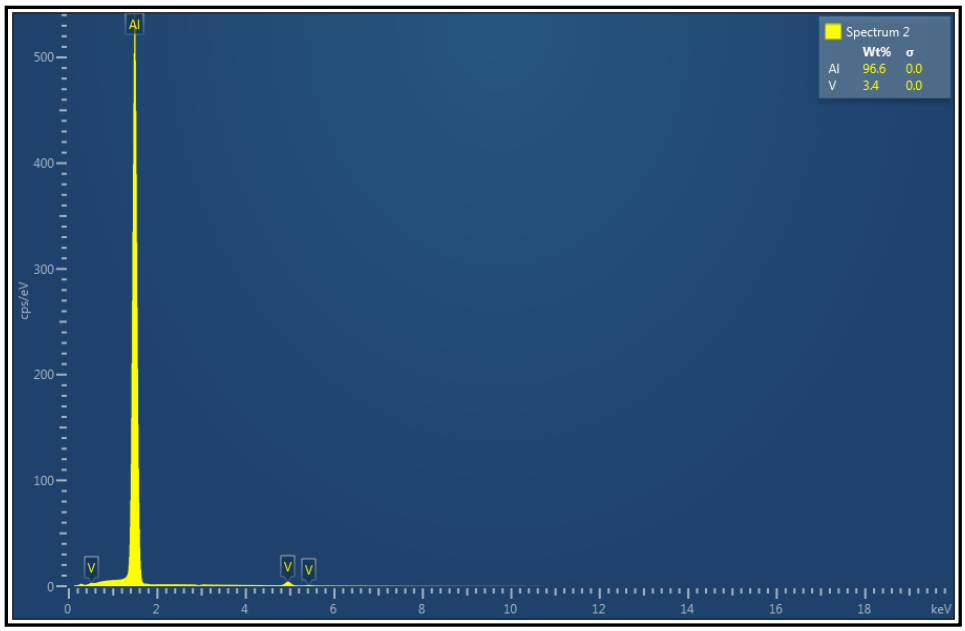

Figure 8-3: Spectrum 2 - chemical composition analysis

Table 8-2. EDX analysis results for zone 1- spectrum 2

Element	**Line Type**	**Apparent Concentration**	**k Ratio**	**Wt.%**	**% Error**	**Standard Label**	**Factory Standard**
Al	K series	37.01	0.26582	96.61	0.04	Al_2O_3	Yes
V	K series	0.80	0.00796	3.39	0.04	V	Yes
Total:				100.00			

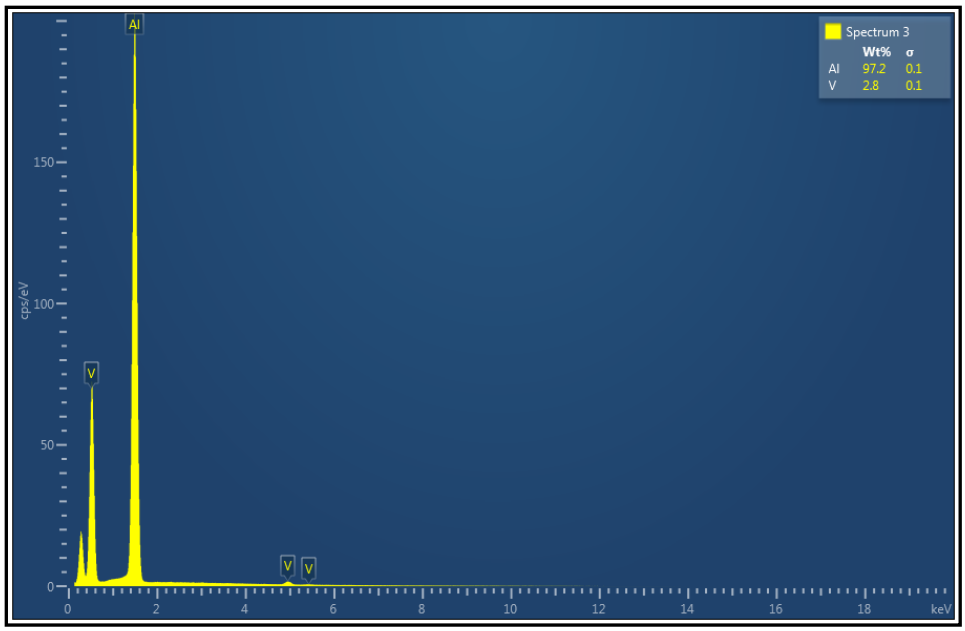

Figure 8-4: Spectrum 3 - chemical composition analysis

Table 8-3. EDX analysis results for zone 1- spectrum 3

Element	**Line Type**	**Apparent Concentration**	**k Ratio**	**Wt.%**	**% Error**	**Standard Label**	**Factory Standard**
Al	K series	13.79	0.09907	97.21	0.07	Al_2O_3	Yes
V	K series	0.24	0.00241	2.79	0.07	V	Yes
Total:				100.00			

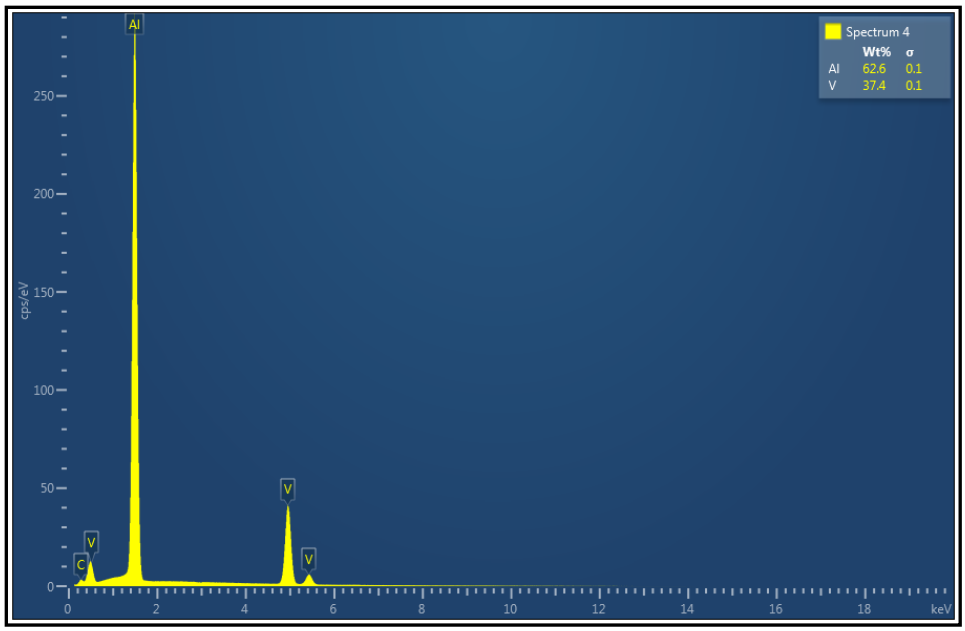

Figure 8-5: Spectrum 4 - chemical composition analysis

Table 8-4. EDX analysis results for zone 1- spectrum 4

Element	**Line Type**	**Apparent Concentration**	**k Ratio**	**Wt.%**	**% Error**	**Standard Label**	**Factory Standard**
Al	K series	19.80	0.14222	62.58	0.07	Al_2O_3	Yes
V	K series	9.18	0.09183	37.42	0.07	V	Yes
Total:				100.00			

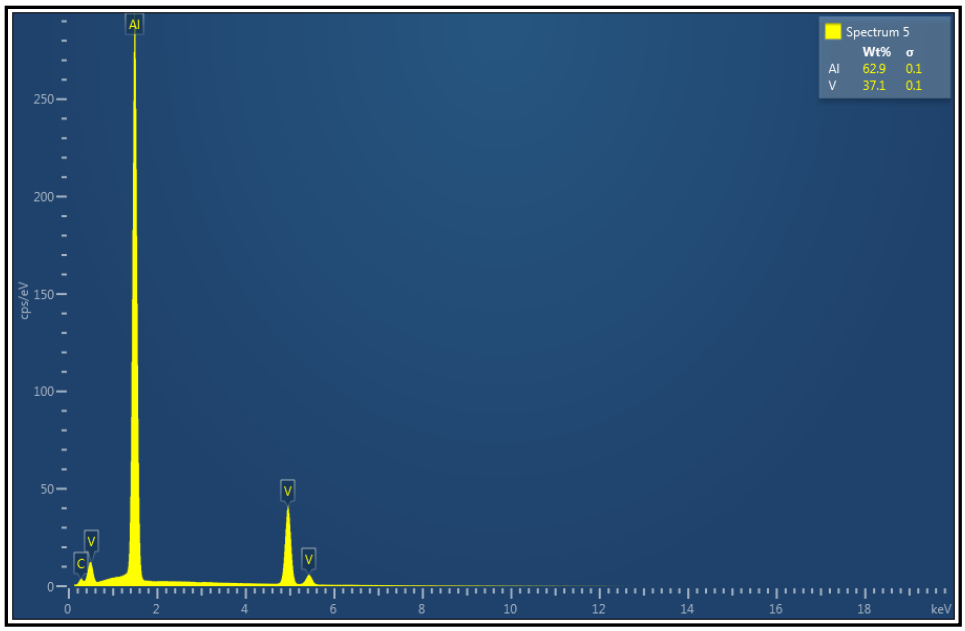

Figure 8-6: Spectrum 5 - chemical composition analysis

Table 8-5. EDX analysis results for zone 1- spectrum 5

Element	**Line Type**	**Apparent Concentration**	**k Ratio**	**Wt.%**	**% Error**	**Standard Label**	**Factory Standard**
Al	K series	20.00	0.14366	62.90	0.07	Al_2O_3	Yes
V	K series	9.13	0.09133	37.10	0.07	V	Yes
Total:				100.00			

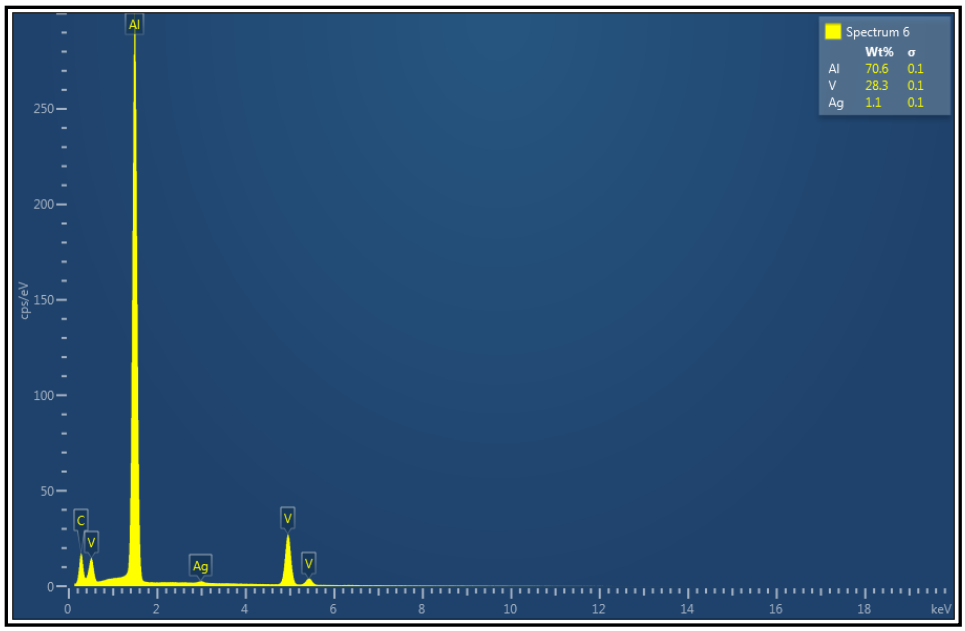

Figure 8-7: Spectrum 6 - chemical composition analysis

Table 8-6. EDX analysis for zone 1- spectrum 6

Element	Line Type	Apparent Concentration	k Ratio	% Error	Wt.% Sigma	Standard Label	Factory Standard
Al	K series	20.47	0.14700	71.33	0.07	Al_2O_3	Yes
V	K series	6.02	0.06021	28.67	0.07	V	Yes
Total:				100.00			

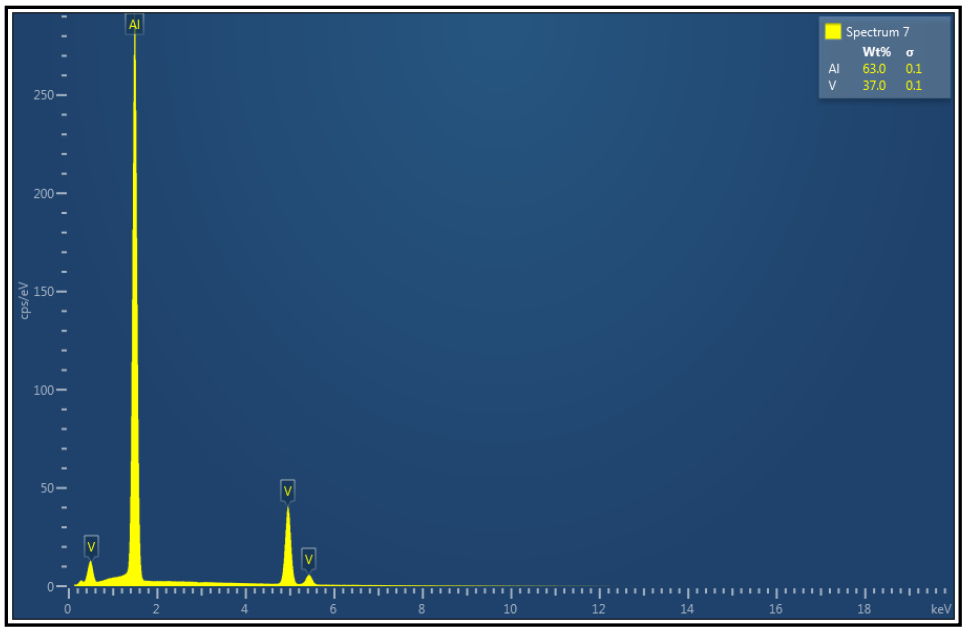

Figure 8-8: Spectrum 7- chemical composition analysis

Table 8-7. EDX analysis results for zone 1- spectrum 7

Element	**Line Type**	**Apparent Concentration**	**k Ratio**	**Wt.%**	**% Error**	**Standard Label**	**Factory Standard**
Al	K series	19.77	0.14199	62.98	0.07	Al_2O_3	Yes
V	K series	8.99	0.08990	37.02	0.07	V	Yes
Total:				100.00			

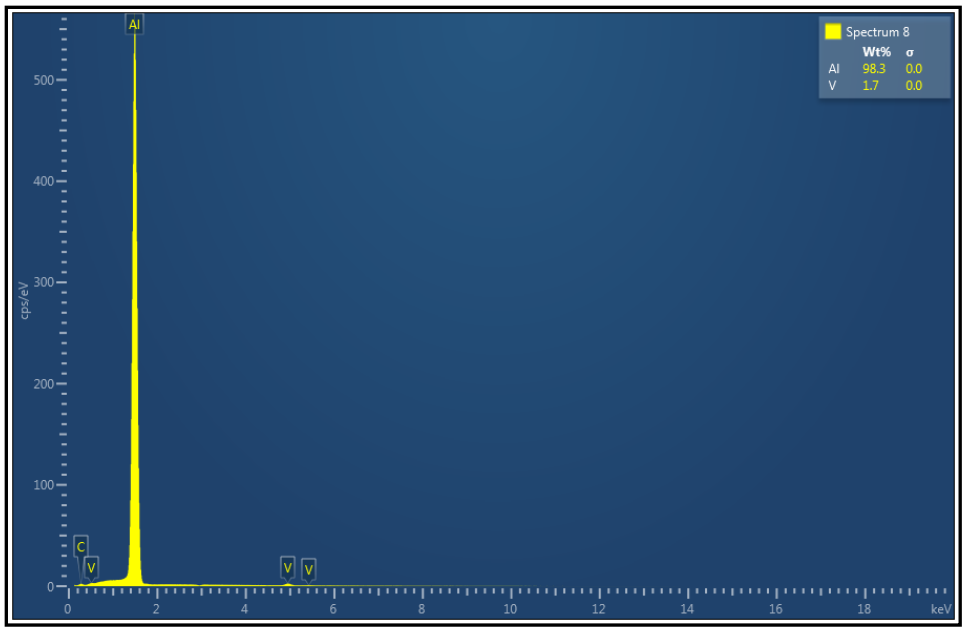

Figure 8-9: Spectrum 8 - chemical composition analysis

Table 8-8. EDX analysis results for zone 1- spectrum 8

Element	Line Type	Apparent Concentration	k Ratio	Wt.%	% Error	Standard Label	Factory Standard
Al	K series	38.68	0.27782	98.30	0.03	Al_2O_3	Yes
V	K series	0.41	0.00406	1.70	0.03	V	Yes
Total:				100.00			

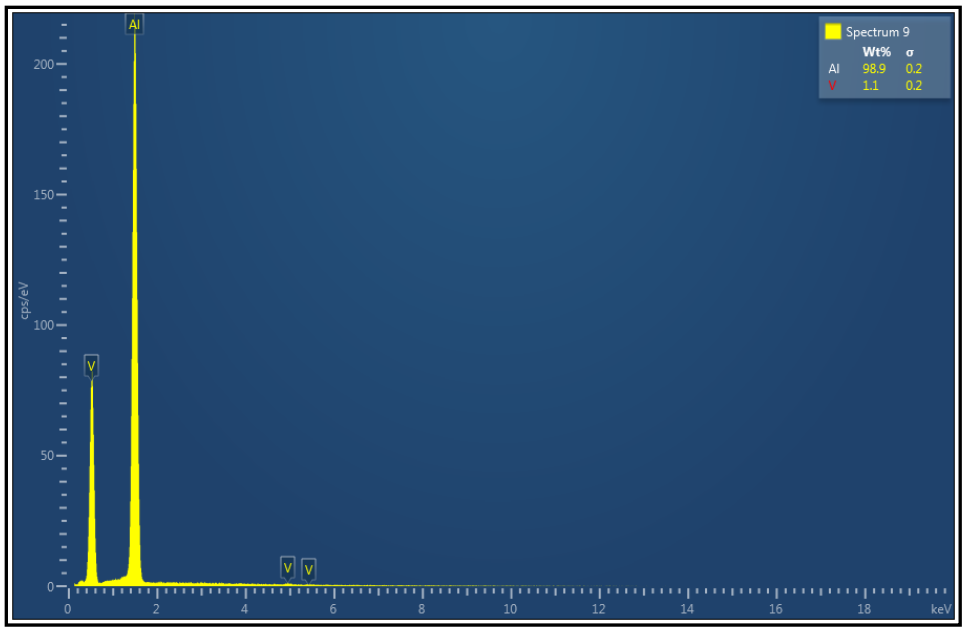

Figure 8-10: Spectrum 9- chemical composition analysis

Table 8-9. EDX analysis results for zone 1- spectrum 9

Element	**Line Type**	**Apparent Concentration**	**k Ratio**	**Wt.%**	**% Error**	**Standard Label**	**Factory Standard**
Al	K series	15.08	0.10833	98.90	0.22	Al_2O_3	Yes
V	K series	0.10	0.00101	1.10	0.22	V	Yes
Total:				100.00			

Figure 8-11 represent the SEM/EDX electron image of the two selected spectra (spectra 16 and 17 respectively) on which the elemental chemical determination was performed.

Region 2- SEM electron image

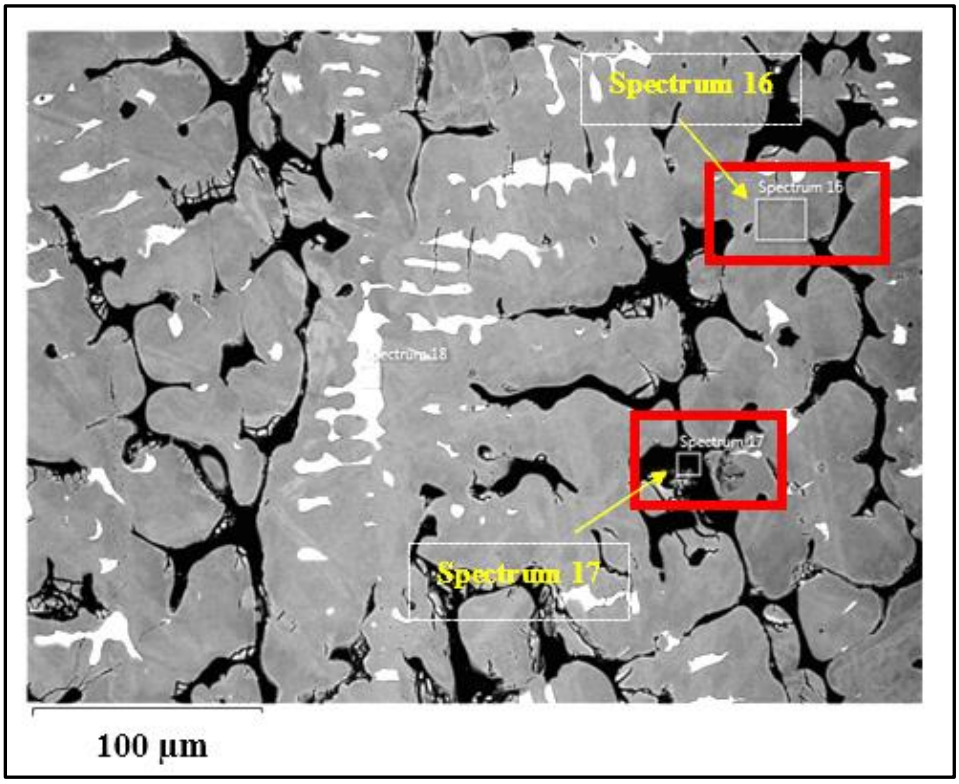

Figure 8-11: SEM-EDX electron image (zone 2)

The corresponding chemical composition graph and table of EDX results for the selected spectrum are illustrated below.

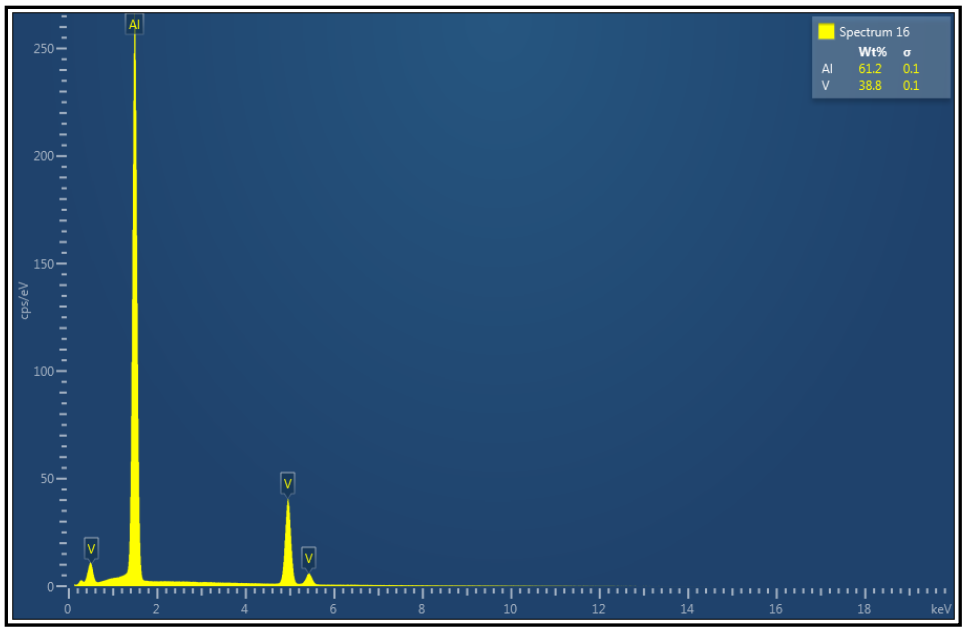

Figure 8-12: Spectrum 16- chemical composition analysis

Table 8-10. EDX analysis results for zone 2- spectrum 16

Element	Line Type	Apparent Concentration	k Ratio	Wt.%	% Error	Standard Label	Factory Standard
Al	K series	18.11	0.13004	61.20	0.07	Al_2O_3	Yes
V	K series	8.98	0.08985	38.80	0.07	V	Yes
Total:				100.00			

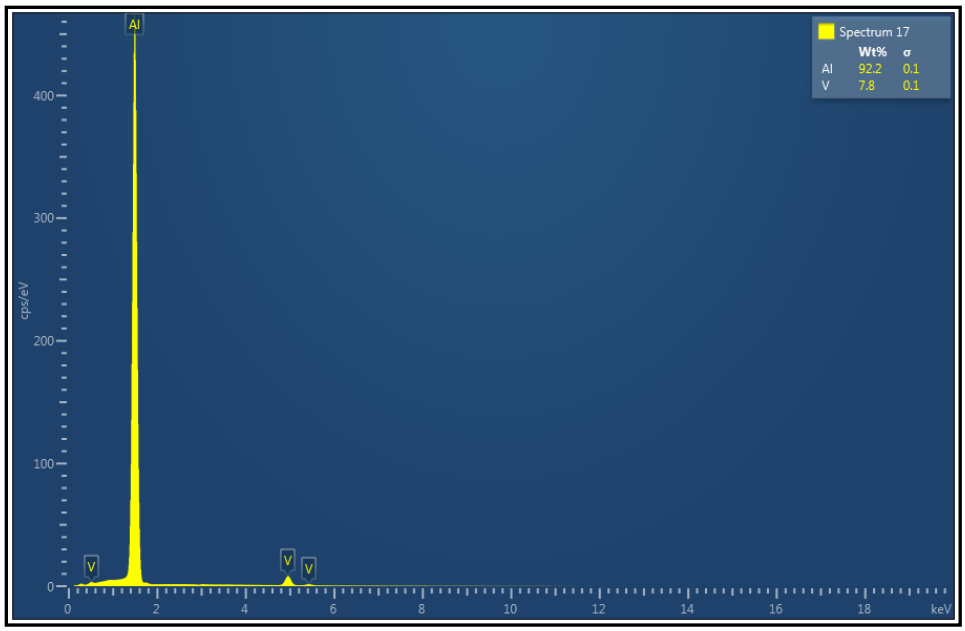

Figure 8-13: Spectrum 17-chemical composition analysis

Table 8-11. EDX analysis results for zone 2- spectrum 17

Element	**Line Type**	**Apparent Concentration**	**k Ratio**	**Wt.%**	**% Error**	**Standard Label**	**Factory Standard**
Al	K series	18.11	0.13004	92.20	0.07	Al_2O_3	Yes
V	K series	8.98	0.08985	7.80	0.07	V	Yes
Total:				100.00			

Figure 8-14 represents the SEM-EDX electron image for the next selected area (zone 3) on the specimen for elemental analysis. The last two spectrums from the 13 selected (spectra 22 and 23 respectively) are illustrated.

Region 3-SEM electron image

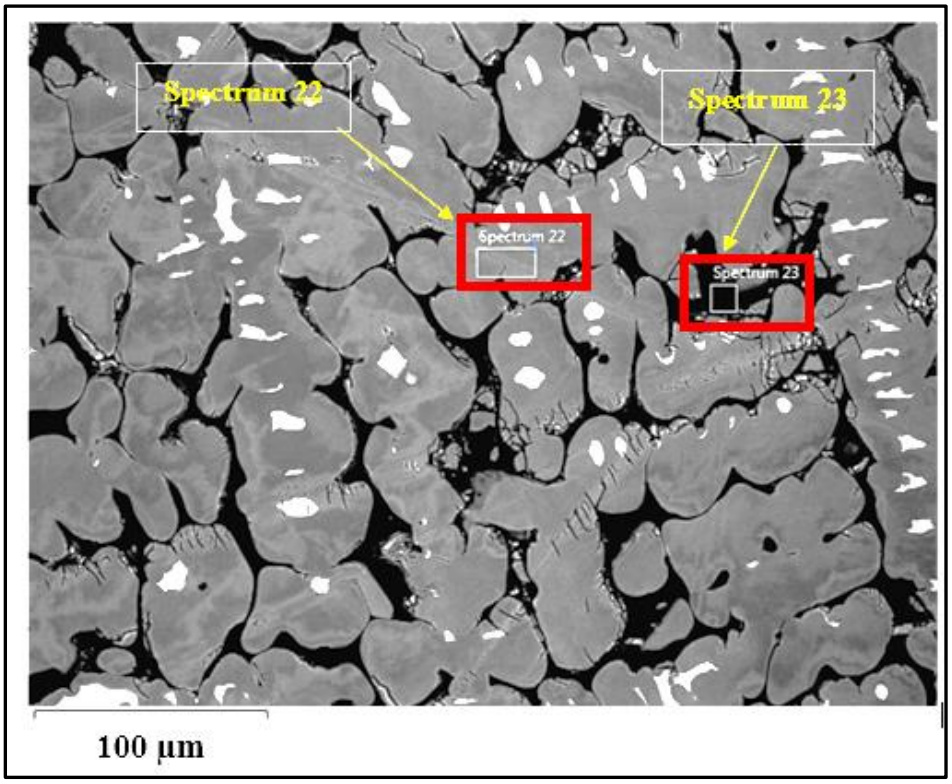

Figure 8-14: SEM-EDX electron image (zone 3)

The corresponding chemical composition graph and table of EDX results for the selected spectrum are illustrated below.

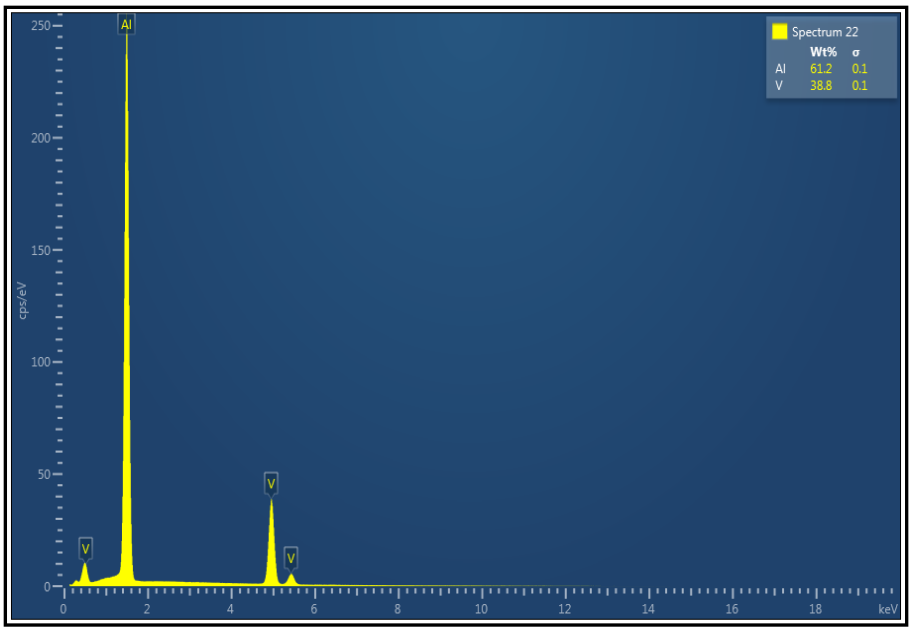

Figure 8-15. Spectrum 22- chemical composition analysis

Table 8-12. EDX analysis results for zone 3- spectrum 22

Element	Line Type	Apparent Concentration	k Ratio	Wt.%	% Error	Standard Label	Factory Standard
Al	K series	17.34	0.12454	61.22	0.07	Al_2O_3	Yes
V	K series	8.59	0.08595	38.78	0.07	V	Yes
Total:				100.00			

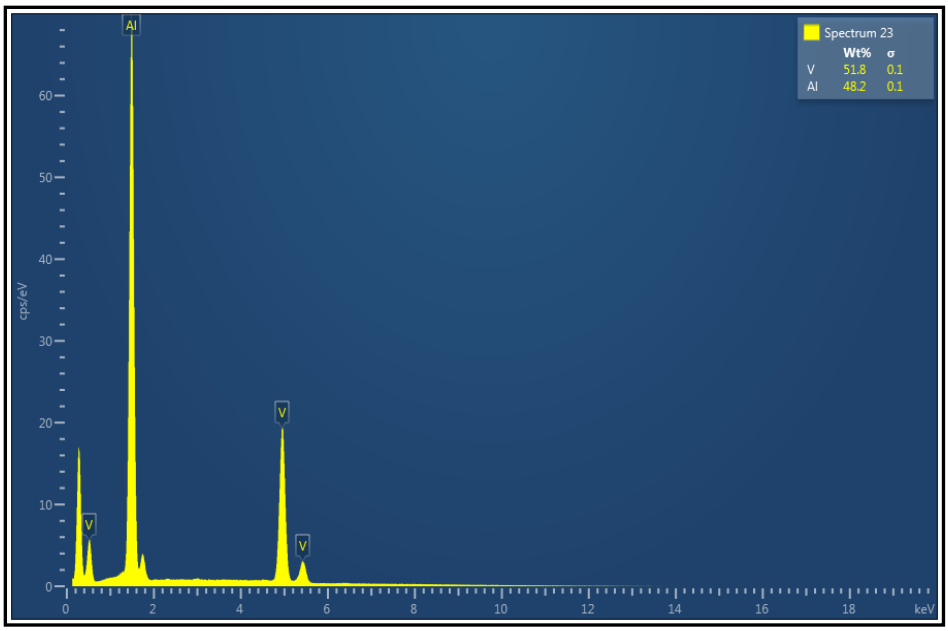

Figure 8-16. Spectrum 23-chemical composition analysis

Table 8-13. EDX analysis results for zone 3- spectrum 23

Element	Line Type	Apparent Concentration	k Ratio	Wt.%	% Error	Standard Label	Factory Standard
Al	K series	4.73	0.03400	48.23	0.11	Al_2O_3	Yes
V	K series	4.32	0.04321	51.77	0.11	V	Yes
Total:				100.00			

8.2 SEM-EDX analysis

The EDX mapping analyses were performed on four different mapping scans on the selected regions and gave the spatial elemental distribution as shown below (Figure 8-17 to Figure 8-19). The selected regions on the sample were scanned to inform on the spatial distribution of the Al and V elements contained in the material.

Scan mapping 2

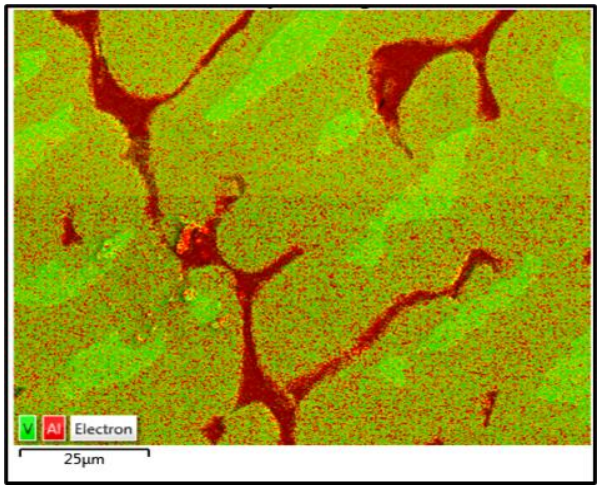

(a).

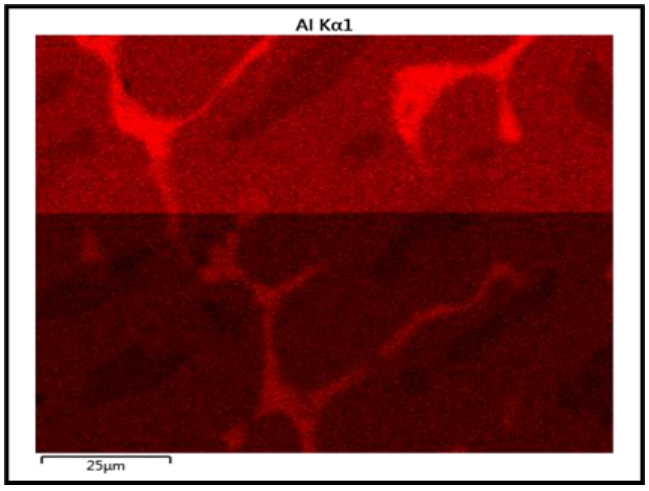

(b).

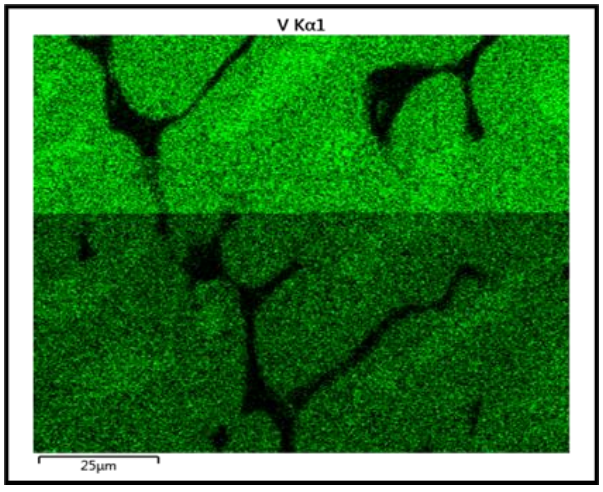

(c).

Voltage:15kV

Time of each analysis: 10 min (maps)

Element	wt.%	% Error	Atomic %
Al	62.13	0.07	75.60
V	37.87	0.07	24.40
Total:	100.00		100.00

(d).

Figure 8-17: SEM-EDX electron image, (a) elemental distribution map, (b) Al K series, (c) V K series of the master alloy, and (d) the average elemental composition of the scanned area (scan 2)

Scan mapping 3

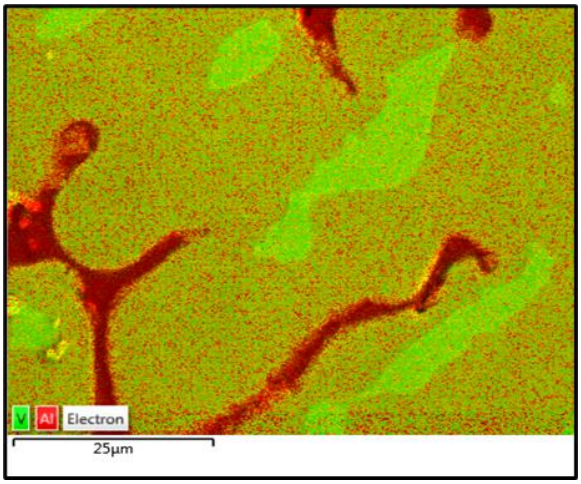

(a).

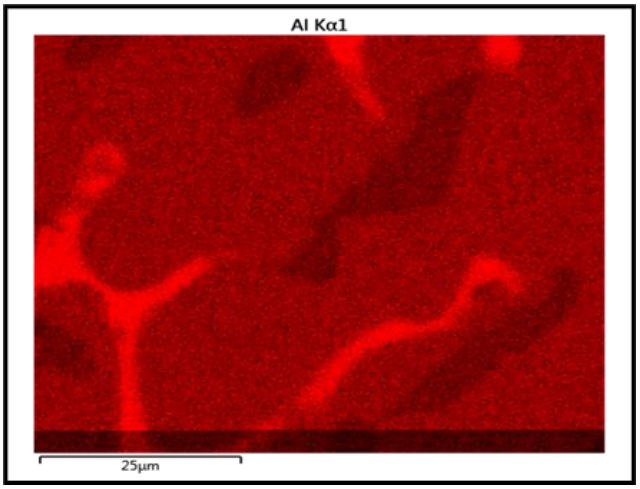

(b).

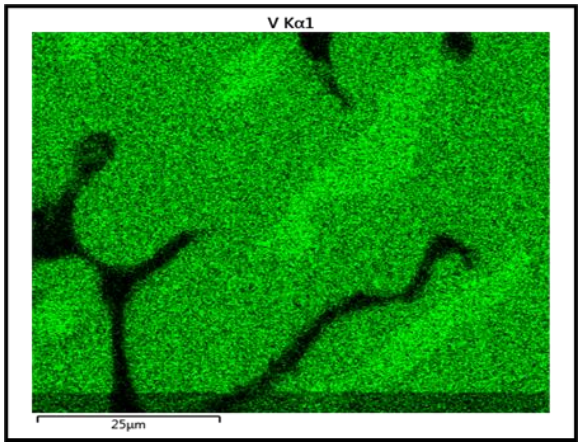

(c).

Voltage:15 kV

Time of each analysis: 10 min (maps)

Element	wt.%	% Error	Atomic %
Al	61.44	0.06	75.05
V	38.56	0.06	24.95
Total:	100.00		100.00

(d).

Figure 8-18: SEM-EDX electron image, (a) elemental distribution map, (b) Al K series, (c) V K series of the master alloy and (d) the average elemental composition of the scanned area (scan 3)

Scan mapping 4

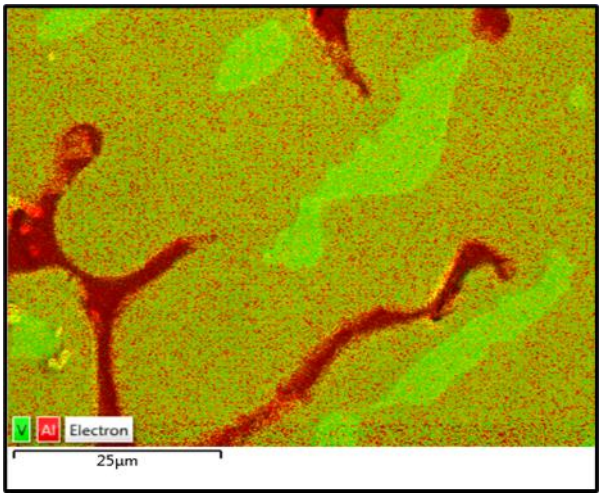

(a).

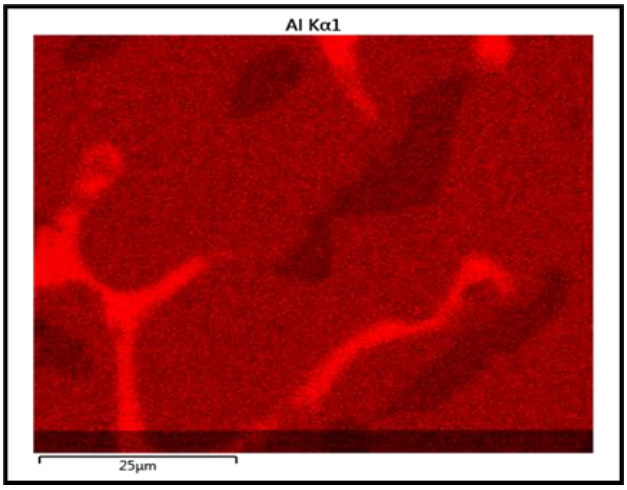

(b).

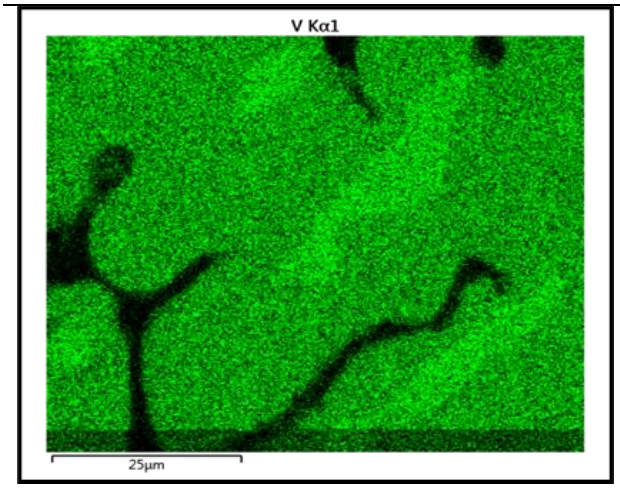

(c).

Voltage:15kV

Time of each analysis: 10 min (maps)

Element	wt.%	% Error	Atomic %
Al	63.05	0.03	76.31
V	36.95	0.03	23.69
Total:	100.00		100.00

(d).

Figure 8-19: SEM-EDX electron image, (a) elemental distribution map, (b) Al K series, (c) V K series of the master alloy and (d) the average elemental composition of the scanned area (scan 4)

8.3 SEM-EDX analysis after DSC-TG tests

The EDX analyses (point count) were performed on the samples after the DSC-TG tests for the temperature range between 1100 and1400 °C. Figure 8-20 represents the SEM micrograph and EDX spectra of the grey phase (spectrum 21), light grey phase (spectrum 22), and dark grey phase (spectrum 23) after the DSC-TG test at a temperature of 1100 °C.

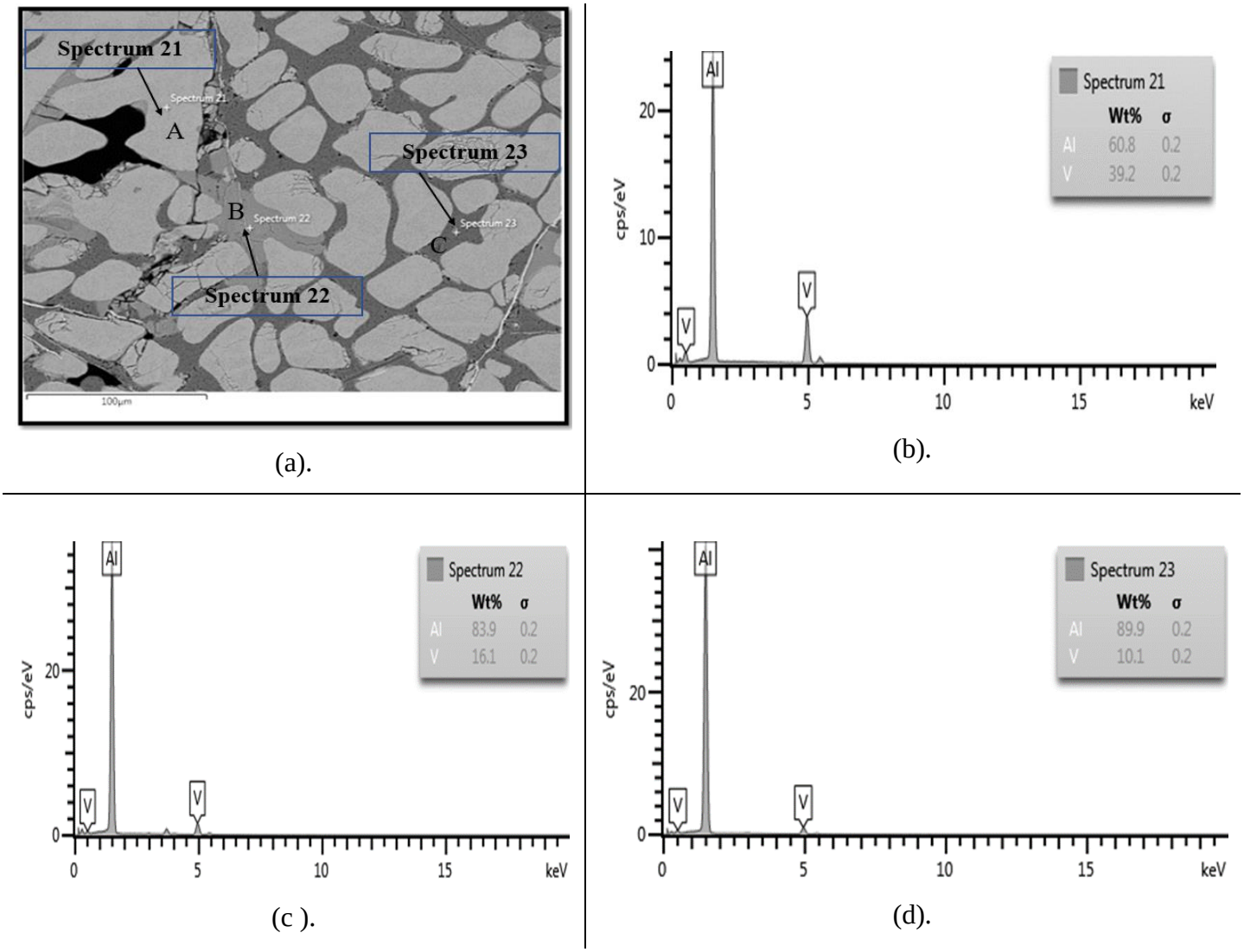

Figure 8-20: (a) SEM micrograph, and EDX spectra of (b) grey phase, (c) light grey phase, (d) dark grey phase after the DSC-TG test at the temperature of 1100 °C

Three spectra (spectrum 21-23) were selected on the micrograph in Figure 8-20 and their chemical compositions analyses are summarised in Table 8-14.

Table 8-14 gives the elemental composition of the three phases namely the grey, light grey, and (black) or dark grey phase obtained on the micrograph in Figure 8-20 after the DSC-TG test at a temperature of 1100 °C.

Table 8-14. EDX analysis after DSC-TG test at a temperature of 1100 °C

Spectrum	Phase description	Composition	
		Al [wt.%]	V[wt.%]
21	Grey phase	60.8 ± 0.2	39.2 ± 0.2
22	Light grey phase	83.9 ± 0.2	16.1 ± 0.2
23	Dark grey phase	89.9 ± 0.2	10.1 ± 0.2

Figure 8-21 represents the SEM micrograph and EDX spectra of the grey phase (spectrum 24), light grey phase (spectrum 25) and dark grey phase (spectrum 26) after the DSC-TG test at a temperature of 1400 °C. Their chemical compositions analyses are summarised in Table 8-15.

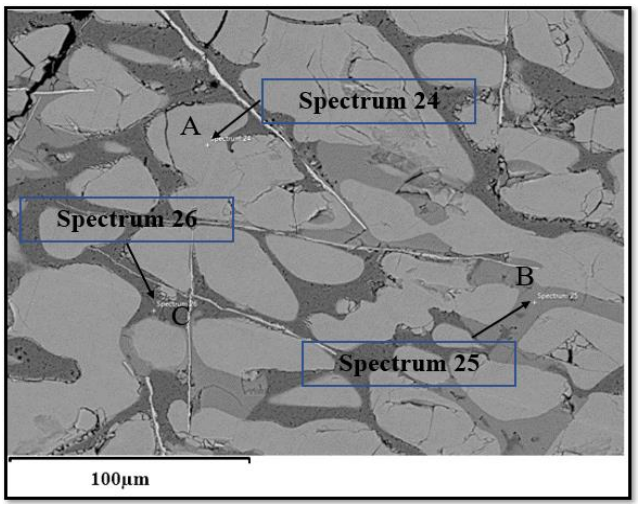

(a).

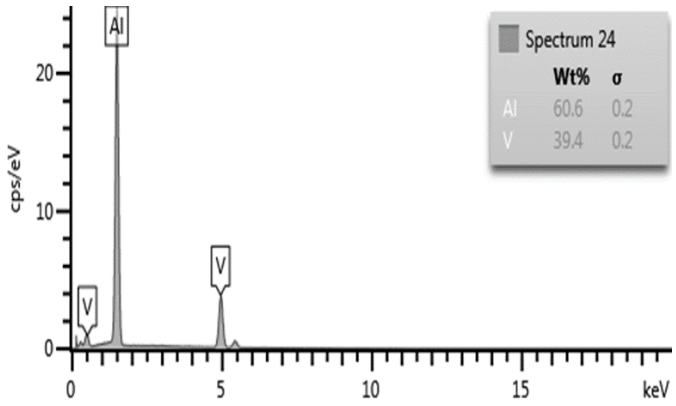

(b).

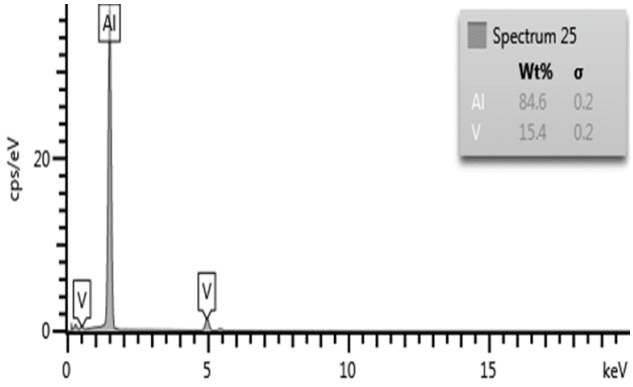

(c).

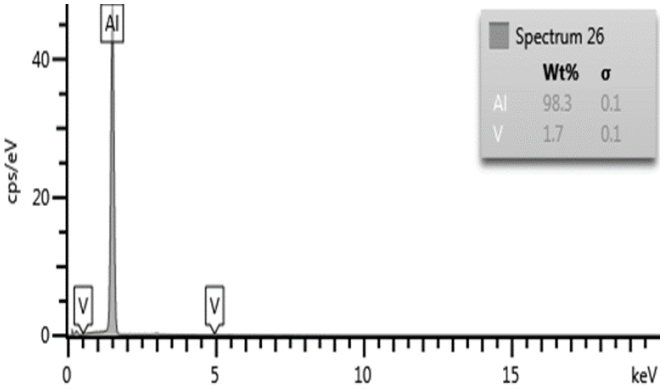

(d).

Figure 8-21: (a) SEM micrograph, and EDX spectra of (b) the grey phase, (c) light grey and (d) dark grey phase after the DSC-TG test at the temperature of 1400 °C

Table 8-15 gives the elemental compositions of the three phases namely the grey, light grey, and (black) or dark grey phase obtained on the micrograph of the master alloy after the DSC-TG test at a temperature of 1400 °C.

Table 8-15. EDX analysis after DSC-TG test at the temperature of 1400 °C

Spectrum	Phase description	Composition	
		Al [wt.%]	V[wt.%]
24	Grey phase	60.6 ± 0.2	39.4 ± 0.2
25	Light grey phase	84.6 ± 0.2	15.4 ± 0.2
26	Dark grey phase	98.3 ± 0.1	1.7 ± 0.1

Table 8-16 represents the summary of the elemental composition obtained from the different spectra depicted of the three phases namely the grey, light grey, and (black) or dark grey phase on the micrographs of the 60Al-40V master alloy after the DSC-TG test at temperature of 1100 and 1400 °C.

Table 8-16. Summary of the elemental composition obtained from different spectra after DSC-TG analyses at temperatures of 1100 and 1400 °C, respectively.

Spectrum	Phase description	Elements		Proposed phases
		Al [wt.%]	**V [wt.%]**	
21	Grey	60.8 ± 0.2	39.2 ± 0.2	$Al_3V + Al_8V_5$
22	Light grey	83.9 ± 0.2	16.1 ± 0.2	$Al_{21}V_2 + Al_{45}V_7$
23	Dark grey	89.9 ± 0.2	10.1 ± 0.2	$Al_{21}V_2 + Al_{45}V_7$
24	Grey	60.6 ± 0.2	39.4 ± 0.2	$Al_3V + Al_8V_5$
25	Light grey	84.6 ± 0.2	15.4 ± 0.2	$Al_{21}V_2 + Al_{45}V_7$
26	Dark grey	98.3 ± 0.1	1.7 ± 0.1	Al-fcc + $Al_{21}V_2$

8.4 DSC-TG thermal analysis

Temperature- heat flow graphs of the 60Al-40V master alloy for the respective 1st and 2nd heating-cooling cycle are given in Figure 8-22 and Figure 8-23 at the temperature of 1100 and 1400 °C, respectively.

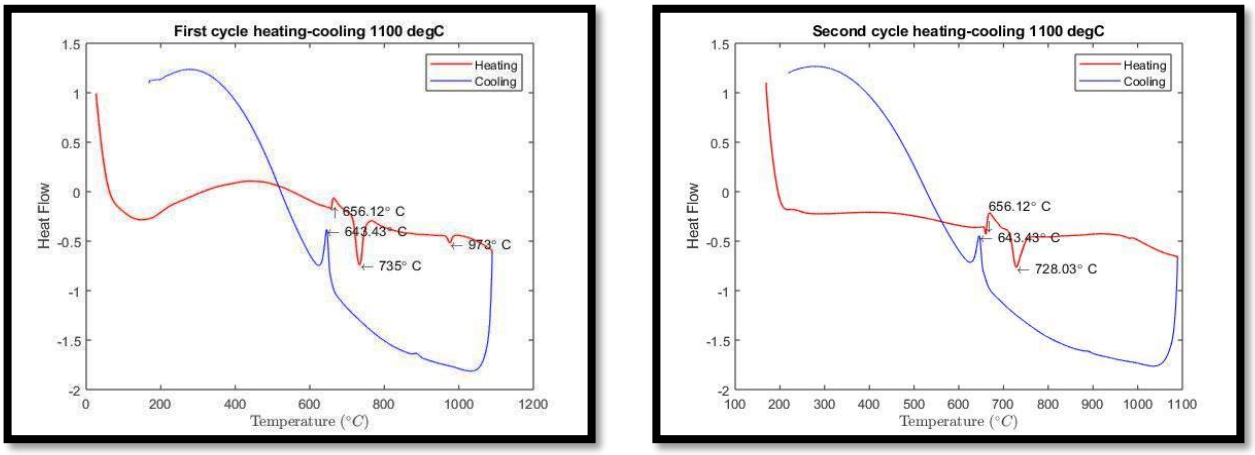

a. b.

Figure 8-22: The change in the heat flow of the 60Al-40V master alloy as a function of temperature at the temperature of 1100 °C

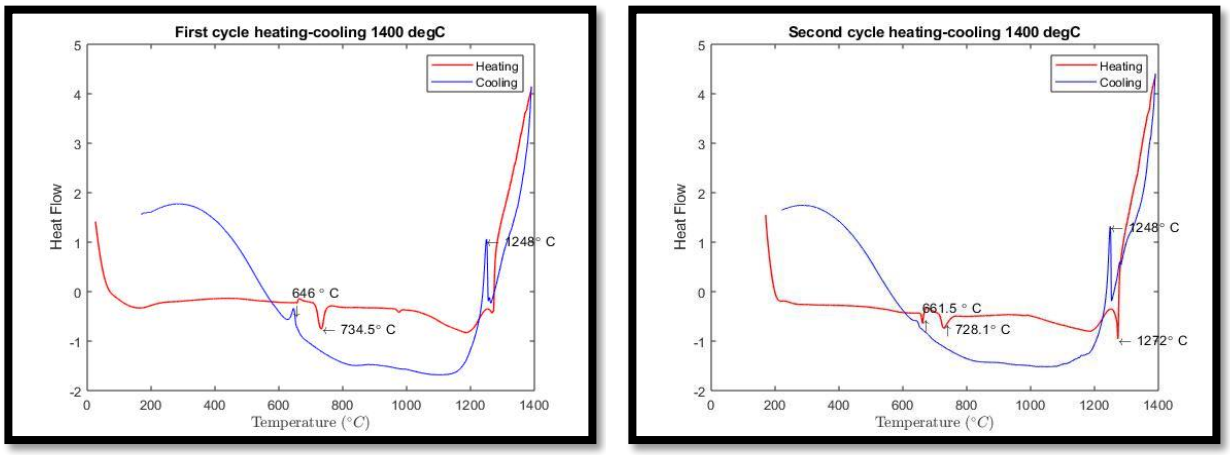

a. b.

Figure 8-23: The change in the heat flow of the 60Al-40V master alloy as a function of temperature at the temperature of 1400 °C.

It can be seen that transformations occur at different points as illustrated in both the first and second heating-cooling cycles. The melting, as well as cooling curves, show peaks of transformations temperatures which were approximatively occurring at the same values.